COLLOIDS AT LIQUID INTERFACES: DYNAMICS AND ORGANIZATION

Dmitry Ershov

Thesis committee

Promotors
Prof. dr. Jasper van der Gucht
Professor of Physical Chemistry and Colloid Science
Wageningen University

Co-promotor
Prof. dr. Martien A. Cohen Stuart
Professor of Physical Chemistry and Colloid Science
Wageningen University

Other members
dr. Peter Schall, Van der Waals-Zeeman Institute, University of Amsterdam.
Prof. dr. Jan Vermant, Department of Materials, ETH Zurich
Prof. dr. Marcel Janson, Laboratory of Cell Biology at Wageningen University
Prof. dr. Rene van Roij, Institute for Theoretical Physics, Utrecht University

This research was conducted under the auspices of Graduate School VLAG.

COLLOIDS AT LIQUID INTERFACES: DYNAMICS AND ORGANIZATION

Dmitry Ershov

Thesis
submitted in fulfillment of the requirements for the degree of doctor
at Wageningen University,
by the authority of the Rector Magnificus,
Prof. Dr. M. J. Kropff,
in the presence of the
Thesis Committee appointed by the Academic Board,
to be defended in public
On Monday 14 April 2014
at 4 p.m. in the Aula

Dmitry Ershov
Colloids at liquid interfaces: dynamics and organization
116 pages.

PhD thesis, Wageningen University, Wageningen, NL (2014)
With references and summary in English.

ISBN: 978-90-6173-894-3

Contents

CHAPTER 1

PARTICLES AT LIQUID INTERFACES

The topic of colloids at liquid interfaces deals with a wide range of problems. Fundamental research in this area focuses mainly on the effects of forces of different nature on organization, crystallization, and mobility of the particles. The forces can arise from the particles themselves (for example, electrostatic forces due to surface charges on the particles) or from the properties of the embedding interface (capillary interactions between particles due to the surface tension acting on the contact line), or they might be external (gravity, electromagnetic fields). It is the complex interplay between all these forces that determines how particles organize.

In this introductory chapter we describe the general behavior of particles trapped at liquid interfaces with a particular focus on capillary interactions.

1.1 Introduction

Colloids at liquid interfaces are used in a number of different technological areas. Pickering emulsions [1, 2], where the dispersed phase is stabilized by particles, are used in drug delivery, cosmetics and food industry [3-5]. Flotation processing, where particles are extracted from aqueous solution by gas bubbles creaming on the surface, is used in water treatment and mineral processing [6, 7]. Other examples are lithography from particles assembled at liquid-liquid interfaces [8], and antifoaming agents [9]. A fundamental understanding of how particles trapped at liquid interfaces behave and how their behavior can be controlled are important for further developments of these areas.

The behavior of colloids in bulk is often very different from that at an interface, because the presence of a border between two continuous phases introduces “side” effects. Even though a particle at an interface can still experience forces of the same nature as a particle in a bulk phase (for instance, electrostatic interactions for charged particles, or hydrodynamic interactions), their range and magnitude are strongly modified by the presence of the interface, because the properties of the space around the particle are not uniform anymore and change when crossing the interface from one phase to the other. Moreover, the interface itself can exert forces on objects that are in contact with it; these forces are called “capillary” forces [10].

Recent findings in the field of colloids at liquid interfaces showed that it is possible to tune capillary interactions between particles. One can induce anisotropic interactions between particles by controlling their shape [11-13], surface chemistry [14], or by tuning the geometry of the interface [15, 16].

Capillary interactions in combination with forces of different nature (i.e. electrostatic) can produce specific interaction potentials of either isotropic or anisotropic character. These findings suggest that there is a promise for guided self-assembly of colloids at liquid interfaces [17].

There are also open fundamental questions. The existence of isotropic attraction between like-charged particles deposited at oil-water interfaces was reported in [18], but reasons for this are still not fully explained [19, 20]. Yet another open question is how both phases that form the interface flow around a particle and affect the dynamics of particles at the interface, in particular when the interface has visco-elastic properties [21].

In this chapter we introduce the general properties of interfaces formed by two liquid phases (such as oil-water) or gas and liquid phases (air-water) and of particles adsorbed to such interfaces. We make a particular emphasis on the flotation capillary interactions [10] and the reasons why these interactions occur.

1.2 Surface tension

Liquid interfaces surround us everywhere in our daily life. There is an interface between water and air in a cup of tea, thousands of tiny interfaces between oil and water in mayonnaise. But if one pours some water into a glass and a second later pours some more, the water just mixes without forming any interface. So why do interfaces exist?

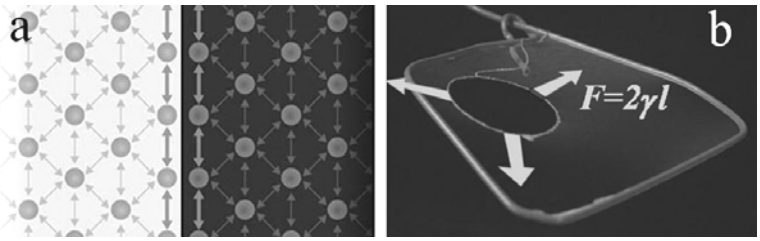

Figure 1.1. Surface tension concept: Interface formation between two immiscible liquids due to Van-der-Waals forces (**a**). Surface tension forces acting on a flexible loop, *l* is the length of the loop (**b**).

If we look deeper into the reason why interfaces exist, we find that any kind of interface appears because of Van der Waals forces. The molecules of one phase like to stay with their kind, and the molecules of the other phase are doing the same. Therefore the liquids don't mix and create a border between them - the interface. The transition from one phase to another is normally idealized to be sharp, as shown on Fig. 1.1a, but in reality there is a diffusive transition layer. Two phases tend to keep the area of the interface as small as possible to have minimal contact with each other's molecules: in Fig. 1.1b it is shown how a liquid film (which actually has two air-water interfaces) can expand a flexible loop in order to decrease its surface area. The magnitude of this effect is determined by the surface tension, γ, which is the force per unit length with which a surface acts on a contact line, as in Fig. 1.1b: $F = 2\gamma l$, where the factor 2 comes from the presence of two air-water interfaces in the film. Another, equivalent, definition of surface tension is the free energy cost of creating surface area, in J/m^2. Surface tension depends on the type of phases that create the interface, the temperature, the presence of third-party molecules (surfactants), and other parameters that might affect interactions between molecules of the two phases forming the interface.

There are very important consequences of surface tension. In order to minimize the surface energy, droplets of the dispersed phase tend to fuse together. If one tries to disperse oil in water without any agent to stabilize oil droplets, very soon he is going to witness that the dispersed oil droplets have coalesced. This happens, because the surface area of one big droplet is smaller than the surface area of many smaller droplets with the same overall volume. It also explains why the bubbles are spherical: in this form they have minimal surface area.

As we mentioned above, surface tension can be modified by adding surfactants to one of the phases, which later diffuse to the interface. Normally this leads to a decrease of the

surface free energy, so that by using surfactants one can create more stable emulsions or foams.

Another consequence of surface tension is that a surface can exert forces on objects and support them floating, even if their density is higher than that of water. A floating metal paperclip is a well-known example of this.

The surface tension forces (and interactions that they cause) were named “capillary”. This name comes from the surface tension driven rise of liquids inside a very thin tube – a capillary. Surface tension forces always lay in the plane tangential to the water interface, therefore the angle between the substrate upon which a surface pulls and the interface is of high importance.

1.3 Contact Angle

We know that some surfaces allow a water droplet to spread on them, and some prefer to have as little area in contact with water as possible. This is yet another manifestation of a surface phenomenon: the balance between surface tensions of air-water, substrate-water, and air-substrate defines how the water droplet will behave.

Air, water and the substrate create a specific line that is a border of all three phases present in this system, the “contact line”. The angle between the planes tangential to water and substrate surfaces at any point on the contact line is called the “contact angle”. In an ideal situation the contact angle is constant along the whole contact line, if the substrate is uniform, Fig. 1.2. The substrate is generally called hydrophilic if the contact angle of water is less than 90, and hydrophobic if otherwise.

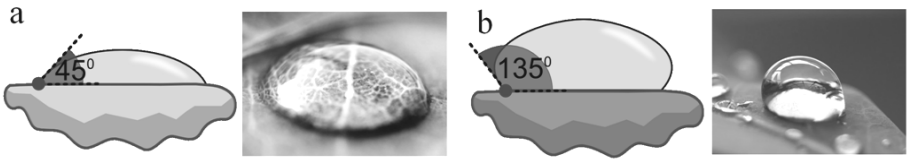

Figure 1.2. Contact angle (θ) and its effect on the shape of a water droplet. (**a**) A spreading droplet, $\theta = 45°$; (**b**) a spherical droplet, $\theta = 135°$.

To abovementioned balance is described by the Young relation: $\gamma_{SG} = \gamma_{SL} + \gamma_{LG} cos\theta$, where γ_{SG}, γ_{SL}, and γ_{LG} are substrate (or solid)-gas, substrate-liquid and liquid-gas surface tensions and θ is the equilibrium contact angle. A small water droplet on a substrate adopts shape that is directly affected by the contact angle (see Fig. 1.2).

There are several subtleties connected to determining the contact angle properly. The contact angle can be very different for a droplet that is expanded than for a droplet that shrinks (this is known as contact angle hysteresis). The substrate can have inhomogeneous properties, and the contact angle, therefore, will be different at different point along the

contact line; the latter effect, as will be discussed later, has a strong effect on the behavior of particles at a liquid interface.

1.4 Particles at liquid interfaces

We encounter particles at liquid interfaces everyday in our lives. These could be pepper particles on the surface of a cup of soup or dust particles on the surface of a puddle. Sometimes the particles spread across the surface as soon as they touch it, but sometimes they cling together instead of spreading. Particles exhibit peculiar behavior specifically due to the fact that they are situated at liquid interfaces, which they would never show such in the bulk.

Figure 1.3. Particles at liquid interfaces: floating flakes (**a**), floating paperclips (**b**), mosquito eggs on water interface (**c**).

A well-known example is the “cheerios effect”. This phenomenon is named after American breakfast cereals, flakes of which can be noticed to aggregate on the surface of milk and to get attracted to the bowl’s walls. A few readers have probably seen mosquito eggs on the surface of a puddle that stick to each other in a peculiar manner forming small “rafts” [22]. And some insects are known for utilizing the air-water interface in such a way that it will pull the insect towards the nearby shore [23, 24].

Small micron-sized particles at interfaces can also attract or repel each other, which leads to a variety of different organizations, some examples of which are shown in Fig. 1.4.

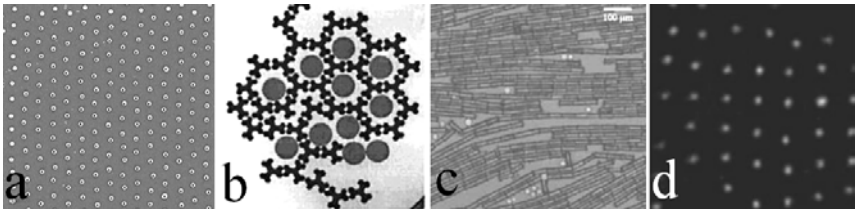

Figure 1.4. Particles organizing into different patterns at liquid interfaces. Examples of isotropic (**a**) and anisotropic interactions (**b-d**).

Being deposited at a liquid interface, particles decrease the surface area between the two phases, and therefore they reduce the surface energy. For example, a micrometer sized

colloidal particle deposited at an air-water interface reduces the surface energy by about 10^7 kT; so the adsorption energy is generally much higher than the thermal energy and the particles can be considered irreversibly adsorbed.

It is clear that the area reduction depends on the contact angle, as can be seen from Fig. 1.5. The contact angle has to be finite for particles to adsorb and the strongest adsorption occurs when the contact angle is $\theta = 90°$, when the displaced interfacial area is the largest.

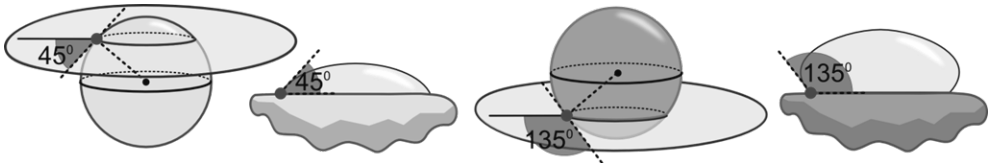

Figure 1.5. Contact angle and its effect on the vertical position of a particle. Contact angle is constant along the whole contact line.

There is also a direct effect of the contact angle on the particle's vertical position. Simply by changing the particle's vertical position, or more generally speaking, by moving it in a direction, normal to the interface, the contact angle is adjusted along the whole contact line because of the axial symmetry of the spherical particle.

However, in a vast variety of systems it is not possible to keep the contact angle constant everywhere along the contact line by repositioning a particle. In this case the particle has to deform the liquid interface in its vicinity to achieve an equilibrium position. This deformation field is called "meniscus". This is where the capillary forces come into the picture. Menisci change the area of the liquid interface, and if two such menisci overlap, this can effectively lead to a decrease or increase of the interfacial area and a corresponding change of the free energy of the system. This effectively leads to interactions between the floating particles, which are called capillary interactions.

In a number of articles the perturbation of the interface by particles is treated as a "capillary charge", which makes a beautiful analogy between electrostatic interactions of charged particles and capillary interactions of particles at liquid interfaces.

Let's have a more general look at the kinds of forces that are involved for particles adsorbed to a liquid interface

1.5 Interactions between colloids at liquid interfaces

1.5.1 Electrostatic forces

In general, forces that are responsible for particle interaction in the bulk are still relevant at an interface: gravity, electrostatic and magnetic forces. However, the presence of the interface implies that the properties of the medium around a colloidal particle are not

continuous (as in bulk) and change when crossing the interface from the first continuous phase to the second.

If we are dealing with a charged particle trapped at an interface between, let's say, oil and water, we have to account for the fact that the surface charge may not be equal at both sides of the particle. Moreover, due to differences in ion content in oil and water, the charges on the particle will be screened to different extents, as shown in Fig. 1.6. The result is that the particles will effectively repel as dipoles: stronger and with a longer range than the screened Coulomb interactions in aqueous bulk [25-27]. Moreover, if the surface charges of particles are not homogeneously distributed, this can lead to formation of in-plane (with the interface) dipoles; these exhibit end-to-end attraction and form chains of particles [28].

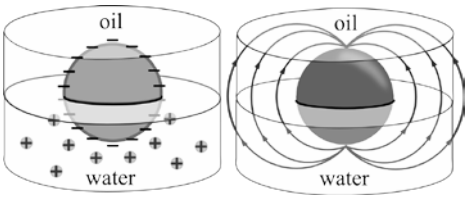

Figure 1.6. Asymmetric charge screening or asymmetric surface charge leads to dipolar behavior of a charged particle.

Another complication that can occur at liquid interfaces is that the electrostatic field will have different densities in phases with different permittivity. A denser electrostatic field will effectively push the particle towards the weaker field, thus deforming the interface in the particle's vicinity. This effect is called "electrodipping", and will be explained in more detail below.

1.5.2 Capillary forces

As mentioned above, the liquid interface itself can also exert significant forces on floating objects; these forces were called capillary forces. The earliest studies of capillary interactions between floating particles started in 1940s with works of Bragg [29] and Nicolson [30]. These works investigated air bubbles at the surface of soap solution. Nicolson argued that buoyancy force acting on a bubble deforms the water surface turning it into a small "hill", which is called meniscus. This makes nearby bubbles climb up this "hill" because of their own buoyancy. He also made a reverse argument for heavy particles made of material denser than water: they "roll" down the "hill" towards each other to decrease potential energy. Both cases result in an apparent attractive interaction. Nicolson's arguments are often referred to in modern works [31].

Let's have a more detailed look at particles that deform the interface locally. By doing so, they increase the interfacial area and, therefore, increase the surface free energy

of the interface. If two particles with similar deformation fields come close to each other, overlapping of their menisci leads to a decrease in the excess surface area and therefore also in the surface free energy. This means that it is more preferable for the particles to stay close together; this leads to an attractive interaction, as shown in Fig. 1.7a, b. The same reasoning can be applied to explain the repulsion between particles that have different deformation fields: depression and rising, as shown in Fig. 1.7c. Indeed, it was demonstrated experimentally that a particle that is heavier than water and one that is lighter than water repel each other [31].

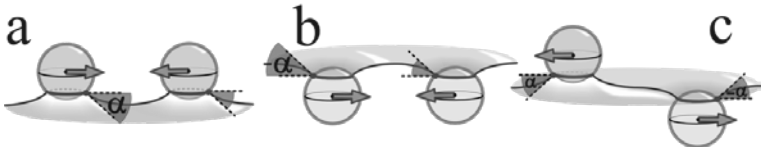

Figure 1.7. Interaction of particles due to overlapping of various deformation fields.

It is worth mentioning that sometimes in literature the term “capillary forces” may refer to the capillary bridging forces that act in the direction normal to the plane where the contact line lays (or at least major part of it), as shown in Fig. 1.8a. In this work we refer to the lateral capillary forces that act on a particle roughly in the plane in which the contact line lays as shown on Fig. 1.8b. Nevertheless, the nature of these forces is identical.

Figure 1.8. Difference between capillary forces due to bridging (**a**) and lateral (**b**) capillary forces.

1.6 Origins of interfacial deformations

Above, we have seen that capillary interactions between floating particles arise when the particles deform the liquid interface. Here, we discuss several possible reasons why such interface deformations can occur.

1.6.1 Deformation of an interface due to external forces acting on the particles

The nature of the external forces may vary; typically these are gravitational forces or forces induced by electric or magnetic fields; it can also be a force exerted on a particle by optical tweezers.

Gravity can induce deformation of the interface only if the particle is heavy enough. The gravitational pull on the particle must be counterbalanced by the net vertical component of the surface tension forces, acting on the contact line of a particle. This results in a perturbed interface around the particle. The particle size at which these deformations start to be noticeable can be estimated by calculating the Bond number, which compares gravitational forces acting on a particle with the surface tension forces:

$$B_0 = \frac{\Delta\rho g a^2}{\gamma}$$

Here $\Delta\rho$ is the density difference between the particle material and liquid, a is the particle radius and γ is the surface tension. It follows from this that a micrometer-sized polystyrene particle at an air-water interface will not significantly deform the interface, since: $B_0 \approx 10^{-7}$ the gravitational force can be neglected. Only for particles of 1 mm or larger, does gravity begin to play a role.

External electric or magnetic fields, if they are strong enough, can also force a particle upon which they act to deform the interface, as shown in Fig. 1.9.

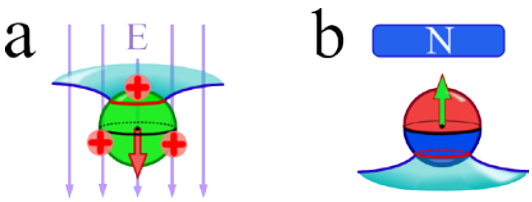

Figure 1.9. Deformation of an interface caused by external forces acting on particles: (**a**) electrostatic field pushing a positively charged particle down; (**b**) Magnetic field pushes a magnetic particle upwards and it drags the interface up.

Interestingly, charged particles can also push themselves into one of the two phases without an external field, under certain conditions. This phenomenon is called the "electrodipping effect" [32]. When a charged particle is placed at an interface between two phases with different relative permittivities $\varepsilon_1 < \varepsilon_2$, the density of the electric field that the particle generates is different in each phase: the electric field is denser in the phase with ε_1. The electrostatic pressure of the denser electric field effectively pushes the particle out of the phase with ε_1 into the phase with ε_2.

Recent observations showed that like-charged spherical colloidal particles trapped at a liquid interface could organize into hexagons due to long-range attractive interaction [18]. Since the gravitational pull on colloids cannot induce deformation of the interface (low Bond number), this attraction was explained with the electrodipping effect that causes deformation of the interface around a particle and creates a monopole around it, and

monopoles normally attract each other. However, this explanation was later reasoned to be inappropriate [19, 20]; thus this attraction is still not fully unexplained.

1.6.2 Deformation of an interface due to an irregular contact line

The surface of a particle is often not completely smooth. In this case, pinning of the contact line can lead to an irregular meniscus around the particle, which necessarily leads to a deformed interface. Whatever the precise shape of the undulations of the contact line is, they can be expressed as a series of Fourier modes:

$$C = \sum_m A_m \sin\big(m(t + \varphi_A)\big) + B_m \cos\big(m(t + \varphi_B)\big)$$

where m is the number of the modes. Interestingly, it was shown in [33], that at large distances from the particle, the quadrupolar mode (m = 2) always dominates. This leads to a far-field interaction between particles with four-fold symmetry. Only at shorter particle separations do higher modes start to become more significant.

1.6.3 Deformation of an interface due to particle shape anisotropy

The geometry of a particle can also deform the hosting interface in order to keep the contact line constant. One of the easiest ways to show an example of this without going into mathematical details is to study a particle with distinct differences in surface geometry, for example a dumbbell-shaped particle (see Fig. 1.10). This shape can be described as a surface of revolution of Ceva's trisectrix with the parameter b roughly between 0.3 - 0.7.

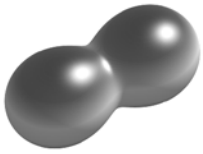

Figure 1.10. Anisotropic particle with a dumbbell shape.

Let's place such a particle on the air-water interface and let the contact angle θ be smaller than 90^0, as shown on the Fig. 1.11a (the contact angle is marked with red). Let's imagine that the curves *ab* and *cd* of the contact line are much longer than *ad* and *bc* (the neck is small). In this case they will play a major role in defining the vertical position of the particle (as described above), and the contact angle along them will be kept constant without deforming the interface. But along the curves *bc* and *ad* the contact angle cannot be kept constant and equal to θ without deforming the interface; the angle there will be smaller

than θ , if the interface remains flat, Fig. 1.11a (this angle is shown in brighter tone). To keep the contact angle the same, the interface there will be dragged onto the neck and the deformation field rises, as shown in Fig. 1.11b with the thick white contour. One would therefore expect a capillary interaction between dumbbells; this was indeed observed in our group (shown in Chapter 6).

If the contact angle $\theta \ll 90°$, the particle is situated deeper in water and the contact line is represented by two circles, and the contact angle along them is easily kept constant by changing the vertical position of the particle without deforming the interface, Fig. 1.11c.

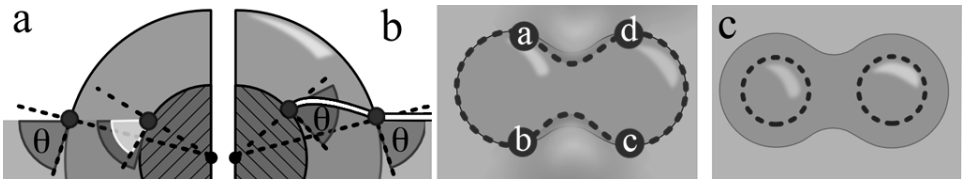

Figure 1.11. Shape anisotropy effect. (**a**) The contact angle β at the neck is less than α, if the interface is not deformed; (**b**) In order to make β equal to α the interface is deformed, and the curves *ad* and *bc* shift inwards; (**c**) The contact line is represented by two circles if $\theta \ll 90°$; no deformation field occurs.

Likewise, the liquid interface deforms around rod-like and ellipsoidal particles [34], as shown in Fig. 1.12. From the symmetry of the particles, it is clear that these deformations must lead to quadrupolar capillary interactions.

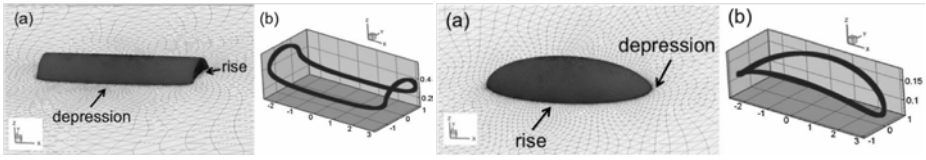

Figure 1.12. Contact lines of a cylinder and an ellipsoid. In order to keep the contact angle constant along the whole contact line the liquid interface needs to be deformed. Adopted from [34].

1.6.4 Deformation field induced by a particle at an interface with curved geometry

All examples given above involve the interface deformation induced by properties of the particles or external forces acting on the particle. Recent theoretical studies have shown, however, that even a spherical and completely smooth particle can deform a liquid interface, if the liquid interface itself is curved [16, 35]. At a flat (or isotropically curved) interface the contact line is a circle, which is axially symmetrical. The contact angle can be

adjusted simultaneously everywhere along the contact line due to the axial symmetry. But if the liquid interface is curved in an anisotropic way (Fig. 1.13a), the contact line is more complex (Fig. 1.13b), and whatever readjustment of the particle's vertical position we do, the contact angle cannot be constant everywhere along such a curved contact line. In order to meet the condition of constant contact angle, the interface has to be locally deformed as shown on Fig. 1.13c. There are rising (in horizontal direction) and depression (in vertical direction) fields along the directions of two local principal curvatures.

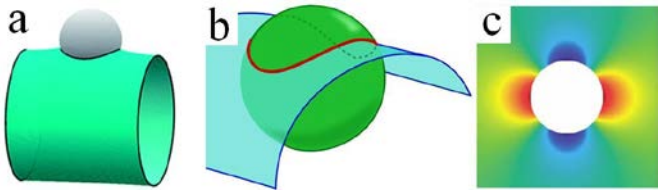

Figure 1.13. A spherical microparticle at a cylindrical interface (**a**), its contact line (red color) (**b**), and the quadrupolar deformation field induced by this particle (**c**). Adopted from [16].

Typical examples of curved interfaces studied theoretically are the cylinder and the catenoid; note that it is not mandatory that an interface has negative Gaussian curvature. In this thesis, we provide experimental proof for the existence of capillary interactions at curved interfaces.

1.7 Mobility of colloids at liquid interfaces

When there are objects present at liquid interfaces (like proteins, lipids, surfactants, and particles), the surface energy of this interface decreases because of the finite area that these object occupy at the interface. Thus such interfaces are more stable than those without any stabilizing additives. This phenomenon is widely used in foam and emulsion production, cosmetics, paints etc.

As a consequence of stabilizer addition, a liquid interface can become visco-elastic, and this property of interfaces plays an important role in foam and emulsion stability. There are many conventional methods of studying the rheology of liquid interfaces, which allow for determining shear and dilatational moduli of an interface [36].

For measuring the shear modulus there are interfacial rheometers that utilize shearing units with different geometries: du Nouy ring or DWR (double-wall ring), a needle, and cone-plate. They are all based on the same principle, in which a shear deformation is imposed to the interface and the resulting surface stress is measured.

For dilatational rheology the approach is different, because one needs to expand or compress the interface. The commonly used techniques are a Langmuir trough and a droplet tensiometer. They measure the change of surface tension of the dilated interface in

response to the dilation. From these two it is possible to calculate the dilatation modulus of the interface.

Recently, microrheology has been introduced as a tool for interfacial rheology. Originally microrheology was developed for studying rheology in the bulk of visco-elastic materials. The idea of this technique is to measure the mobility of microparticles in a medium of interest and to connect it to the visco-elastic properties of the medium through a generalized Stokes-Einstein relation [37]:

$$\tilde{G}(s) = \frac{k_B T}{\pi a s \langle \Delta \tilde{r}^2(\mathrm{s}) \rangle}$$

where a is particles' radius, $\langle \Delta \tilde{r}^2(s) \rangle$ is Laplace transform of time-dependent mean-square displacement.

One-point microrheology, where the MSD of individual particles is measured, is easy to use, but it reports values of shear moduli that are often not consistent with those obtained from conventional rheometers. This discrepancy is probably due to inhomogeneities in the medium, and to a depletion zone around the particles, leading to a local environment that differs from the average medium. To avoid this problem two-point microrheology was developed [38]; it measures the cross-correlated motion between a pair of tracer particles, thus effectively probing the entire medium that is between them, including all inhomogeneities. Shear moduli reported by two-point microrheology are consistent with those obtained with conventional rheometers.

Microrheology has a number of potential advantages over traditional rheology. It requires only very small sample volumes, it gives local information, and it can probe much higher frequencies.

Microrheology can also be applied to probe the visco-elastic properties of liquid interfaces. However, several complications must be considered when interpreting the mobility of particles at interfaces. The effective drag that a particle experiences at a liquid interface is not only determined by the properties of the interface, but also by the viscosities of the subphase and the superphase. Extracting the viscous and elastic properties of the interface is hard, especially when the surface viscosity and elasticity are low [39, 40].

Another complication is that the flow of liquid around a particle is disturbed by the presence of the interface. In case of a particle situated in a continuous medium (bulk microrheology), the Navier-Stokes equations can be solved to obtain the viscous drag on the particle. For interfacial flows, which in general couple to the bulk flows, this is more difficult [21, 41].

Finally, to understand the mobility of particles trapped at an interface, we need to account for the various interparticle interactions at an interface, which can be very long-ranged, as discussed above.

1.8 Aim of this research

The initial aim of this research was to study the visco-elastic properties of thin networks of actin filaments attached to an interface. Such networks can be seen as a model system for the cytoskeletal cortex in animal cells. In the last decades, a lot of progress has been made in understanding the mechanical properties of bulk actin networks. However, the properties of thin actin networks have not been studied in much detail yet. To tackle this problem we anchored actin filaments to liquid interfaces (oil droplets in water), constructing a thin "2D" actin network.

To characterize the mechanical properties of these actin networks, we used microrheology: microparticles were deposited at the actin-covered interfaces and their mobility was followed and related to the network properties.

While studying the mobility of particles at liquid interfaces, we learned that the behavior of the particles was strongly affected by the curvature of the interface. It turned out that particles at such interfaces have very long-ranged and anisotropic interactions. We therefore decided to study these interactions and the organizations that they lead to in more detail. As a result, this thesis consists of two parts: one part dealing with capillary interactions between particles at curved liquid interfaces and a second part dealing with the mobility of particles at a complex liquid interface.

1.9 Outline of this thesis

This thesis deals with two aspects of the behavior of particles at liquid interfaces and therefore consists of two parts. The first part is dedicated to the experimental observation and the theoretical study of capillary interactions between particles trapped at curved oil-water interfaces. The second part is about the dynamics of such particles and how these can be used as a tool to study interfacial properties. We then apply this to a special kind of surface, which mimics the interior of a living cell.

Part I "Organization". In Chapter 2 we present an experimental observation of the behavior of spherical colloidal particles at curved liquid interfaces. We study the capillary interaction between the particles arising from the curvature of the interface and how this interaction affects the organization of the particles. To explain this interaction, in Chapter 3 we numerically solve the Young-Laplace equation for the shape of a curved interface in the vicinity of a particle and find the deformation profile around it (meniscus). We show how particles experience a capillary interaction via these menisci and study how the capillary term of the pair interaction potential behaves for different interfacial curvatures, particle sizes, distances between them, and at which condition it may result in ordering. We compare the results of the numerical calculations with the experimental findings of Chapter 2 and discuss the feasibility of the calculations.

Part II "Mobility". Chapter 4 deals with the dynamics of colloidal particles at an interface with visco-elastic properties. We prepare interfaces covered with colloidal particles at different densities and add tracer particles. The mean square displacement of the particles is related to the viscous and elastic properties of the particle monolayer. In chapter 5, we use the same method to probe the visco-elastic properties of thin actin networks attached to a liquid interface. Such actin networks mimic the actin cortex in living cells. We probe the mechanical properties of the networks in the presence of varying amounts of cross-linkers and motor proteins.

General discussion. In the final Chapter of this thesis we discuss how the findings of this thesis contribute to understanding the behavior of microparticles trapped at liquid interfaces; we also discuss where and how these findings might be used in future studies.

References

1. Pickering, S.U., *CXCVI.-Emulsions.* Journal of the Chemical Society, Transactions, 1907. **91**(0): p. 2001-2021.
2. Dinsmore, A.D., et al., *Colloidosomes: Selectively permeable capsules composed of colloidal particles.* Science, 2002. **298**(5595): p. 1006-1009.
3. Frelichowska, J., et al., *Pickering w/o emulsions: Drug release and topical delivery.* International Journal of Pharmaceutics, 2009. 368(1-2): p. 7-15.
4. Tadros, T.F., Colloids in Cosmetics and Personal Care. 2008: Wiley.
5. Kargar, M., et al., *Investigation into the potential ability of Pickering emulsions (food-grade particles) to enhance the oxidative stability of oil-in-water emulsions.* Journal of Colloid and Interface Science, 2012. **366**(1): p. 209-215.
6. Ata, S., *Phenomena in the froth phase of flotation - A review.* International Journal of Mineral Processing, 2012. **102**: p. 1-12.
7. Ross, V.E., *Particle-bubble attachment in flotation froths.* Minerals Engineering, 1997. **10**(7): p. 695-706.
8. Isa, L., et al., *Particle Lithography from Colloidal Self-Assembly at Liquid-Liquid Interfaces.* Acs Nano, 2010. **4**(10): p. 5665-5670.
9. Frye, G.C. and J.C. Berg, *Antifoam Action by Solid Particles.* Journal of Colloid and Interface Science, 1989. **127**(1): p. 222-238.
10. Kralchevsky, P.A. and K. Nagayama, *Capillary interactions between particles bound to interfaces, liquid films and biomembranes.* Advances in Colloid and Interface Science, 2000. **85**(2-3): p. 145-192.
11. Lewandowski, E.P., et al., *Orientation and Self-Assembly of Cylindrical Particles by Anisotropic Capillary Interactions.* Langmuir, 2010. **26**(19): p. 15142-15154.
12. Botto, L., et al., *Capillary interactions between anisotropic particles.* Soft Matter, 2012. **8**(39): p. 9957-9971.
13. Loudet, J.C., et al., *Capillary interactions between anisotropic colloidal particles.* Physical Review Letters, 2005. **94**(1).
14. Park, B.J., T. Brugarolas, and D. Lee, *Janus particles at an oil-water interface.* Soft Matter, 2011. **7**(14): p. 6413-6417.
15. Lewandowski, E.P., et al., *Rotation and alignment of anisotropic particles on nonplanar interfaces.* Langmuir, 2008. **24**(17): p. 9302-9307.
16. Zeng, C., et al., *Capillary interactions among spherical particles at curved liquid interfaces.* Soft Matter, 2012. **8**(33): p. 8582-8594.
17. Furst, E.M., *Directing colloidal assembly at fluid interfaces.* Proceedings of the National Academy of Sciences of the United States of America, 2011. **108**(52): p. 20853-20854.
18. Nikolaides, M.G., et al., *Electric-field-induced capillary attraction between like-charged particles at liquid interfaces.* Nature, 2002. **420**(6913): p. 299-301.
19. Megens, M. and J. Aizenberg, *Like-charged particles at liquid interfaces.* Nature, 2003. **424**(6952): p. 1014-1014.

20. Nikolaides, M.G., et al., *Like-charged particles at liquid interfaces - Reply.* Nature, 2003. **424**(6952): p. 1014-1014.
21. Levine, A.J. and F.C. MacKintosh, *Dynamics of viscoelastic membranes.* Physical Review E, 2002. **66**(6).
22. Loudet, J.C. and B. Pouligny, *How do mosquito eggs self-assemble on the water surface?* European Physical Journal E, 2011. **34**(8).
23. Hu, D.L. and J.W.M. Bush, *Meniscus-climbing insects.* Nature, 2005. **437**(7059): p. 733-736.
24. Yu, Y., et al., *Meniscus-climbing behavior and its minimum free-energy mechanism.* Langmuir, 2007. **23**(21): p. 10546-10550.
25. Pieranski, P., *Two-Dimensional Interfacial Colloidal Crystals.* Physical Review Letters, 1980. **45**(7): p. 569-572.
26. Hurd, A.J., *The electrostatic interaction between interfacial colloidal particles.* Journal of Physics A: Mathematical and General, 1985. **18**(16): p. L1055.
27. Park, B.J. and E.M. Furst, *Attractive interactions between colloids at the oil-water interface.* Soft Matter, 2011. **7**(17): p. 7676-7682.
28. Chen, W., et al., *Long-ranged attraction between charged polystyrene spheres at aqueous interfaces.* Physical Review Letters, 2005. **95**(21).
29. Bragg, L. and J.F. Nye, *A Dynamical Model of a Crystal Structure.* Proceedings of the Royal Society of London. Series A. Mathematical and Physical Sciences, 1947. **190**(1023): p. 474-481.
30. Nicolson, M.M., *The interaction between floating particles.* Mathematical Proceedings of the Cambridge Philosophical Society, 1949. **45**(02): p. 288-295.
31. Vella, D. and L. Mahadevan, *The "Cheerios effect".* American Journal of Physics, 2005. **73**(9): p. 817-825.
32. Boneva, M.P., et al., *Attraction between Particles at a Liquid Interface Due to the Interplay of Gravity- and Electric-Field-Induced Interfacial Deformations.* Langmuir, 2009. **25**(16): p. 9129-9139.
33. Stamou, D., C. Duschl, and D. Johannsmann, *Long-range attraction between colloidal spheres at the air-water interface: The consequence of an irregular meniscus.* Physical Review E, 2000. **62**(4): p. 5263-5272.
34. Botto, L., et al., *Capillary bond between rod-like particles and the micromechanics of particle-laden interfaces.* Soft Matter, 2012. **8**(18): p. 4971-4979.
35. Wurger, A., *Curvature-induced capillary interaction of spherical particles at a liquid interface.* Physical Review E, 2006. **74**(4).
36. Miller, R. and L. Liggieri, *Interfacial Rheology*. 2009: Taylor & Francis.
37. Mason, T.G. and D.A. Weitz, *Optical Measurements of Frequency-Dependent Linear Viscoelastic Moduli of Complex Fluids.* Physical Review Letters, 1995. **74**(7): p. 1250-1253.
38. Crocker, J.C., et al., *Two-point microrheology of inhomogeneous soft materials.* Physical Review Letters, 2000. **85**(4): p. 888-891.

39. Saffman, P.G. and M. Delbrück, *Brownian motion in biological membranes.* Proceedings of the National Academy of Sciences, 1975. **72**(8): p. 3111-3113.
40. Petrov, E.P. and P. Schwille, *Translational diffusion in lipid membranes beyond the Saffman-Delbruck approximation (vol 94, L41, 2008).* Biophysical Journal, 2012. **103**(2): p. 375-375.
41. Prasad, V., S.A. Koehler, and E.R. Weeks, *Two-particle microrheology of quasi-2D viscous systems.* Physical Review Letters, 2006. **97**(17).

CHAPTER 2

CAPILLARITY-INDUCED ORDERING OF SPHERICAL COLLOIDS ON AN INTERFACE WITH ANISOTROPIC CURVATURE

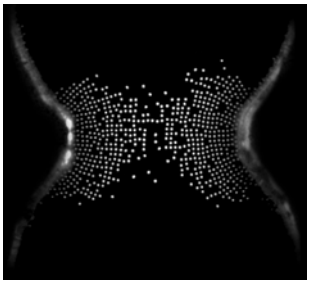

In this Chapter we study the behavior of spherical colloidal particles deposited at anisotropically curved liquid interfaces. We present experimental observations on how the curvature of the interface affects the interactions between the particles and forces them to organize into square lattices. We demonstrate that the strength of the anisotropic interactions depend on the deviatoric curvature (defined below) alone, irrespective of the exact shape of the liquid interface. These observations suggest that anisotropic interactions can easily be induced between isotropic colloids through tailoring of the interfacial curvature.

This chapter is based on: Dmitry Ershov, Jeroen Appel, Joris Sprakel, Jasper vander Gucht, Martien Cohen Stuart, "Capillarity-induced ordering of spherical colloids on an interface with anisotropic curvature", PNAS, 2013.

2.1 Introduction

Colloidal self-assembly is a promising route towards the fabrication of new micro-structured materials. Examples of assembly in 3D include the formation of well-defined clusters [1] or complex colloidal crystals [2] using particles decorated with “sticky” patches. In such cases formation of the superstructures relies on the use of particles that have patches of distinct chemical functionality at their surface [3-5]. In another study, magnetic cores were introduced into particles during their synthesis to drive their interaction and assembly [6]. Such methods are effective, but synthesizing monodisperse, chemically modified particles is difficult and often yields only small quantities [7, 8].

Another bottom-up approach to control colloid self-assembly is to make use of anisometric particles [5, 9-11], where the shape of the particles dictates their organization.

Inducing anisotropic interactions between isotropic spherical particles requires the imposition of a directional external field or a template. This has been achieved through application of electric or magnetic fields [12, 13] or by immersing the particles in anisotropic fluids [14].

An alternative strategy is based on using interfaces to direct self-assembly. Microparticles can be trapped at liquid interfaces [15], and under certain conditions, these adsorbed particles might order in regular patterns. This ordering depends on the strength and directionality of the particle-particle interactions. It is possible to control these interactions by using particles with chemically modified surfaces [16, 17] or by using external fields (flows of liquids, electric fields) [18-20]. Besides these methods, there is another type of interaction, which is unique to liquid interfaces: capillary interaction [21].

Capillary forces are directionally anisotropic for particles with anisotropic shape [22-24], leading to direction-specific interaction and organization. Recent findings show that spherical particles can generate anisotropic (quadrupolar) forces that lead to specific organization too [25-27]. While liquid interfaces could be suited as a template for self-assembly of microparticles [28], control over the directionality of the interactions is still lacking so far.

Colloidal particles adsorb strongly to interfaces formed between two immiscible phases: liquid-liquid (oil-water) or gas-liquid (air-water) interfaces. This adsorption is favorable because it reduces the surface energy; even for a small micrometer-sized particle trapped at the air water interface, the adsorption energy can be as large as 10^7 kT, thus making particle adsorption essentially irreversible. If there are enough particles at the interface, so that the separation between them allows for different types of interaction to occur, they may organize into regular structures. This organization is largely determined by inter-particle interactions.

Isotropic repulsion, for example by electrostatic forces, leads to crystallization into a hexagonal lattice, once the particle density is high enough [29]. If the particles locally deform the interface (for various reasons described in Chapter 1), capillary interactions arise [30, 31]. The deformations increase the area of the interface leading to an unfavorable increase in surface free energy. When two particles approach each other, so that the

deformations that they induce overlap, the total change in area may be reduce or increased depending on the relative sign of the two deformations. Therefore the capillary interaction between two particles can be both repulsive and attractive in case of a complex deformation field.

Macroscopic objects floating at a flat liquid interface (such as breakfast cereals floating in a bowl of milk or bubbles at the surface of a soft drink) are heavy (or light) enough to cause deformation of the interface. As a result they clump together due to capillary attraction arising from menisci interaction: these deformations cause excess surface area that can be reduced if the particles move closer together. For micrometer-sized colloids, however, the gravitational force is too small to produce significant interfacial deformations, so that capillary forces between spherical colloids at a flat interface are negligible.

With a particle trapped at a liquid interface one can associate a Bond number B_0 that characterizes the ratio between the gravitational and interfacial energy $B_0 = \Delta\rho g a^2/\gamma$, where a is the radius of the particle, $\Delta\rho$ is the density difference for the particle material and the liquid, and γ is the interfacial tension of the liquid. For a micrometer-sized polystyrene particle trapped at the air-water interface, B_0 would be approximately 10^{-8}, meaning that the gravitational energy is negligible compared to the surface energy, and therefore no significant deformation occurs [32].

For colloidal particles of negligible weight, interface distortions can be caused by particle shape anisotropy [23, 33-35] or by surface heterogeneities [36]. In both cases, the undulating contact line induces orientation-dependent attractions and repulsions, causing particles to assemble with preferred orientations. Smooth, spherical colloids, however, can insert themselves in a flat interface without distorting it. The condition of a constant contact angle along the three-phase contact line, as required by Young's law, can be satisfied simply by changing the vertical position of the particle. Such particles therefore do not experience any tangential forces at a flat interface.

The situation changes, however, if the liquid interface is not flat, but has an anisotropic curvature (that is, if the two principal curvatures are locally different). In this case, it is no longer possible for an adsorbed particle to satisfy a uniform contact angle along the contact line without distorting the interface. Capillary interactions between spherical colloids arising because of such deformations have been predicted to be anisotropic [25, 26], but until now have not been rigorously investigated experimentally. Here, we investigate how these interactions govern the self-assembly of particles adsorbed to interfaces of various different shapes. We study the organization of the particles and identify the characteristic measure for the interfacial shape that determines how the particles order.

2.2 Experimental details

2.2.1 Materials and methods

We worked with core-shell particles consisting of a fluorescent polystyrene core and a shell of poly(n-isopropyl acrylamide-co-methacrylic acid); the particles where synthesized adopting a protocol described in [37]. After synthesis of a fluorescent polystyrene core particle through emulsion polymerisation, with a diameter of approximately 300 nm and polydispersity <5%, dyed with Pyromethene 546 (Exciton, Dayton (OH) USA), a non-fluorescent microgel shell was grown through precipitation co-polymerization of n-isopropylacrylamid (93 wt%), methacrylic acid (5 wt%) and the crosslinker bismethacrylamide (2 wt%). After extensive washing of the particles against DI water, they are stored as a concentrated stock suspension at 4˚C. The final size of the core-shell particle was determined by dynamic light scattering and is 1.5 μm.

Droplets with anisotropic curvature were prepared on substrates with patterned wettability. We prepare this through soft photolithography (see Fig. 2.1a); first a 25 μm thick layer of SU-8 photoresist is spin coated on a glass slide, which is then selectively cross-linked through a photomask. After washing the substrate with propylene glycol methyl ether acetate (Sigma Aldrich), we obtain slides with wells in a 25 μm thick layer of hydrophobic photoresist. Then 5 μl of oil (Sigma Aldrich, Heavy Mineral) was deposited on the substrate and treated with weak air stream to remove excessive oil, leaving oil droplets only in the wells. Then, 200 μl of an oil-in-water emulsion (2 %v/v) stabilized by the colloidal particles was carefully placed on top (Fig. 2.1b). The emulsion droplets fused with the droplets in the wells, after which the particles could spread over the oil/water interface. Because the contact line of the oil droplet is pinned strongly to the edge of the well, the shape of the interface is determined completely by the shape of the well and the volume of the droplet. Each slide contains approximately 20-40 droplets of various shapes. To prevent evaporation, samples were sealed in a glass chamber. The whole process is illustrated in Fig. 2.1.

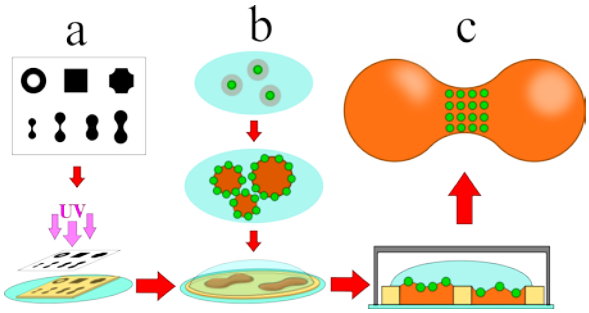

Figure 2.1. Wells of defined shape made by soft photolithography (**a**); oil droplets (orange) stabilized by core-shell particles (green-grey) are deposited into the wells and sealed (**b**); square lattices form on curved interfaces (**c**).

Samples were imaged using a Zeiss Axiovert 200M-Exciter confocal laser-scanning microscope, using a 100x/1.4NA oil immersion objective. The pinhole was 60 μm, corresponding to a slice thickness of 0.4 μm. Three-dimensional image stacks are obtained and analyzed as described below.

2.2.2 Analysis of images and geometry

The resulting image sequences were analyzed using a MatLab script for 3D particle tracking from the M. Kilfoil lab [38, 39]. Centroids of the particles were determined in 3 dimensions; the resolution of the tracking algorithm is approximately 20 nm in plane and 50 nm in the z-direction [38]. With this procedure 3-dimensional particle coordinates were obtained; occasional particles that were not at the interface were excluded from the analysis. The coordinates of the particles trapped at the interface were interpolated in order to obtain a smooth numerical description of the liquid interface, using an interpolation MatLab routine [40].

For any surface described in parametric form in the Monge gauge, the position on the surface can be given by $\vec{r} = \big(u, v, h(u,v)\big)$ [41]. The normal to the surface at this point is then given as a normalized cross-product of two tangential vectors $\vec{r}_u = \partial\vec{r}/\partial u$ and $\vec{r}_v = \partial\vec{r}/\partial v$:

$$\vec{n} = \frac{\vec{r}_u \times \vec{r}_v}{|\vec{r}_u \times \vec{r}_v|} \qquad 2.1$$

and the curvature of the surface at this point as

$$k = \frac{d\vec{r} \cdot d\vec{n}}{d\vec{r} \cdot d\vec{r}} \qquad 2.2$$

where $d\vec{r} = \vec{r}_u du + \vec{r}_v dv$ is a vector on the surface connecting two infinitesimally separated points. From Equation 2.2 it is clear that for each direction in the surface, $d\vec{r}$, there is a value of the curvature. Two extreme values (one minimal and one maximal) of k can be found and their corresponding direction too; these are called the principal curvatures and principal directions. The principal directions are orthogonal and define the extrema of the curvatures.

By using the obtained smooth numerical description of the interface and analyzing it according to [41] we are able to calculate the principal curvature values k_1 and k_2 and the corresponding principal directions at any point of interest, namely any particle position.

2.3 Results and discussion

2.3.1 General observation

The core-shell particles that we synthesize, are stabilized with negative charges and don't aggregate in the bulk water. As described by Pieranski [29], such particles, when deposited at an oil-water interface, repel each other even stronger than in a continuous medium, because the asymmetric charging of the particle leads to dipole-dipole repulsive interactions.

Our particles indeed repel each other and don't show signs of attractive interaction, if the interface they are deposited at is flat. To show that this is the case for long times, we record a movie of particles at low surface density and show the probability distribution of inter-particle separations, Fig. 2.2a,b.

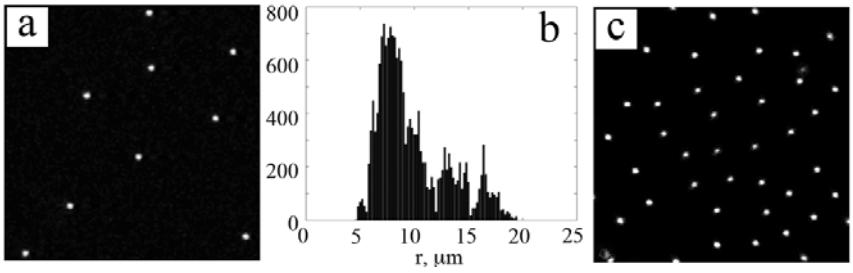

Figure 2.2. Particles at a flat oil-water interface. **(a)**: At low surface density with **(b):** The histogram of inter-particle separations for (a), sampled for 5 minutes. **(c):** At intermediate surface density.

For the time of observation of ~5 minutes, the particles don't seem to have a tendency to approach each other; at higher surface densities they also don't aggregate and show repulsive interaction, forming transiently stable patterns (Fig. 2.2c). At even higher concentration they form the well-known hexagonal packing (not shown).

However, if the oil-water interface is not flat but has an anisotropic curvature, the particles are observed to form pairs or strings of multiple particles (Fig. 2.3a). This indicates the presence of a long-ranged attraction between the particles.

In this case, analysis of the movies reveals a strong peak in the probability distribution of inter-particle separation at a distance ~ 2 μm, which means that this separation is conserved throughout the whole movie. At intermediate surface density the particles show a stable organization into a square pattern (Fig. 2.3c). At even higher surface densities this structure is replaced by a hexagonal packing, as will be discussed below.

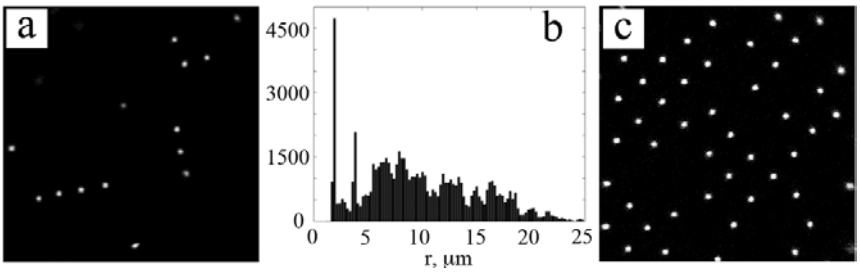

Figure 2.3. Particles at a flat oil-water interface. **(a)**: At low surface density with **(b):** The histogram of inter-particle separations for (a), sampled for 5 minutes. **(c):** At intermediate surface density.

2.3.2 Effect of the shape of the interface

To study the organization more systematically, we create oil/water interfaces of different shape by depositing oil droplets on glass slides patterned with hydrophobic patches and covering these with a layer of water. Due to strong pinning of the oil droplets on the hydrophobic patches, the droplets assume a shape, which is completely determined by the shape of the hydrophobic patch and the volume of the oil droplet. We then add colloidal particles that consist of a fluorescently labeled polystyrene core and negatively charged shell, with a total radius $a = 0.75$ μm.

The organization of the particles on the oil/water interface is monitored using confocal microscopy. Figure 2.4 shows maximum intensity projections of confocal z-stacks for droplets of various different shapes. On non-spherical droplets, the particles self-organize into ordered patterns, even when the coverage of the interface is still low, as shown for a variety of droplet shapes, ranging from dumbbells (Fig. 2.4c), rounded squares (Fig. 2.4d), toroids (Fig. 2.4e) and prolate ellipsoids (Fig. 2.4f). On all these interfaces, the particles organize into an unusual square lattice (inset of Fig. 2.4f), which implies that the inter-particle interactions must be anisotropic.

Once adsorbed to the interface, the particles are no longer affected by gravity, because the Bond number $B_0 \approx 10^{-8}$. The interactions we observe are thus not caused by gravitational deformation of the interface, as observed for macroscopic objects [32]. Another possible cause of capillary interactions is an undulating contact line due to pinning at irregularities at the particle surface [38]. However, this would give rise to particle clustering also on flat surfaces, which is not what we observe experimentally (Fig. 2.4a). For the same reason we can exclude capillary interactions caused by the electrodipping effect due to an asymmetry in the electric field [42], which is still controversial [43, 44]. Instead, we argue that the ordering is caused by the anisotropic curvature of the interface. Indeed, it has been predicted theoretically that particles embedded in an anisotropic interface experience quadrupolar capillary interactions [25], because the constraint of a constant contact angle along the particle perimeter can only be satisfied if the interface deforms (see Chapter 3).

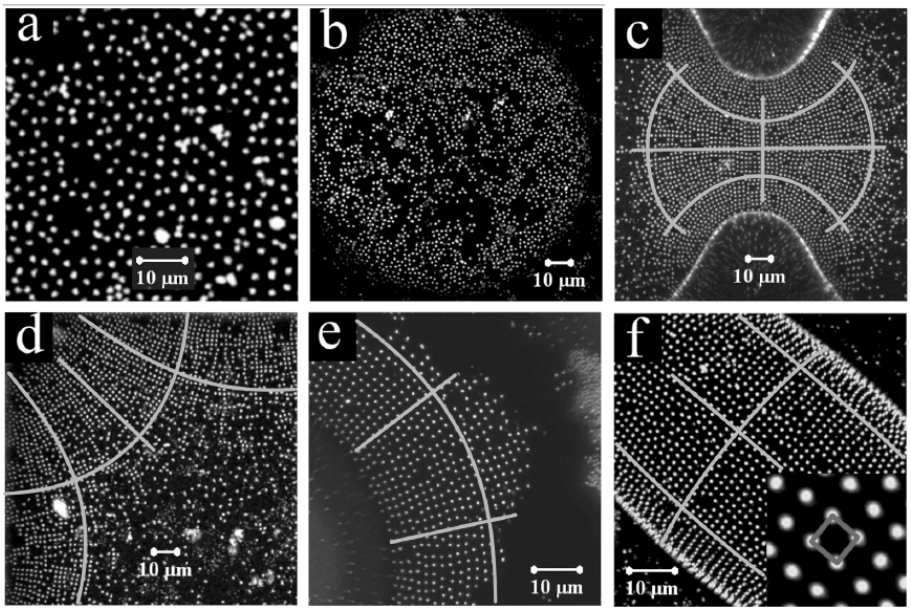

Figure 2.4. Particle organizations on oil/water interfaces of different shape. Maximum intensity projections of confocal z-stacks, showing fluorescently labeled particles on **(a)** a flat interface, **(b)** a spherical interface, **(c)** a dumbbell-shaped droplet, **(d)** a droplet pinned to a square patch (only one corner is shown), **(e)** a toroid-shaped droplet, and **(f)** a prolate ellipsoid. Inset in (f) shows square lattice organization. Scale bar indicates10 μm in all images. Grey lines in c-f indicate the directions of principal curvature.

2.3.3 Deviatoric curvature

The images in Fig. 2.4 suggest that the ordering of the particles is related to the anisotropic shape of the interface. To study this relation more quantitatively, we need to find a quantity that characterizes the local shape anisotropy.

The mean curvature $H = (k_1 + k_2)/2$ (k_1 and k_2 are the local principal curvatures) clearly is not a proper parameter to characterize the organization, because no ordering is found on spherical droplets of different H. Only at very high densities do the particles organize into a hexagonal pattern, so as to minimize excluded volume interactions. The characteristic quantity that determines the square lattice organization is also not the Gaussian curvature $K = k_1 k_2$. Particle ordering occurs in regions of negative Gaussian curvature (for instance the toroid in Fig. 2.4e and the dumbbell in Fig. 2.4c), in some regions of positive Gaussian curvature (prolate ellipsoid on Fig. 2.4f), while on a spherical ($K > 0$) interface no ordering is found.

Instead, we argue that the relevant parameter that governs particle ordering is the deviatoric curvature, defined as $D = |k_1 - k_2|/2$. The deviatoric curvature is an invariant

of the curvature tensor and is the simplest measure for the anisotropy of the interfacial curvature; it is larger than zero, whenever the two principal curvatures are unequal. It should be noted that, in contrast to the mean curvature, the deviatoric curvature D is not a constant for a given droplet, but varies spatially.

A typical result showing a surface mapped with its deviatoric curvature is shown in Fig. 2.5. The principal curvature directions at each particle's position are shown as black lines. It can be seen how particles are dispersed in the area where $D < 0.002$ μm^{-1} (upper right corner), while above this threshold they organize into square lattices (lower left corner).

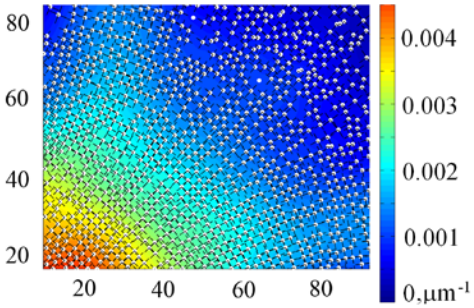

Figure 2.5. A surface mapped with its deviatoric curvature D. The vertical color bar indicates the values of D in μm^{-1}. Axes give relative position of the particles in μm.

2.3.4 Characterization of patterns and choosing neighbors

Each type of crystallization has its own spatial organization of particles into unique patterns. The radial distribution function $g(r)$ shows how the distance from the center of a randomly chosen particle affects the probability of finding another particle. The shape of this function can serve as a fingerprint for the type of organization.

We calculate this function for all the particles present at a curved liquid interface and compare it to the fingerprint of a square lattice, shown in Fig. 2.6a. It shows distinct peaks characteristic for a square lattice: at $1S$, $\sqrt{2}S$, $2S$, and $\sqrt{5}S$ times the lattice spacing S. For 15 different interfaces the ensemble average spacing varies from $S = 1.75$ to 2.1 μm, with the average equal to 1.9 μm. It is larger than the particle diameter measured in water with dynamic light scattering, $a = 1.5$ μm.

This suggests that there is a distance of approximately 400 nm between the particles' surfaces. Apparently, the capillary attraction is balanced by a long-ranged repulsive interaction between the particles, so as to give a minimum at finite separation distance. This repulsive contribution to the interaction potential may be an electrostatic repulsion, which can be very long-ranged for particles at an interface due to asymmetric charging of the particle surface [29].

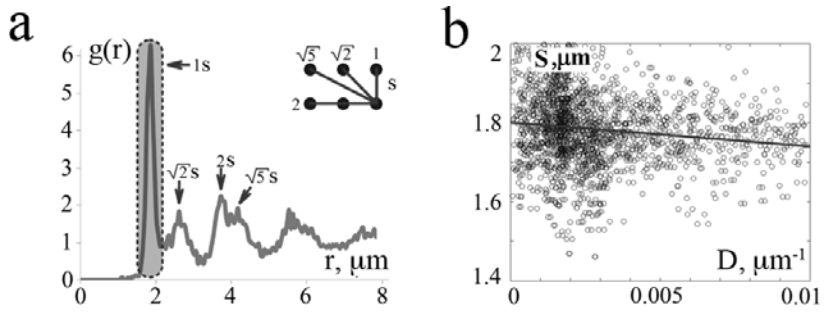

Figure 2.6. Radial distribution function *g(r)* for particles on a dumbbell-shaped interface and for particles on a flat interface. On the anisotropic interface, *g(r)* shows the characteristic peaks for a square lattice organization, at *1S*, *√2S*, *2S*, and *√5S* times the lattice spacing, which is S = 1.9 μm in this particular example.

The position of the peak corresponding to *1S* seems to vary weakly with the deviatoric curvature *D*, as shown by the red linear fit in Fig. 2.6b. This supports the hypothesis that the strength of the capillary interaction depends on the deviatoric curvature, and in this case the shorter particle separation indicates stronger attraction at higher *D*. To further analyze the ordering, we first need to identify the nearest neighbors of each particle. The common way of finding the nearest neighbor of a particle is to set a threshold for the separation distance equal to the distance at which the first peak in $g(r)$ appears. In our case this approach fails, since the position of this peak subtly varies depending on the local shape of the interface, for which $g(r)$ has been calculated, Fig. 2.6b.

This means that setting one threshold for the whole interface and finding neighbors within this threshold would give erroneous results. To avoid this, we locally calculate $g_i(r)$ around each i^{th} particle using only positions of its neighbors within 5 diameters (7.5 μm) and set the threshold for finding the closest neighbors according to the peak in $g_i(r)$. This approach gives more plausible results that are also visually confirmed.

2.3.5 Alignment of square lattices with the principal curvature directions. Effect of the deviatoric curvature on alignment.

It can be noticed that the bonds between neighboring particles tend to align along the principal curvature axes of the interface. For example, in Fig. 2.7a, all inter-particle bonds in the cylindrical region in the middle of the droplet are either along the long axis or along the short axis of the droplet.

To quantify these observations, we find the local principal curvature directions P_1 and P_2 in the vicinity of each particle (they correspond to minimal and maximal local curvatures), and measure the probability distribution of angles ϕ between each inter-particle bond and the local principal directions, as shown in Fig. 2.7b. The distribution has strong peaks at 0 and 90 degrees, as expected for alignment along the perpendicular

principal axes. This indicates that the particles attract each other most strongly when they approach each other along one of the principal axes, in agreement with theoretical predictions made by Wurger [25] and those described in Chapter 3.

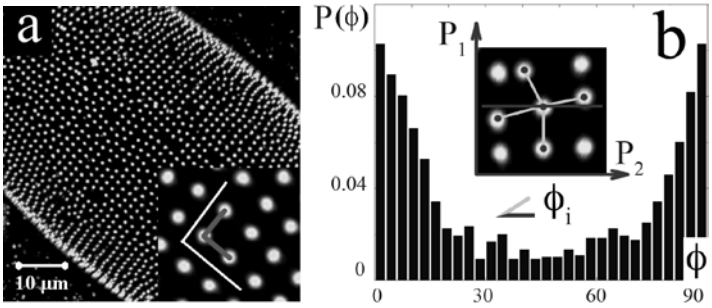

Figure 2.7. (**a**): Organization of particles on a prolate ellipsoid. Inset: alignment of the inter-particle bonds (thick grey lines) with the ellipsoid axes (thin white lines). (**b**): Probability distribution of angles ϕ for all particles on the ellipsoid. Inset: angle ϕ_i is formed by an inter-particle bond (white lines) and two local principal directions P_1 and P_2.

The distribution in Fig. 2.7b suggests that we can quantify the degree of ordering with an order parameter $\langle cos(4\phi)\rangle$, which is unity when all inter-particle bonds are aligned with either of the two principal axes (ϕ = 0 or 90 degrees), and zero for a random organization. For the distribution shown in Fig. 2.7b, the order parameter $\langle cos(4\phi)\rangle$ = 0.6, which appears to be the maximal value achievable in our experimental setup. An example of mapping the particles with the values of the order parameter is shown in Fig. 2.8.

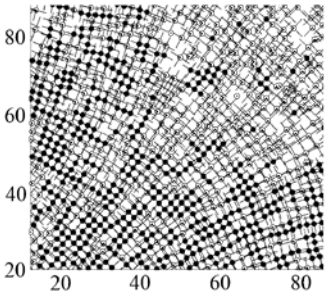

Figure 2.8. Particles at a curved oil-water interface pinned in a square well (left lower corner is shown). The particles are colored according to $\langle cos(4\phi)\rangle$: dark for values higher than 0.6, light for values lower than 0.6.

To test how the deviatoric curvature affects particle organization, we plot in Fig. 2.9 the order parameter $\langle cos(4\phi)\rangle$ as a function of D for droplets of different shapes. We find that the data for different droplet shapes indeed collapses on one master curve. For $D < 0.002$ μm^{-1} the order parameter $\langle cos(4\phi)\rangle$ is small, which indicates a random particle

distribution. As D increases, the order parameter increases nearly linearly, and for $D > 0.003\ \mu m^{-1}$, it reaches a plateau of approximately 0.6. These findings indicate that the capillary interaction between the particles becomes stronger as the deviatoric curvature increases.

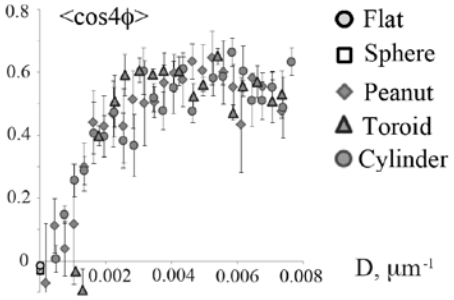

Figure 2.9. Order parameter $\langle cos(4\phi)\rangle$ as a function of the deviatoric curvature D for droplets of different shape. Average values and standard deviations are shown, obtained for ~4000 particles on 3 different droplets for the shapes with $D > 0$ and for ~2000 particles on 1 droplet for the shapes $D = 0$.

2.3.6 Effect of the deviatoric curvature on pair interaction potential

The pair interaction potential can give us information about the mobility of particles inside a crystal, thus telling us about its stability [42]. To see the effect of curvature on the stability of square lattices we extract the local confining potential from the probability distribution $P(r)$ of the center-to-center distance r between neighboring particles in the lattice, by tracking all particles for several minutes. From this distribution, we estimate the potential well $V(r)$ of a particle in the lattice by inverting the Boltzmann distribution $P(r) \propto e^{-V(r)/kT}$.

Figure 2.10 shows the resulting potential for interfaces with two different values of D. Both potentials have a parabolic shape and can be fitted to the expected confining potential of a harmonic oscillator to extract an effective spring constant for the particle bonds. As D increases, the minimum of the potential shifts to smaller separations, while the effective spring constant increases from 1.4 μN/m for $D = 0.007\ \mu m^{-1}$ to 8.2 μN/m for $D = 0.016\ \mu m^{-1}$. This can be ascribed to an increase in the capillary attraction with increasing D.

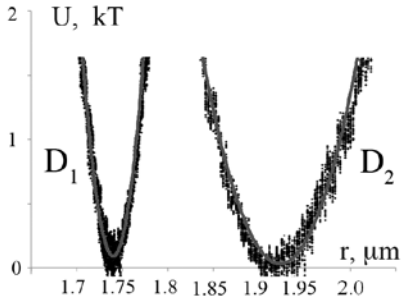

Figure 2.10. Interparticle potential for two different deviatoric curvatures (D_1 = 0.016 μm^{-1}, D_2 = 0.007 μm^{-1}) as obtained from the probability distribution of the interparticle distances.

2.3.7 Effect of the particle density on the organization

The square lattices that we observe in our experiment arise because this arrangement optimizes the attractive capillary interactions between the particles. However, when we increase the concentration of particles, the organization changes into hexagonal packing (Fig. 2.11a,b).

We characterize this transition by calculating the local bond orientation order parameter $\psi_n = \frac{1}{N}\sum_j e^{in\theta_j}$ for each particle [45]. Here N indicates the number of neighbors of the particle and θ_j is the angle between the bond with a neighboring particle j and an arbitrary reference axis. The index n denotes the symmetry of the lattice: $\langle|\psi_4|\rangle$ measures four-fold symmetry and $\langle|\psi_6|\rangle$ measures six-fold symmetry. Figure 2.11b shows both $\langle|\psi_4|\rangle$ and $\langle|\psi_6|\rangle$ as a function of the particle density at the interface for interfaces with $D \approx 0.01$ μm^{-1}. At low densities $\langle|\psi_4|\rangle > \langle|\psi_6|\rangle$, which indicates that the particles organize into a square lattice. However, at a density of approximately 0.3 μm^{-2}, $\langle|\psi_4|\rangle$ drops rapidly, while $\langle|\psi_6|\rangle$ increases, indicating a transition from a square to hexagonal packing. Sometimes, coexistence between square and hexagonal domains is seen on the same droplet.

The reason for the change in particle organization with increasing particle density is that the short-range repulsion is still isotropic and will eventually dominate because a higher packing density can be achieved for particles in a hexagonal lattice than for particles in a square lattice. The gain in adsorption energy outweighs the cost of the unfavorable capillary interactions. The smallest separation distance between particles in a square lattice is approximately 1.73 μm, which corresponds to a maximum particle density of approximately 0.33 μm^{-2} for the square lattice. Above this density, regions of hexagonal organizations begin to appear. The maximum particle density for particles in a hexagonal lattice at the same particle separation in 1.73 μm corresponds to 0.39 μm^{-2}. Both densities are indicated with the vertical dashed lines in Fig. 2.11c.

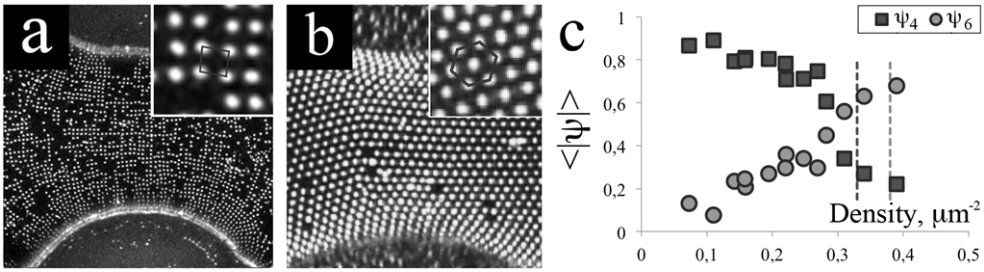

Figure 2.11. Transition from square to hexagonal packing at high particle densities. **(a)** Part of a dumbbell-shaped droplet covered with colloidal particles at relatively low density (0.16 μm^{-2}) organize in a square pattern: $\langle|\psi_4|\rangle$ = 0.81, $\langle|\psi_6|\rangle$ = 0.2; **(b)** At higher density (0.64 μm^{-2}) the particles are organized in a hexagonal lattice (see inset): $\langle|\psi_4|\rangle$ = 0.32, $\langle|\psi_6|\rangle$ = 0.74. **(c)** Bond order parameters for four- and six-fold symmetry as a function of particle density for interfaces with D = 0.01 μm^{-1}. The vertical dashed lines indicate maximum densities for a particle separation of 1.73 μm in a square (0.33 μm^{-2}) and a hexagonal lattice (0.39 μm^{-2}).

2.4 Concluding remarks

In this study we have demonstrated that spherical microparticles stabilized with negative charge and trapped at an oil-water interface show attraction if the interface is anisotropically curved. This curvature-induced capillary interaction has a four-fold symmetry and leads to particle organization into a square pattern aligned along the principal curvature axes of the interface.

The results strongly suggest that the precise shape of a curved interface doesn't play an explicit role in the particle interaction; it is controlled by the deviatoric curvature only. In the next chapter we present theoretical calculations that support these findings.

Our results show that a precise control over the curvature of the interface opens up new possibilities to direct the self-assembly of particles into complex arrangements.

A similar curvature-induced interaction might also arise for particles embedded in a membrane. Anisotropically curved membranes occur for example in lipid mesophases, such as the cubic phase. Such phases have attracted attention, because they facilitate the crystallization of some membrane proteins [46]. The mechanism underlying this crystallization method is poorly understood, but our data suggest that anisotropic interactions between proteins induced by the curvature field might play a role.

References

1. Wang, Y.F., et al., *Colloids with valence and specific directional bonding.* Nature, 2012. **491**(7422): p. 51-U61.
2. Chen, Q., S.C. Bae, and S. Granick, *Directed self-assembly of a colloidal kagome lattice.* Nature, 2011. **469**(7330): p. 381-384.
3. Glotzer, S.C. and M.J. Solomon, *Anisotropy of building blocks and their assembly into complex structures.* Nature Materials, 2007. **6**(8): p. 557-562.
4. Bianchi, E., C.N. Likos, and G. Kahl, *Self-Assembly of Heterogeneously Charged Particles under Confinement.* Acs Nano, 2013. **7**(5): p. 4657-4667.
5. Glotzer, S.C., M.J. Solomon, and N.A. Kotov, *Self-assembly: From nanoscale to microscale colloids.* Aiche Journal, 2004. **50**(12): p. 2978-2985.
6. Chen, C.H., et al., *Microfluidic Assembly of Magnetic Hydrogel Particles with Uniformly Anisotropic Structure.* Advanced Materials, 2009. **21**(31): p. 3201-+.
7. Millman, J.R., et al., *Anisotropic particle synthesis in dielectrophoretically controlled microdroplet reactors.* Nature Materials, 2005. **4**(1): p. 98-102.
8. Choi, C.H., et al., *Surface-Tension-Induced Synthesis of Complex Particles Using Confined Polymeric Fluids.* Angewandte Chemie-International Edition, 2010. **49**(42): p. 7748-7752.
9. Sacanna, S. and D.J. Pine, *Shape-anisotropic colloids: Building blocks for complex assemblies.* Current Opinion in Colloid & Interface Science, 2011. **16**(2): p. 96-105.
10. Dugyala, V.R., S.V. Daware, and M.G. Basavaraj, *Shape anisotropic colloids: synthesis, packing behavior, evaporation driven assembly, and their application in emulsion stabilization.* Soft Matter, 2013. **9**(29): p. 6711-6725.
11. Dijkstra, M., *Phase diagrams of shape-anisotropic colloidal particles*, in *Physics of Complex Colloids*, F.S. C. Bechinger, P. Ziherl, Editor. 2013.
12. Winkleman, A., et al., *Directed self-assembly of spherical particles on patterned electrodes by an applied electric field.* Advanced Materials, 2005. **17**(12): p. 1507-1511.
13. Lloyd, J.R., M.O. Hayesmichel, and C.J. Radcliffe, *Internal organizational measurement for control of magnetorheological fluid properties.* Journal of Fluids Engineering-Transactions of the Asme, 2007. **129**(4): p. 423-42814. Poulin, P., et al., *Novel colloidal interactions in anisotropic fluids.* Science, 1997. **275**(5307): p. 1770-1773.
15. Subramaniam, A.B., M. Abkarian, and H.A. Stone, *Controlled assembly of jammed colloidal shells on fluid droplets.* Nature Materials, 2005. **4**(7): p. 553-556.
16. Kumar, A., et al., *Amphiphilic Janus particles at fluid interfaces.* Soft Matter, 2013. **9**(29): p. 6604-6617.
17. Rezvantalab, H. and S. Shojaei-Zadeh, *Capillary interactions between spherical Janus particles at liquid-fluid interfaces.* Soft Matter, 2013. **9**(13): p. 3640-3650.
18. Dommersnes, P., et al., *Active structuring of colloidal armour on liquid drops.* Nature Communications, 2013. **4**.

19. Dillmann, P., G. Maret, and P. Keim, *Polycrystalline solidification in a quenched 2D colloidal system.* Journal of Physics-Condensed Matter, 2008. **20**(40).
20. Velev, O.D. and K.H. Bhatt, *On-chip micromanipulation and assembly of colloidal particles by electric fields.* Soft Matter, 2006. **2**(9): p. 738-750.
21. Kralchevsky, P.A. and K. Nagayama, *Capillary interactions between particles bound to interfaces, liquid films and biomembranes.* Advances in Colloid and Interface Science, 2000. **85**(2-3): p. 145-192.
22. Lewandowski, E.P., et al., *Orientation and Self-Assembly of Cylindrical Particles by Anisotropic Capillary Interactions.* Langmuir, 2010. **26**(19): p. 15142-15154.
23. Loudet, J.C., et al., *Capillary Interactions Between Anisotropic Colloidal Particles.* Physical Review Letters, 2005. **94**(1): p. 018301.
24. Yao, L., et al., *Near field capillary repulsion.* Soft Matter, 2013. **9**(3): p. 779-786.
25. Wurger, A., *Curvature-induced capillary interaction of spherical particles at a liquid interface.* Physical Review E, 2006. **74**(4).
26. Zeng, C., et al., *Capillary interactions among spherical particles at curved liquid interfaces.* Soft Matter, 2012. **8**(33): p. 8582-8594.
27. Shindel, M.M., S.W. Wang, and A. Mohraz, *Interfacial polymer phase segregation and self-assembly of square colloidal crystals.* Soft Matter, 2012. **8**(25): p. 6684-6688.
28. Furst, E.M., *Directing colloidal assembly at fluid interfaces.* Proceedings of the National Academy of Sciences of the United States of America, 2011. **108**(52): p. 20853-20854.
29. Pieranski, P., *Two-Dimensional Interfacial Colloidal Crystals.* Physical Review Letters, 1980. **45**(7): p. 569-572.
30. Peter A. Kralchevsky, K.D.D., *Interactions between Particles at a Fluid Interface.* Nanoscience: Colloidal and Interfacial Aspects, 2010: p. pp. 397-435.
31. Vella, D. and L. Mahadevan, *The "Cheerios effect".* American Journal of Physics, 2005. **73**(9): p. 817-825.
32. Bowden, N., et al., *Self-assembly of mesoscale objects into ordered two-dimensional arrays.* Science, 1997. **276**(5310): p. 233-235.
33. Botto, L., et al., *Capillary interactions between anisotropic particles.* Soft Matter, 2012. **8**(39): p. 9957-9971.
34. Madivala, B., J. Fransaer, and J. Vermant, *Self-Assembly and Rheology of Ellipsoidal Particles at Interfaces.* Langmuir, 2009. **25**(5): p. 2718-2728.
35. Cavallaro, M., et al., *Curvature-driven capillary migration and assembly of rod-like particles.* Proceedings of the National Academy of Sciences of the United States of America, 2011. **108**(52): p. 20923-20928.
36. Stamou, D., C. Duschl, and D. Johannsmann, *Long-range attraction between colloidal spheres at the air-water interface: The consequence of an irregular meniscus.* Physical Review E, 2000. **62**(4): p. 5263-5272.
37. Perro, A., et al., *Design and Synthesis of Model Transparent Aqueous Colloids with Optimal Scattering Properties.* Langmuir, 2009. **25**(19): p. 11295-11298.

38. Pelletier, V., et al., *Microrheology of Microtubule Solutions and Actin-Microtubule Composite Networks.* Physical Review Letters, 2009. **102**(18).
39. Kilfoil, M., *Biological Physics Lab Webpage: http://people.umass.edu/kilfoil/downloads.html.*
40. D'Errico, J., *Routines are available online: http://www.mathworks.com/matlabcentral/fileexchange/8998-surface-fitting-using-gridfit.*
41. Safran, S.A., *Statistical Thermodynamics of Surfaces, Interfaces, and Membranes*. 2003: Westview Press.
42. Nikolaides, M.G., et al., *Electric-field-induced capillary attraction between like-charged particles at liquid interfaces.* Nature, 2002. **420**(6913): p. 299-301.
43. Megens, M. and J. Aizenberg, *Like-charged particles at liquid interfaces.* Nature, 2003. **424**(6952): p. 1014-1014.
44. Nikolaides, M.G., et al., *Like-charged particles at liquid interfaces - Reply.* Nature, 2003. **424**(6952): p. 1014-1014.
45. Steinhardt, P.J., D.R. Nelson, and M. Ronchetti, *Bond-orientational order in liquids and glasses.* Physical Review B, 1983. **28**(2): p. 784-805.
46. Caffrey, M., *Crystallizing Membrane Proteins for Structure Determination: Use of Lipidic Mesophases.* Annual Review of Biophysics, 2009. **38**: p. 29-51.

CHAPTER 3

NEAR-FIELD CAPILLARY INTERACTIONS BETWEEN SPHERICAL PARTICLES ON CURVED LIQUID INTERFACES

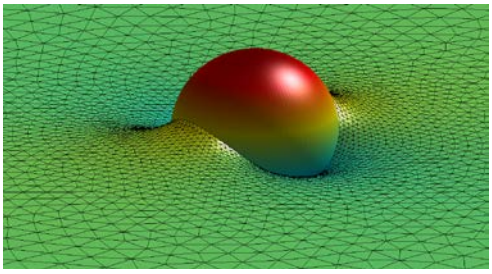

In the previous chapter, we have seen that spherical particles can organize into an unusual square lattice. This implies that the inter-particle interactions must be anisotropic. Here we present numerical calculations to show how such anisotropic interactions arise. A spherical particle trapped at an interface that locally has anisotropic curvature cannot keep the contact angle constant along the contact line without deforming the interface. To find this deformation we solve the Young-Laplace equation in the vicinity of a particle using the finite elements method (FEM). We find that the interfacial deformation around the particle has a quadrupolar shape. When two particles approach each other, so that the deformations that they induce overlap, a capillary interaction arises, which also has quadrupolar symmetry. We calculate the magnitude of this interaction for different interface shapes and particle sizes and use this to explain our experimental findings of the previous chapter. We also compare our results to previously published analytical approximations that are valid for large particle separations. We find that the interaction is strongly enhanced in the near field (for small separations) compared to the analytical prediction.

3.1 Introduction

The behavior of colloidal particles trapped at liquid interfaces and their interactions have been addressed in many theoretical and experimental works. Forces of different nature can contribute to the effective particle interaction potential [1, 2]. These include electrostatic interactions, Van der Waals forces, and capillary forces [3]. The latter occur if the interface around an adsorbed particle is deformed leading to an increase in interfacial area [4]. When two such particles approach each other, this excess area changes, leading to an effective interaction.

One way in which the presence of a particle can cause a deformation of the interface is by an external force on the particle, such as gravity or buoyancy [5, 6], or an electric field [7, 8]. Deformations may also be caused by irregularities in the contact line [9, 10], or by anisotropy in shape [11, 12] or in surface chemistry [13, 14] of the particles. The complex interplay between capillary forces and other forces (for example electrostatic) results in different interaction potentials, which determine whether the particles disperse or attract each other [6, 15] or even form crystals of different structures [8, 16-18].

Several studies in the last decade have revealed that the interaction between particles and their organization depend not only on external forces and on the particles' intrinsic properties. The shape of the hosting interface, or more precisely its curvature, also has a significant effect on the interaction, and it was shown that even small, spherical colloids with a smooth and homogeneous surface could attract each other on an interface with anisotropic curvature [19-21].

The first theoretical prediction of this curvature-induced interaction was due to Wurger [19], who considered particles at an interface with negative Gaussian curvature (catenoid). It was reasoned that a particle is bound to deform the interface in order to satisfy the condition of constant contact angle along the contact line. By constructing a free energy functional that describes the dependency of the surface area on the deformation field, he could find the deformation field ξ of the interface around a particle:

$$\xi(r,\varphi) = \frac{ca_0^4}{6r^2} cos(2\varphi) \qquad 3.1$$

where polar coordinates have been used, with the particle center in the origin, r the distance from the particle center, and φ the angle between $\vec{r}$ and one of the principal curvatures of the interface. In Equation 3.1, $a_0 = a\ sin\theta$ is the projection of the particle radius a on a flat interface, with θ the contact angle and c the curvature of the interface (for a catenoid the two principal curvatures are $k_1 = c$ and $k_1 = -c$).

The deformation field induced between two particles was calculated for inter-particle distances ρ with $a \ll \rho \ll 1/c$:

$$\xi(r) = \frac{ca_0^2}{6} \frac{1}{1-(a_0/\rho)^4} \left[\frac{a_0^2}{r^2} + \frac{3a_0^2 r^2}{\rho^4}\right] \qquad 3.2$$

where r is the distance from the origin, which is placed at the center of one of the particles. The interaction energy between these particles was calculated from the reduction in surface free energy due to area reduction after overlap of the deformation fields:

$$U(\rho, \varphi_0) = -\frac{\pi}{12}\gamma\frac{c^2 a_0^8}{\rho^4}cos(4\varphi_0) \quad 3.3$$

where γ is the interfacial tension and φ_0 is the angle between the line connecting the particle centers and the principal axis of the interface. The cosine term in Equation 3.3 indicates quadrupolar symmetry of the potential. This is what causes the organization of particles in a square lattice, as observed and discussed in Chapter 2.

However, the typical distances between particles, as observed in our experiments, are very small, so that the far-field approximation (Equation 3.2) is not likely to give an accurate estimate of the potential. It is for this reason that in this chapter, we estimate the strength of the interactions in the near field, for $a < \rho < 10a$. We consider anisotropically curved liquid interfaces with zero mean curvature (catenoid) and with finite mean curvature (cylinder).

We do this by numerically solving the Young-Laplace equation for the shape of the interface, which minimizes the interfacial area for given boundary conditions. We find the deformation field ξ in the vicinity (near-field) of the particles. Induced by such deformations capillary forces acting on the particles were calculated; the interaction potential was then calculated by integrating these forces. We find that the attractive interaction between particles increases more steeply in magnitude upon decreasing the particle separation than predicted by Equation 3.3.

3.2 Theory

3.2.1 Representation of the interface. Young-Laplace equation.

The interface is parameterized by a position vector $\vec{r} = (x, y, z(x, y))$, where it is assumed that the height $z(x, y)$ is single-valued (see Figure 3.1). In this parameterization, the unit normal vector to the interface at position (x, y) is

$$\vec{n}_I = \frac{\hat{k} - \nabla z}{\sqrt{g}} = \frac{(-z_x, -z_y, 1)}{\sqrt{g}} \quad 3.4$$

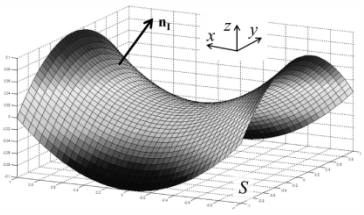

Figure 3.1: Curved interface $(x, y, z(x, y))$. The unit normal vector to the surface $\vec{n}_I$ is indicated; S denotes the reference domain in the xy plane.

where $\nabla = (\partial_x, \partial_y)$ is the 2-dimensional nabla operator, and where g is the metric of the surface: $g = 1 + (\nabla z)^2 = 1 + z_x^2 + z_y^2$, with z_x and z_y the partial derivative of z with respect to x and y, respectively.

The free energy functional of the interface is given by

$$F = \gamma \iint dA - p \iiint dV = \gamma \iint_S \sqrt{g} dS - p \iiint_S z dS \qquad 3.5$$

where the first contribution is due to the interfacial tension and the second due to the pressure. For a droplet with a given volume and a pinned contact line, the pressure arises as a Lagrange multiplier associated with the volume constraint. In the last form of Equation 3.5, the integral is over the projection on the reference domain in the xy plane; the surface element is given by $dA = \sqrt{g} dS = \sqrt{g} dx dy$.

The shape of the interface follows from minimization of the free energy functional, leading to the following Euler-Lagrange equation:

$$\gamma \nabla \left(\frac{\nabla z}{\sqrt{g}} \right) + p = 0 \qquad 3.6$$

which is the generalized Young-Laplace equation. This can also be written as

$$\nabla \cdot \vec{n}_I = \frac{p}{\gamma} \qquad 3.7$$

The left-hand side is the curvature of the surface and the right-hand side is the Laplace pressure divided by the interfacial tension. For a surface with zero mean curvature (a flat surface or a catenoid) $p = 0$, for a spherical drop $p = 2\gamma/R$, and for a cylindrical surface $p = \gamma/R$. In the general case, it can be shown, using the properties of the nabla operator that the total curvature equals:

$$k = \frac{p}{\gamma} = \frac{z_{xx}(1+z_y^2) + z_{yy}(1+z_x^2) - 2 z_x z_y z_{xy}}{g^{3/2}} \qquad 3.8$$

3.2.2 Colloidal particle on a curved interface

When a particle adsorbs at the interface, the shape of the interface may change slightly in the vicinity of the particle: the local height changes from z_0 to z (Figure 3.2).

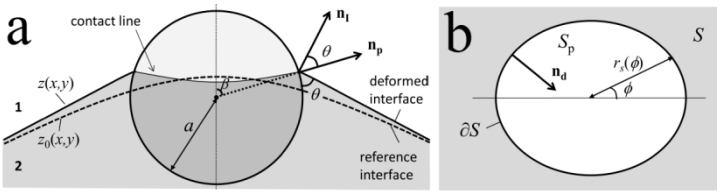

Figure 3.2: Colloidal particle adsorbed onto curved interface. (**a**) Side view; (**b**) projection on the reference domain S.

The contact line must then also adjust its x and y position such that:

$$(x - x_p)^2 + (y - y_p)^2 + (z - z_p)^2 = a^2 \tag{3.9}$$

with (x_p, y_p, z_p) the coordinates of the center of the colloid and a the radius of the colloid. Using polar coordinates in the reference domain, with the origin at (x_p, y_p), we can also write this as

$$r_S(\varphi) = \sqrt{a^2 - (z_S(\varphi) - z_p)^2} \tag{3.10}$$

where the subscript s denotes that the point is on the boundary dS.

A finite element description of the problem is obtained from the weak formulation of the Young-Laplace equation:

$$\iint_S \; w(x,y)\left(\nabla \cdot \vec{n}_I - \frac{p}{\gamma}\right) dS = 0 \tag{3.11}$$

where w is an arbitrary function, that can be considered as a virtual vertical displacement of the interface. After integration by parts (Green-Gauss theorem), this becomes:

$$-\iint_S \; \nabla w \cdot \vec{n}_I dS + \int_{\partial S} w \vec{n}_I \cdot \vec{n}_S dS - \int_S \; w \frac{p}{\gamma} dS = 0 \tag{3.12}$$

where $\vec{n}_S$ is the outward unit vector on the domain boundary. The boundary condition on the particle surface is given by the fixed contact angle:

$$\vec{n}_I \cdot \vec{n}_P = cos\theta \tag{3.13}$$

with $\vec{n}_P$ the outward unit normal to the particle surface at the contact line.

The outward unit vector $\vec{n}_S$ is a vector normal to the contact line and lies in the xy plane. It can be written in terms of $\vec{n}_I$ and $\vec{n}_P$

$$\vec{n}_S = A \cdot \hat{k} \times (\vec{n}_I \times \vec{n}_P) \tag{3.14}$$

where $(\vec{n}_I \times \vec{n}_P)$ is the tangent vector at the contact line and $\hat{k}$ is the unit vector in the z-direction. The factor A is a normalization constant that makes sure that the norm of $\vec{n}_S$ is unity. Using the BAC-CAB rule for the triple cross product, we find:

$$\vec{n}_S = \frac{\vec{n}_I cos\beta - \frac{1}{\sqrt{g}}\vec{n}_P}{\sqrt{cos^2\beta - \frac{2}{\sqrt{g}}cos\theta cos\beta + \frac{1}{g}}} \tag{3.15}$$

with $\vec{n}_P \cdot \hat{k} = cos\beta = (z_S - z_P)/a$ and $\vec{n}_P \cdot \hat{k} = 1/\sqrt{g}$. It follows that the term $\vec{n}_I \cdot \vec{n}_S$ that appears in the boundary integral can be written as

$$\vec{n}_I \cdot \vec{n}_S = \frac{cos\beta - \frac{1}{\sqrt{g}}cos\theta}{\sqrt{cos^2\beta - \frac{2}{\sqrt{g}}cos\theta cos\beta + \frac{1}{g}}} \tag{3.16}$$

A particle adsorbed to the interface assumes an equilibrium position at which the net force on the particle vanishes. The force on a particle i has three contributions

$$\vec{f}_i = \vec{f}_{is} + \vec{f}_{ip} + \vec{f}_{i,ext} \tag{3.17}$$

The first contribution is due to the meniscus, the second due to the pressure difference, and the third is the external force exerted on the particle. The first term is found by integrating the surface tension along the contact line:

$$\vec{f}_{is} = \gamma \int_{\partial C_i} \vec{m} dl \tag{3.18}$$

where ∂C_i is the contact line along particle i and $\vec{m}$ the unit vector tangential to the meniscus and normal to the contact line:

$$\vec{m} = A_m(\vec{n}_I \times \vec{n}_P) \times \vec{n}_I = \frac{\vec{n}_P - \vec{n}_I cos\theta}{sin\theta} \tag{3.19}$$

where the BAC-CAB rule has been used to obtain the second form. Note that to transform this to an integral in the reference plane we need to transform the line element dl towards a line element ds in the reference xy plane (see Appendix):

$$dl = \frac{sin\theta ds}{\sqrt{cos^2\beta - \frac{2}{\sqrt{g}}cos\theta cos\beta + \frac{1}{g}}} \tag{3.20}$$

Note that the z-component of this contribution to the force is

$$\hat{k} \cdot \vec{f}_{is} = \gamma \int_{\partial S_i} \vec{n}_I \cdot \vec{n}_S ds \tag{3.21}$$

The second contribution to the force, due to the pressure difference is obtained by integrating the pressure over the area of the colloid:

$$\vec{f}_{ip} = \iint_{A_c} \vec{n}_P \, P dA \tag{3.22}$$

where A_c denotes the area of the spherical particle and P is the local pressure, which is different in liquids 1 and 2 if there is a finite mean curvature; we write $P_2 = P_1 + p$. Then,

$$\vec{f}_{ip} = p \iint_{A_2} \vec{n}_P dA = pa^2 \int_0^{2\pi} \int_{\pi}^{\beta} \vec{n}_P sin\theta d\theta d\varphi =$$
$$= pa^2 \int_0^{2\pi} \begin{pmatrix} \frac{1}{2}(\beta - \pi - sin\beta cos\beta) cos\varphi \\ \frac{1}{2}(\beta - \pi - sin\beta cos\beta) sin\varphi \\ \frac{1}{2} sin^2\beta \end{pmatrix} d\varphi \tag{3.23}$$

with p the Laplace pressure and A_2 the area between the colloid and liquid 2. To evaluate the integral, polar coordinates were used in the reference plane. The integral over φ can be converted into a line integral using

$$\mathrm{d}\varphi = \frac{\frac{1}{\sqrt{\mathrm{g}}} - \cos\theta\cos\beta}{\mathrm{a}\sin^2\beta \sqrt{\cos^2\beta - \frac{2}{\sqrt{\mathrm{g}}}\cos\theta\cos\beta + \frac{1}{\mathrm{g}}}} ds = -\frac{\vec{\mathrm{n}}_\mathrm{P} \cdot \vec{\mathrm{n}}_\mathrm{S}}{a sin^2\beta} ds \tag{3.24}$$

In our calculations, we take the x and y position of the particles fixed (so that there may be a net force tangential to the surface), while we assume that the height of the particle adjusts so as to make the normal component of the force vanish. This condition can be imposed by the method of Lagrange multipliers, by adding a term $\lambda_i(\vec{n}_i \cdot \vec{f}_i)$ to Equation 3.12, with λ_i a Lagrange multiplier, and $\vec{n}_i$ the unit normal of the interface at the particle center.

3.3 Finite element method

Equations 3.13 with 3.18 and the Lagrange multiplier terms yield a non-linear equation that is solved using the finite element method. The integration domain is discretized using a

triangular mesh, generated using a method published previously [22]. Both the local height z of the interface and the virtual displacement w are discretized using linear interpolation functions in each triangular element. This gives a set of non-linear equations for the z-position of the interface at each node of the mesh. These equations are solved using the Newton-Raphson method [23], using a home-made Matlab script. This gives the shape of the interface in the presence of the particles, from which the force on the particle can be calculated using Equations 3.17-18, and 3.23.

3.4 Results and discussion

3.4.1 Interface deformation

First, a single particle (a_0 = 1 μm) was placed on catenoids with different curvatures c and the deformation field ξ around a particle was calculated. Note that the deviatoric curvature $D = |k_1 - k_2|/2$ of a catenoid is $D = |c|$ at the location where the particle was deposited (Figure 3.3a); therefore the parameter c can locally be treated as D.

The calculated deformation field $\xi = z - z_0$ has a quadrupolar shape, as shown in Fig. 3.3b, and coincides with Wurger's prediction $\xi(\varphi) \propto \cos(2\varphi)$ as in Equation 3.1.

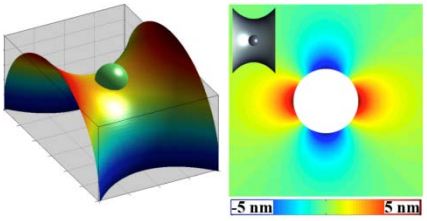

(a) (b)

Figure 3.3: (**a**) Particle on a catenoid interface; color indicates local height. (**b**) Quadrupolar deformation field of the catenoid interface induced by a spherical particle. The rising deformation field is in horizontal direction.

The radial profiles (at φ = 0) of ξ are plotted in Fig. 3.4a,b and compared to the analytical result, calculated with Equation 3.1. It is clear that the deformation of the interface around a single particle is proportional to r^2 and is very accurately described by Equation 3.1. Only at large distances do the numerical results deviate from the analytical result, which is most probably due to the boundary conditions that force the deformation to zero at the boundary of the mesh.

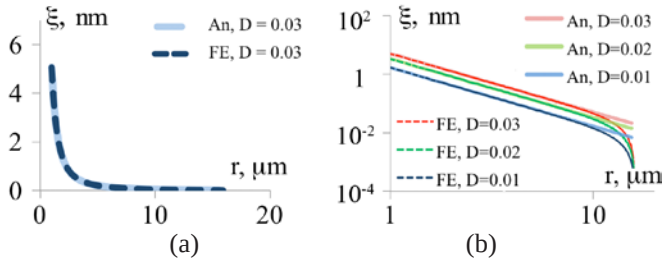

Figure 3.4: Deformation field ξ in linear scale (**a**) and logarithmic scale (**b**). D: deviatoric curvature, FE: deformation field calculated with finite elements method, An: calculated by the analytical Equation 3.1.

3.4.2 Torque

Next, we consider an interface with two particles in it. Two particles trapped at a liquid interface experience an attractive interaction between them, if the deformation fields around them are like-signed and overlap, Fig. 3.5a [3]. For particles on an anisotropically curved interface, the deformation field has different signs in the directions of two principal curvatures, Fig. 3.5b. This means that two particles will attract each other along these directions. By contrast, overlapping of opposite-signed deformations (Fig. 3.5c) gives rise to a repulsive capillary interaction; hence, two particles situated at 45° with respect to the principal axes (Fig. 3.5d) will repel each other. Clearly, the quadrupolar deformation field strongly favors the formation of a square lattice.

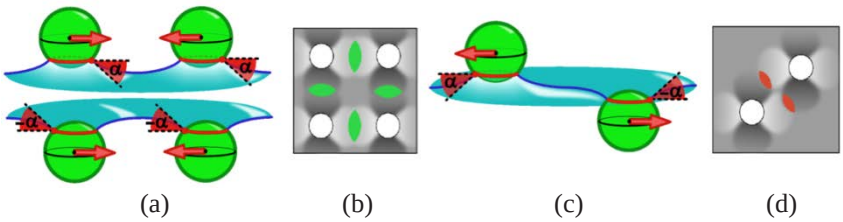

Figure 3.5: Interaction between to spherical particles at a liquid interface. Overlap of like-signed deformations leads to capillary attraction (**a**). As a consequence, particles on an interface with anisotropic curvature attract each other along the principal (**b**). When opposite-signed deformations overlap, the particles repel each other (**c**). This happens for particles situated at an angle of 45° to the principal axes (**d**). Arrows indicate attractive or repulsive forces.

These considerations suggest that there is a force $\vec{f}$ acting between the particles separated by the distance $\vec{\rho}$, which rotates them to certain orientations with respect to the principal curvature axes, thus creating a torque: $\vec{T} = \vec{\rho} \times \vec{f}$. If we restrict the interaction forces to act only in the interfacial plane (the component normal to the interface is forced to be zero), this torque will act to rotate the particles in the plane of the interface.

Figure 3.6a shows the torque as a function of the orientation angle φ_0. The figure indicates that there are two stable equilibriua at which there is no net torque on the particles: at φ_0 = 0 and 90 degrees. Any deviation from these orientations causes a torque that rotates the particles back to these angles. By contrast, the situation at φ_0 = 45 corresponds to an unstable equilibrium. There is no net torque at this angle, but any small fluctuation leads to a torque, which pushes the particles towards one of the stable states. The strongest torque occurs at φ_0 = 22.5 and φ_0 = 67.5 degrees.

These results imply that the system consisting of two particles will always rotate to align the bond between them parallel to one of the two local principal curvature directions. A square lattice, formed in this way, will have its cells always aligned with the local principal curvatures, as described in Chapter 2.

The effect of the magnitude of the deviatoric curvature on the torque at a fixed orientation angle (φ_0 = 22.5, when the strongest torque occurs) is shown in Figure 3.6b. The strength of the torque grows as D^2. As expected, higher curvatures lead to a stronger torque, thus making deviations from φ_0 = 0 or 90 degrees less possible. This in turn leads to a higher degree of ordering in a square lattice.

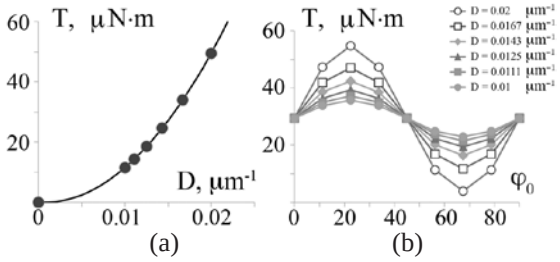

Figure 3.6: (**a**) Dependency of the torque T on the deviatoric curvature at the orientation angle φ_0 = 22.5 degrees; the solid line is fit D^2. **(b)** Effect of the deviatoric curvature on dependency of the torque T on the orientation angle φ_0.

3.4.3 Pair interaction potential

In order to quantitatively characterize the particle interaction we take two particles with a radius a_0 = 1 μm and place them on a catenoid-shaped interface ($D = |c|$) at a distance $-\rho/2$ and $\rho/2$ from the origin. Then we calculate the interaction potential for two orientations: φ_0 = 0 and φ_0 = 45 degrees. We do this by calculating the force $\vec{f}$ acting between the particles at varying distances and then integrating the force: $U(\rho) = \int_{\infty}^{\rho} \vec{f} \cdot d\vec{r}$. The effect of the distance ρ, the deviatoric curvature $D = |c|$, and the particle size a_0 were studied; the results are shown in Fig. 3.7a.

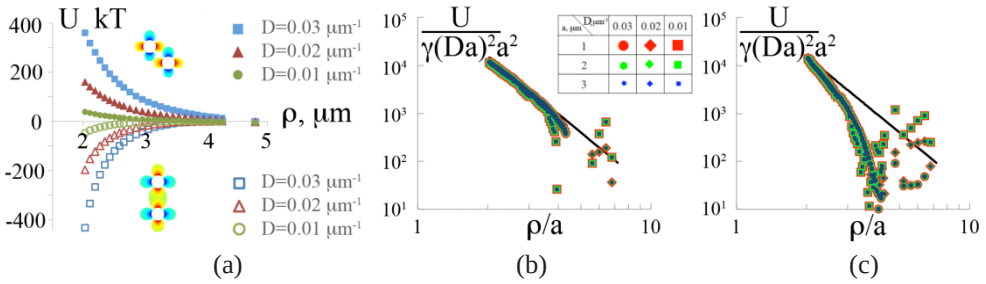

Figure 3.7: (**a**) Pair interaction potentials at different curvatures and orientation angles. Normalized repulsive (**b**) and attractive (**c**) interaction; black line is the analytical interaction potential.

Even though the deformation of the interface caused by the particles is at most a few nanometers, the interaction between the particles can still be many kT, because of the relatively large interfacial tension (chosen to be 34 mN/m as for the experimental system in Chapter 2, which is about 8 kT/nm^2). As expected, the strength of the interaction increases with increasing the deviatoric curvature of the interface.

We find that the calculated interaction curves for different D and a_0 can be superimposed by plotting $-U/(\gamma a^2)(Da)^2$ as a function of ρ/a, as shown in Fig. 3.7b, c. The interaction potential calculated with the analytical Equation 3.3 was normalized in the same way and shown with the black line.

The analytical expression predicts a distance scaling according to $(\rho/a)^{-4}$; our numerical results are consistent with this only in the case of repulsive interaction, as shown in Fig. 3.7b. One can notice a drop in the potential for distances $\rho/a > 4$, but this is due to the boundary conditions forcing the deformation to 0 at the boundary of the mesh.

However, in the case of attractive interaction we find a potential proportional to $(\rho/a)^{-6}$, which is steeper than that of the analytical prediction. A power-law fit through the data for the attractive interaction potential in Fig. 3.7c gives

$$U_{attractive} = -6\gamma D^2 a_0^4 \left(\frac{\rho}{a_0}\right)^{-6} \qquad 3.25$$

where $a_0 = a\,sin\theta$ is the effective particle radius, with θ the contact angle.

The values for repulsive interaction obtained with FEM method are consistent with those predicted by Equation 3.3, even if the latter was derived for distances $\rho \gg a$. However, the fact that the potentials calculated with FEM for attractive and repulsive interactions behave differently (the powers $(\rho/a)^{-6}$ and $(\rho/a)^{-4}$ respectively) is surprising, and the reason for this is not understood.

3.4.4 Superposition principle

As was mentioned in the previous section, the results of our numerical calculations for the interaction potential differ from the analytical prediction of Equation 3.3, which is based on a far-field approximation $\rho \gg a$. For such large distances the total deformation can be described by a superposition approximation [19]:

$$\xi(\vec{r}, \vec{r}_1, \vec{r}_2) = \xi_1(\vec{r}, \vec{r}_1) + \xi_2(\vec{r}, \vec{r}_2)$$

where $\xi(\vec{r}, \vec{r}_1, \vec{r}_2)$ is the deformation of the interface at a position $\vec{r}$ in the presence of two particles at position $\vec{r}_1$ and $\vec{r}_2$, and where $\xi_1(\vec{r}, \vec{r}_1)$ and $\xi_2(\vec{r}, \vec{r}_2)$ are the deformations when only particle 1 or 2 is present. However, we hypothesize that this approximation may not be valid for small particle separations $a < \rho < 10a$.

To test this, we place two identical spherical particles on the catenoid interface at distances $-\rho/2$ and $\rho/2$ from the origin and calculate the deformation profile ξ' when two particles are present simultaneously. Then we place the same particles separately from each other and calculate their respective deformation profiles ξ_1 and ξ_2 and according to the superposition principle calculate their total effect on the interface: $\xi'' = \xi_1 + \xi_2$.

The deformation profiles ξ' and ξ'' were calculated for particles a_0 = 1 μm at a catenoid with a deviatoric curvature D = 0.03 μm^{-1} for two distances between the particle centers: ρ_1 = 2.24 μm and ρ_2 = 3 μm. To show the difference between the deformation profiles we plot their radial cross-section at φ_0 = 0 (shown as the solid line in Fig. 3.8a); the results are shown in Fig. 3.8b; the deformation profile calculated with the analytical Equation 3.2 is also shown.

For convenient comparison of the profiles we place the left particle at r = 0 mm and plot the profiles starting from its surface (at r = 1 um); for instance, for the two upper curves the distance between the surfaces is $\rho_1 - 2a_0$ = 0.24 μm.

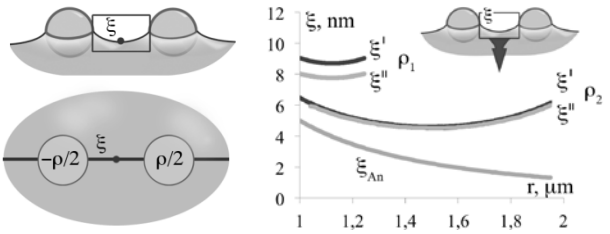

(a) (b)

Figure 3.8. (a) A diagram showing the line, along which the radial profile of the deformation field is defined; the small circle is the origin. **(b)** Radial profiles of the deformation fields ξ' (calculated for two particles present simultaneously), ξ'' (calculated with the superposition principle) and ξ_{An}. Distances between the particles' centers ρ_1 = 2.24 μm and ρ_2 = 3 μm.

From Fig. 3.8b it is clear that for distances $\rho > 3a$ the superposition principle works well, and the discrepancy between ξ' and ξ'' doesn't exceed 2%; for shorter distances this discrepancy increases reaching 10% at ρ_1 = 2.24 μm. The interface between the particles rises higher than predicted by the superposition approximation.

3.5 Comparison to experimental data

3.5.1 Critical deviatoric curvature required for organization.

In Chapter 2 we studied the effect of the curvature on particle organization. In order to quantify the phenomenon of particle alignment along the principal directions, we introduced the angle φ between an inter-particle bond and the local principle directions; we chose $\langle \cos(4\varphi) \rangle$ as the order parameter, which is 1 for ideal alignment. The experimental findings of Chapter 2 on the dependency of $\langle cos(4\varphi) \rangle$ on the deviatoric curvature D (Figure 3.9a) show that $\langle cos(4\varphi) \rangle$ reaches a plateau at D_{crit} ~ 0.003 μm^{-1}.

We now calculate with FEM the value of D at which $U_{attractive}$ becomes ~1 kT. For that we use Equation 3.25 with the following inputs: a_0 = 0.75 μm, ρ = 1.8 μm, γ = 34 mN/m. The oil-water interfacial tension was obtained experimentally and the separation 1.8 μm was chosen from the position correlation function. The resulting D_{crit} = 0.004 μm^{-1}, which is quite close to the value where the experimentally observed ordering sets in, Fig. 3.9a.

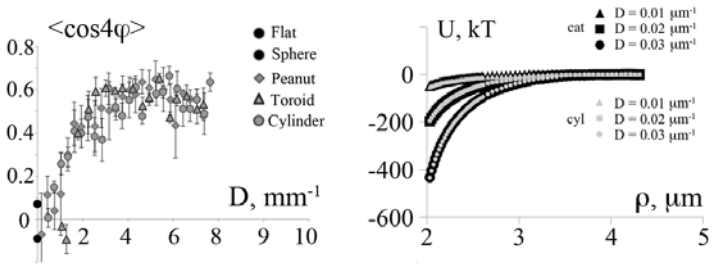

(a) (b)

Figure 3.9. (**a**) Effect of the deviatoric curvature *D* on the order parameter $\langle cos(4\varphi) \rangle$ for different shapes of the interfaces. (**b**): Attractive potential calculated for a catenoid and cylinder with equal *D*.

3.5.2 Shape independency

The findings of Chapter 2 (Figure 3.9a) also suggest that the interaction between the particles is independent of the exact shape of the interface. To check whether this is also found in our calculations, we compare the calculated deformation profile and attraction

energy for two particles a_0 = 1 μm on a catenoid and a cylinder. The particles were placed on these interfaces in places where the values of D coincide.

The calculated deformation field ξ_{cat} and ξ_{cyl} are close to each other in this case, and the areas of the deformations are therefore similar as well. This results in equal magnitude of interaction energy, independent of the exact shape of the interface, but depending only on the local value of D. The attractive potential that we calculate is shown in Fig. 3.9b: the curves $U_{cat}(\rho)$ and $U_{cyl}(\rho)$ overlap with a relative difference of $\varepsilon < 5\%$ within the range < 3 μm.

3.6 Concluding remarks

A spherical particle situated on a flat or isotropically curved interface (spherical) is able to keep the contact angle at the contact line constant simply by readjusting its position in the direction normal to the interface. However, when the interface locally has different principal curvatures, the particle has to deform the interface, in order to satisfy the abovementioned condition. In the cases studied in this work, the deformation field has a quadrupolar shape. This gives rise to anisotropic interactions between the particles, which attract each other in the direction of the local principal curvatures (orientation angles 0° and 90°). This leads to the formation of a square lattice [19].

Our experimental findings and calculations indicate that the interaction of particles at a curved interface is not explicitly dependent on the shape of the hosting interface but only on its local deviatoric curvature D. The attraction potentials for two particles are identical, whether they are at a catenoid or a cylinder, if the local D is the same.

We showed experimentally that there is a threshold for the deviatoric curvature at which the square lattices start to form. For particles with the radius a_0 = 0.75 μm at an oil-water interface with γ = 34 mN/m, D_{crit} ~ 0.003 μm^{-1}. Results of our numerical calculations showed that this is close to the value of D, where the attraction exceeds the thermal energy: D_{crit} = 0.004 μm^{-1} (calculated for particles with a radius a_0 = 1 μm).

The effect of D on the stability of square lattices can be explained with the torque, acting on a system of two particles. If deformation fields with different signs overlap (Figure 3.5c, d), repulsive capillary interactions effectively give rise to a rotational force. Thus, the system is rotated around its center and the particles are brought to the most energetically favorable positions: at 0 and 90 degrees. The strength of the torque grows as D^2.

Interestingly, the interaction potentials that we find are different for attraction and repulsion: $U^{FEM}_{attractive} \propto \gamma c^2 \frac{a^{10}}{r^6}$ and $U^{FEM}_{repulsive} \propto \gamma c^2 \frac{a^8}{r^4}$, and only the repulsive potential coincides well with the analytical prediction, which is using the superposition principle, Equation 3.2.

Appendix

The unit tangent vector along the contact line is

$$\vec{t} = \frac{\vec{n}_I \times \vec{n}_P}{sin\theta}$$

The unit tangent along the domain in the xy plane is

$$\vec{t}_{||} = \vec{n}_S \times \hat{k} = \frac{cos\beta\left(\vec{n}_I \times \hat{k}\right) - \frac{1}{\sqrt{g}}\left(\vec{n}_P \times \hat{k}\right)}{\sqrt{cos^2\beta - \frac{2}{\sqrt{g}}cos\theta cos\beta + \frac{1}{g}}}$$

We can obtain Equation 3.20 from the cosine of the angle between $\vec{t}$ and $\vec{t}_{||}$:

$$\frac{ds}{dl} = \vec{t} \cdot \vec{t}_{||} = \frac{\sqrt{cos^2\beta - \frac{2}{\sqrt{g}}cos\theta cos\beta + \frac{1}{g}}}{sin\theta}$$

where we used $\left(\vec{a} \times \vec{b}\right) \cdot \left(\vec{c} \times \vec{d}\right) = (\vec{a} \cdot \vec{c})\left(\vec{b} \cdot \vec{d}\right) - \left(\vec{a} \cdot \vec{d}\right)\left(\vec{b} \cdot \vec{c}\right)$. The relation between $d\varphi$ and ds is obtained as

$$ds = \frac{r_S d\varphi}{cos\alpha}$$

where α is the angle between $-\vec{n}_S$ and the projection of the particle normal onto the xy plane, $\vec{n}_P^{xy}$

References

1. Boneva, M.P., et al., *Attraction between Particles at a Liquid Interface Due to the Interplay of Gravity- and Electric-Field-Induced Interfacial Deformations.* Langmuir, 2009. **25**(16): p. 9129-9139.
2. Danov, K.D. and P.A. Kralchevsky, *Interaction between like-charged particles at a liquid interface: Electrostatic repulsion vs. electrocapillary attraction.* Journal of Colloid and Interface Science, 2010. **345**(2): p. 505-514.
3. Peter A. Kralchevsky, K.D.D., *Interactions between Particles at a Fluid Interface*, in *Nanoscience: Colloidal and Interfacial Aspects*, V.M. Starov, Editor. 2010, CRC Press: New York. p. 397-435.

4. Hinsch, K., *Holographic study of liquid surface deformations produced by floating particles.* Journal of Colloid and Interface Science, 1983. **92**(1): p. 243-255.
5. Vassileva, N.D., et al., *Capillary forces between spherical particles floating at a liquid-liquid interface.* Langmuir, 2005. **21**(24): p. 11190-11200.
6. Vella, D. and L. Mahadevan, *The "Cheerios effect".* American Journal of Physics, 2005. **73**(9): p. 817-825.
7. Singh, P., D.D. Joseph, and N. Aubry, *Dispersion and attraction of particles floating on fluid-liquid surfaces.* Soft Matter, 2010. **6**(18): p. 4310-4325.
8. Dillmann, P., G. Maret, and P. Keim, *Polycrystalline solidification in a quenched 2D colloidal system.* Journal of Physics-Condensed Matter, 2008. **20**(40).
9. Stamou, D., C. Duschl, and D. Johannsmann, *Long-range attraction between colloidal spheres at the air-water interface: The consequence of an irregular meniscus.* Physical Review E, 2000. **62**(4): p. 5263-5272.
10. Danov, K.D. and P.A. Kralchevsky, *Capillary forces between particles at a liquid interface: General theoretical approach and interactions between capillary multipoles.* Advances in Colloid and Interface Science, 2010. **154**(1-2): p. 91-103.
11. Loudet, J.C., et al., *Capillary interactions between anisotropic colloidal particles.* Physical Review Letters, 2005. **94**(1).
12. Botto, L., et al., *Capillary interactions between anisotropic particles.* Soft Matter, 2012. **8**(39): p. 9957-9971.
13. Glaser, N., et al., *Janus particles at liquid-liquid interfaces.* Langmuir, 2006. **22**(12): p. 5227-5229.
14. Rezvantalab, H. and S. Shojaei-Zadeh, *Capillary interactions between spherical Janus particles at liquid-fluid interfaces.* Soft Matter, 2013. **9**(13): p. 3640-3650.
15. Botto, L., et al., *Capillary bond between rod-like particles and the micromechanics of particle-laden interfaces.* Soft Matter, 2012. **8**(18): p. 4971-4979.
16. Nikolaides, M.G., et al., *Electric-field-induced capillary attraction between like-charged particles at liquid interfaces.* Nature, 2002. **420**(6913): p. 299-301.
17. Choi, I.S., et al., *Mesoscopic, templated self-assembly at the fluid-fluid interface.* Langmuir, 2000. **16**(7): p. 2997-2999.
18. Lewandowski, E.P., et al., *Oriented assembly of anisotropic particles by capillary interactions.* Soft Matter, 2009. **5**(4): p. 886-890.
19. Wurger, A., *Curvature-induced capillary interaction of spherical particles at a liquid interface.* Physical Review E, 2006. **74**(4).
20. Zeng, C., et al., *Capillary interactions among spherical particles at curved liquid interfaces.* Soft Matter, 2012. **8**(33): p. 8582-8594.
21. Shindel, M.M., S.W. Wang, and A. Mohraz, *Interfacial polymer phase segregation and self-assembly of square colloidal crystals.* Soft Matter, 2012. **8**(25): p. 6684-6688.
22. Persson, P.O. and G. Strang, *A simple mesh generator in MATLAB.* Siam Review, 2004. **46**(2): p. 329-345.

23. Bhatti, A., *Fundamental Finite Element Analysis and Applications: with Mathematica and Matlab Computations*. 2005: Wiley.

CHAPTER 4

MICRORHEOLOGY OF PARTICLE MONOLAYERS AT FLAT AIR-WATER INTERFACES

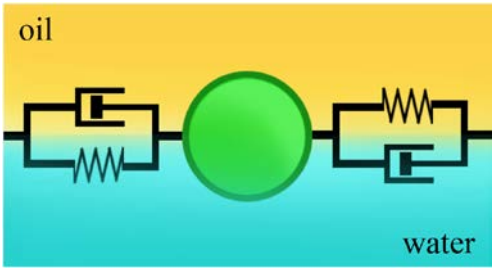

Diffusion of a particle exploring visco-elastic medium can be linked to the viscosity of the medium, as summarized in Stokes-Einstein equation. Generalization of this equation to all timescales allows one to extract rheological properties of the medium from behavior of such a particle; this approach has been given the name “microrheology”.

In this exploratory chapter we utilize the microrheology mathematical machinery adapted for quasi-2D cases to study mechanical properties of monolayers made of core-shell microparticles. We are studying how varying the surface density of the core-shell particles affects the rheology of such layers and also looking for ways of interpreting the data obtained by means of interfacial microrheology.

4.1 Introduction

4.1.1 Particles at liquid interfaces

Colloidal particles can be used to stabilize liquid interfaces, between oil and water phases in emulsions, or between air and water in foams. These occur, for example, in many products in food, cosmetic, paint, drug delivery and other industries. In all these applications, stability of the multiphase system is of crucial importance: sometimes, a high stability is desired, for example to improve shelf life, and sometimes this is not desired, for example to reduce foaming. An important factor that determines emulsion and foam stability is the rheology of the liquid interface [1, 2]. The interfacial rheological properties are determined by the density of and interactions between the stabilizing agents on the interface (surfactants, lipids, proteins, polymers, or particles [3-5].

One way to study the visco-elastic properties of an interface is interfacial rheology, traditionally performed using controlled-stress or controlled-strain macroscale mechanical rheometers [6, 7]. They allow measuring the response of an interface to a shear or dilatational stress applied at different rates or frequencies; as a result the complex shear or dilatational modulus is measured, which consists of frequency-dependent storage and loss moduli.

Traditional interfacial rheology gives reproducible results for a wide variety of systems; however, if the layer is very fragile or its area is very small, application of these methods can damage the layer even at the lowest strains. Moreover, these methods require macroscopic interfaces, which are not always possible to produce, as for example, in the case of biological membranes.

One method that is capable of probing a sample on much smaller scales is microrheology, which is based on tracking the Brownian motion of microparticles embedded in the interface. The mobility of the tracer particle is directly related to the rheological properties of its surroundings. One important feature of this method is that it can probe local micro-scale heterogeneities of the sample, which traditional macrorheology cannot.

There are two kinds of microrheology: active, that imposes a force of known amplitude and frequency to the microparticles and measures the response, and passive, which analyzes the thermally driven motion of the particles and makes use of the fluctuation-dissipation theorem. In the following sections we introduce the basic concepts of bulk and interfacial passive microrheology.

4.1.2 Bulk microrheology

The mobility of a particle placed in viscous fluid depends on the geometry of the particle and on the viscosity of the fluid. The drag force $\vec{F}$ (the friction force that the fluid

exerts on objects moving inside it) is proportional to the velocity of the particle. This relation is called Stokes law and derived from Navier-Stokes equations [8]. In the case of a spherical particle of radius a moving with a velocity $\vec{V}$ in a viscous fluid with dynamic viscosity η it reads

$$\vec{F} = -(6\pi\eta a)\vec{V} \tag{4.1}$$

The Stokes equation is exact for particles moving at low Reynolds number in a continuous non-elastic Newtonian medium with no-slip boundary conditions. The coefficient of proportionality $\zeta = 6\pi\eta a$ is called Stokes' friction coefficient.

Einstein and Smoluchowski in their works on Brownian motion independently from each other found that for a particle the friction coefficient ζ and the diffusion coefficient D are inversely proportional [9]:

$$D = \frac{k_B T}{\zeta} \tag{4.2}$$

where k_B is the Boltzmann constant and T is the temperature. Relations 4.1 and 4.2 together give the Stokes-Einstein equation, valid for a spherical particle:

$$D = \frac{k_B T}{6\pi\eta a} \tag{4.3}$$

The diffusion coefficient can be obtained easily by measuring the mean-squared displacement (MSD) of a free particle, $\langle \Delta r^2(t) \rangle = 6Dt$ in three dimensions. Hence, by analyzing the Brownian motion of a particle, the diffusion coefficient, and from that the viscosity of the medium can be obtained.

For a visco-elastic medium, Stokes' law is no longer valid, and memory must be introduced in the friction coefficient. Mason and Weitz [10] argued that a generalization of the Stokes-Einstein equation (GSE) applies in this case:

$$\tilde{G}(s) = s\tilde{\eta}(s) \approx \frac{k_B T}{\pi a s \langle \Delta \tilde{r}^2(s) \rangle} \tag{4.7}$$

where s represents the frequency in the Laplace domain, and $\tilde{G}(s)$ is the Laplace transformed shear modulus. From $\tilde{G}(s)$ it is possible to obtain the complex shear modulus, $G^*(\omega) = G'(\omega) + iG''(\omega)$ as described in [10]. Hence, this approach allows one to measure the complex shear modulus $G^*(\omega)$ by introducing spherical particles into the medium of interest, recording their MSD and using Equation 4.7. This is the basis of the microrheology method; a detailed discussion can be found in a recent review [11].

It should be noted that in order to arrive at Equation 4.7, a number of crucial approximations were made: (a) the medium around the tracer particle is treated as a continuum matrix, meaning that the size of the tracer is larger than any structural length scale in the medium; (b) no slip boundary conditions; (c) the fluid surrounding the sphere is

incompressible; (d) there are no inertial effects [10, 12, 13]. Moreover, it was assumed that the relation between $\tilde{\eta}(s)$ and $\tilde{\zeta}(s)$ known for viscous fluids is valid for all frequencies s in case of visco-elastic fluids [10].

Microrheology has been used to probe the visco-elastic properties of polymer solutions, actin networks, particles suspension and living cells [14-16]. Even though some of these studies report "excellent agreement" between complex shear moduli $G^*(\omega)$ obtained from microrheology and traditional macroscale mechanical rheology [17], others report that the $G^*(\omega)$ obtained using microrheology can be orders of magnitude too low [18, 19].

One of the explanations that have been given for this discrepancy is that the probed medium has local heterogeneities. Microrheology then probes the local particle environment, while bulk rheology probes the medium on larger length scales, at which these heterogeneities are averaged-out. These two may vary significantly, in particular when the particles are not very large compared to the typical length scales in the medium.

It is also possible that the tracer particles interact with or modify the medium in their direct vicinity and therefore report locally modified mechanical properties. For example it was shown in [20] that the surface chemistry of tracers has a strong effect on measured visco-elastic properties of F-actin networks. With all this it is clear that care should be taken when selecting tracer particles to avoid such adverse effect.

An alternative strategy, which circumvents some of the issues related to one-particle microrheology, is to analyze cross-correlations in the thermal motion of pairs of tracer particles [13, 21]. Such cross-correlations are sensitive to the medium between the particles and are therefore much less sensitive to the local particle environment. The cross-correlated particle motions are calculated as [13]:

$$D_{\alpha\beta}(R,\tau) = \langle \Delta r_\alpha^i(t,\tau)\Delta r_\beta^j(t,\tau)\delta[R - R^{ij}(t)]\rangle_{i\neq j,t} \qquad 4.8$$

where i,j are particle indices, the subscripts α,β represent different directions and R^{ij} is the distance between particles i and j. Using the motions parallel to the line joining the centers of the particles, Δr_r, we calculate the longitudinal cross-correlation D_{rr}, while from the motions perpendicular to it (Δr_θ) we can calculate $D_{\theta\theta}$. For an incompressible material, in the limit $R \gg a$ (distances larger than tracers' radius), the strain field around a moving particle decays as $1/R$, while D_{rr} and $D_{\theta\theta}$ decay as $1/R$ and $1/R^2$, respectively [13, 21]. The extension of the generalized Stokes-Einstein relation to correlated motions is

$$\widetilde{D}_{rr}(R,s) = \frac{k_B T}{2\pi R s \tilde{G}(s)}, \qquad D_{\theta\theta} = \frac{1}{2} D_{rr} \qquad 4.9$$

where $\widetilde{D}_{rr}(R,s)$ is the Laplace transform of $D_{rr}(R,\tau)$ [13]. Note that this relation does not involve a, suggesting that the properties of the probes do not play a role in the limit $R \gg a$. The microrheology that relies on cross-correlated motions and Equation 4.9 is called two-point microrheology, in contrast to the one-point method that relies on the motion of individual particles.

By extrapolating the long-wavelength thermal undulations of the medium down to the bead size, the so-called distinct mean square displacement $\langle \Delta r^2(\tau) \rangle_D$ is obtained:

$$\langle \Delta r^2(\tau) \rangle_D = \frac{2R}{a} D_{rr}(R, \tau) \tag{4.10}$$

and in case the assumptions made for GSE (Equation 4.7) are valid, $\langle \Delta r^2(\tau) \rangle_D = \langle \Delta r^2(\tau) \rangle$. When there are differences, however, $\langle \Delta r^2(\tau) \rangle$ can be understood as the superposition of a long-wavelength motion described by $\langle \Delta r^2(\tau) \rangle_D$, plus a local motion in a cavity [13].

It is clear that the length scales r that can be probed with this technique are much larger than the radius of the tracers, so that even particles smaller than the characteristic length-scale of the probed material can be used, which was indeed demonstrated in [22]. Evidently, this technique is suitable for measuring visco-elastic properties of highly inhomogeneous materials; in contrast to 1P microrheology, 2P microrheology measurements of the complex shear modulus $G^*(\omega)$ show good consistency with macroscale mechanical rheology measurements [13, 17].

Hence, bulk microrheology is a powerful tool for acquiring rheological data for "difficult" samples, where standard rheometers cannot help due to the medium matrix being very fragile, or due to small sample volumes as, for example, living cells [16, 23, 24].

4.1.3 Interfacial microrheology

While microrheology for 3D media has grown into a mature technique, its application to interfaces is still in its infancy. The experimental implementation of interfacial microrheology is similar to the 3D case: microparticles are trapped at a liquid interface (which may be covered with a complex layer) and the 2D-Brownian motion of the particles is analyzed. However, the mathematical analysis of particle mobilities is somewhat different than that in the 3D case, because the flow field created by a particle moving at an interface is much more complicated. Both the properties of the interface and those of the two adjacent fluid phases need to be taken into account. This was done first for particles on a purely viscous interface by Saffman and Delbruck [25]. They showed that the diffusion coefficient of a spherical particle at an interface is given by

$$D_s = \frac{k_B T}{4\pi\eta_s} \left[\ln\left(\frac{\eta_s}{\eta a}\right) - \gamma_E \right] \tag{4.11}$$

where a is the radius of the particle, η_s is the interfacial viscosity and $\eta = \eta_1 + \eta_2$ is the sum of the viscosities of the super- and subphase. The ratio $l = \eta_s/\eta$ is called the Saffman-Delbruck length, which characterizes the distance below which interfacial viscosity dominates. Equation 4.11 is valid only for $a \ll l$.

This equation has been used for studying mobility of lipid domains in lipid membranes or for proteins bound to a lipid membrane, but in many cases corrections are required [26-28].

Hughes and Pailthorpe introduced an extended hydrodynamic model of viscous membranes [29]. Their numerical results were later approximated in [30] by Petrov and Schwille:

$$\mathrm{D}_s = \frac{k_B T}{4\pi\eta_s}\left[\ln\left(\frac{2}{\varepsilon}\right) - \gamma_E + 4\frac{\varepsilon}{\pi} - \left(\frac{\varepsilon^2}{2}\right)\ln\left(\frac{2}{\varepsilon}\right)\right] \times \\ \times \left[1 - \left(\frac{\varepsilon^3}{\pi}\right) ln\left(\frac{2}{\varepsilon}\right) + \frac{c_1\varepsilon^{b_1}}{1+c_2\varepsilon^{b_2}}\right]^{-1} \qquad 4.12$$

where $\varepsilon = a/l$, and c_i and b_i are numerical constants (see [30] for more details). The Petrov-Schwille (P-S) approximation extends the Saffman-Delbruck model to a wider range of ε, making it usable for bigger particles [31].

Equations 4.11 and 4.12 can be used to extract surface viscosities from the motions of embedded tracer particles. However, as for bulk microrheology, this method is sensitive to local heterogeneities at the interface. In [21], therefore, viscous protein layers at the air-water interface were studied by means of both 1P and 2P microrheology. A detailed comparison of the two methods and an analysis in terms of a theoretical model for visco-elastic membranes [32] gave insight in the complex hydrodynamic flow field around particles at an interface. However, this method has only been applied to purely viscous and very homogeneous protein-covered interfaces. To make it into a widely applicable tool, a more thorough experimental validation is needed. Here, we study the potential of interfacial microrheology for characterizing particle-laden interfaces.

4.2 Experimental details

4.2.1 Materials and Methods

The monolayers of interest are comprised of spherical microgel particles deposited at a flat air-water interface. To create the latter we fill a Teflon ring with water [33]. The inner diameter of the ring is 15 mm, which is sufficiently larger than the water capillary length, $\lambda_c = \sqrt{\gamma/\rho g}$ for clean water, ~2 mm. This produces a circular region in the middle of about 10 mm in diameter, where the interface is more or less flat.

The core-shell particles forming the layer consist of a polystyrene core surrounded with a cross-linked PNIPAM-MMA shell, which is negatively charged; their synthesis is described in Chapter 2. The polystyrene core is about 300 nm in diameter and can be seen in Phase Contrast microscopy; the shell is 600 nm, giving an overall particle diameter of 1.5 μm. Unfortunately, our imaging set-up is not capable of tracking the dynamics of these particles with sufficient accuracy to analyze their mobilities. We therefore use 3 μm sized

negatively charged spherical polystyrene particles as tracer particles, which can be easily tracked.

Firstly tracer particles are suspended in ethanol at 0.01% and 10 μL of this suspension is evenly distributed over the air-water interface and equilibrated for 1 hour. As ethanol evaporates, the particles are trapped at the air/water interface. Microgel particles were also suspended in ethanol at 0.1% and 10 μL of this suspension was distributed over the air-water interface containing the tracers in the same way.

After equilibration for 30 minutes, the sample was covered with a transparent lid for minimizing airflows, and movies of tracer movements were taken with a 100x oil immersion phase contrast objective with numerical aperture 1.4 in a Zeiss Axiovert microscope.

When 20 movies for one monolayer have been taken, the density of the core-shell particles is increased by addition of 2 μL of 0.1% stock ethanol solution, while the surface density of the tracers was kept unchanged. In this way monolayers with various surface densities of core-shell particles were studied.

4.2.2 Particle tracking

Time-lapse image sequences were analyzed with a Matlab routine from [34], which allows for finding the tracers' centroids and tracking them throughout the movie. It should be noted that for dilute layers it was not possible to avoid drift in the monolayer. We therefore had to correct for the interfacial flows by stabilizing the image around one chosen tracer in video-stabilizing software. This restricts our analysis to times not longer than 2 minutes, after which the tracers leave the field of view. The tracking resolution of our microscope was analyzed by tracing particles immobilized on the glass cover, and was estimated to be 30 nm, which means that the lower limit of mean square displacements that we can detect is approximately 10^{-3} μm^2.

4.3 Results

4.3.1 Surface density of the core-shell particles and the tracers

Phase contrast images of the liquid interfaces allow for visual calculation of the surface density (Fig. 4.1) of both the core-shell and tracer particles. Applying a series of filters (general contrast enchasing, sharpening, and thresholding) in ImageJ and counting the number of local maxima gives the number of the particles of interest per unit area. By varying the area of a local maximum, we can distinguish between small core-shell particles and larger tracers. This number can be further translated into the area fraction φ as

$$\varphi = \frac{N\pi a^2}{A} \qquad 4.13$$

where N is the number of the particles with radius a, and A is the area of the field of view. To check whether particle counting performed in ImageJ is correct we manually counted the number of the core-shell particles for one sample and found that the difference is below 5%.

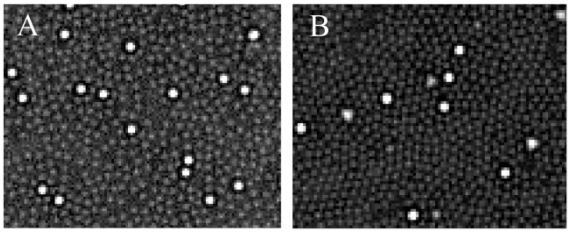

Figure 4.1. Examples of filtered phase contrast images of the core-shell and tracer microparticles at the air-water interface. Large bright spots are tracer particles. **(a)**: $\varphi = 0.18$ **(b)**: $\varphi = 0.42$. The number of the particles can be calculated as the number of local maxima in ImageJ.

In our experiments, the density of the tracer particles is always much lower than that of the core-shell particles. We therefore assume that the mobility of the tracers is affected by the core-shell particles, but not by other tracers.

4.4 One-point interfacial microrheology

4.4.1 Mean square displacement of the tracers

As expected, the trajectories of the tracer particles are more compact in denser layers, indicating that their motion is restricted by the core-shell particles. Representative trajectories at three different densities are shown in Fig. 4.2.

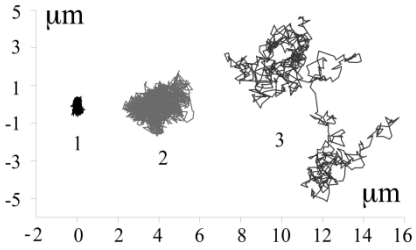

Figure 4.2. Examples of the trajectories of tracers exploring monolayers of core-shell particles at different surface densities, from left to right: φ_1 = 0.42, φ_2 = 0.27 and φ_3 = 0.18.

Recorded time-lapse image sequences were analyzed with the particle tracking routine [34] to obtain the MSDs of the tracers. In the layer with the lowest density (φ = 0.18), the tracer motion is diffusive throughout almost the whole range of time scales studied (Fig. 4.3, the top curve). By contrast, in the layer with the highest density φ = 0.42, the tracer particles are immobilized for time scales up to 70 seconds, before diffusive motion can be observed (Fig. 4.3, the bottom curve). This indicates caged motion of the tracers, followed by cage-hopping at long times, which is typical from tracers' trajectories exploring similar systems [14, 35]. Note that the amplitude of the fluctuations of the particles inside the cage is still above the resolution of our tracking algorithm (10^{-3} μm^2).

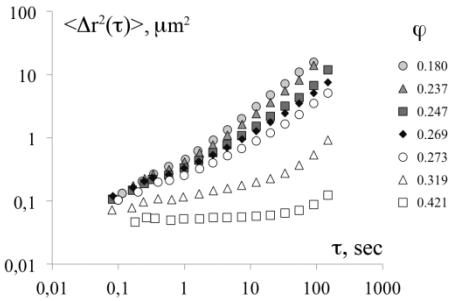

Figure 4.3. Double logarithmic plot of the mean square displacements of the tracers in monolayers of core-shell particles at different densities, as indicated in the table (densities are in the same order as that of the curves from top to bottom).

At time scales longer than 100 seconds all MSDs show diffusive behavior: the exponent α in $\langle \Delta r^2(t) \rangle \sim t^{\alpha}$ is close to 1. By contrast, for the short timescales (below 2 seconds) the MSDs show subdiffusive behavior with $\alpha < 1$. The MSD of the tracers inside the densest layer (φ = 0.42) shows α = 0.054; such subdiffusive behavior indicates that the core-shell particles form a monolayer with visco-elastic properties.

In the following sections we analyze the subdiffusive and diffusive regimes of the particle MSDs separately.

4.4.2 Analysis of the diffusive regime

From those regions of the MSDs where $\alpha = 1$ the surface viscosity η_s of the layers can be calculated using the Petrov-Schwille approximation (Equation 4.12); the results are plotted versus the area fraction φ in Fig. 4.3. Note that using the Saffman-Delbruck approximation (4.11) gave the same results for all monolayers except for the one with φ = 0.18.

Interestingly, we find that the interfacial viscosity found in this way increases approximately exponentially with the density of the monolayer: the data set can be fitted

with $\eta_s(\varphi) \sim e^{k\varphi}$ with $k \sim 25$. We find no sign of a divergence of the interfacial viscosity, which would indicate a glass transition.

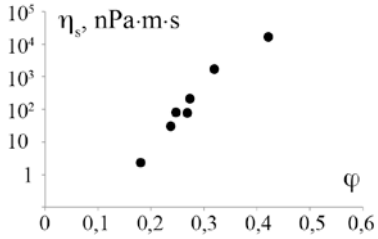

Figure 4.4. Effect of the core-shell particles surface density φ on the surface viscosity η_s of the monolayer, as extracted from the tracer diffusivity using Equation 4.12.

Exponential relations between viscosity and the concentration of the colloids have been observed in 3D suspensions too. In [36] the dependency of viscosity of hard sphere suspensions on the volume fraction has two regimes: an exponential relation for $\varphi_V < 0.41$ and a power law for $\varphi_V > 0.41$. Unfortunately we could not obtain data for higher area fractions to check whether the exponential law regime is followed by a power law regime in the case of the particle monolayers. We note also that the relation between interfacial viscosity and particle density found by us differs from that found by Reynaert et al. [6]. These authors found that their data (for weakly aggregated particles at a liquid interface) could be described by a 2D Krieger-Dougherty relation,

$$\eta_r = \left(1 - \frac{\varphi}{\varphi_m}\right)^{-[\eta]\varphi_m} \qquad 4.14$$

where φ_m is the maximum packing fraction at the interface and $[\eta]$ the intrinsic interfacial viscosity, predicted to be 2 for hard spheres in two dimensions. Our data, however, cannot be described by this equation, unless we use an unrealistically high value of 14 for $[\eta]$. The reasons for the difference between our results and those of Reynaert el al are not clear. Possibly, the approximations used in the 1-point interfacial microrheology approach do not apply here, so that the interpretation of the measured diffusion coefficients in terms of an interfacial viscosity is questionable.

4.4.3 Analysis of the subdiffusive regime

In this section we discuss the subdiffusive regime of the tracers' MSDs, where $\langle \Delta r^2(t) \rangle \sim t^{\alpha}$, with a subdiffusion exponent $\alpha < 1$. These regimes are indicated in Fig. 4.5a.

As can be seen in Fig. 4.5, the subdiffusion exponent α decreases with increasing layer density. This indicates that the motion of the tracer particles becomes restricted as the

density of core-shell particles increases. At very high densities the exponent becomes very close to zero, which indicates a complete caging of the tracers.

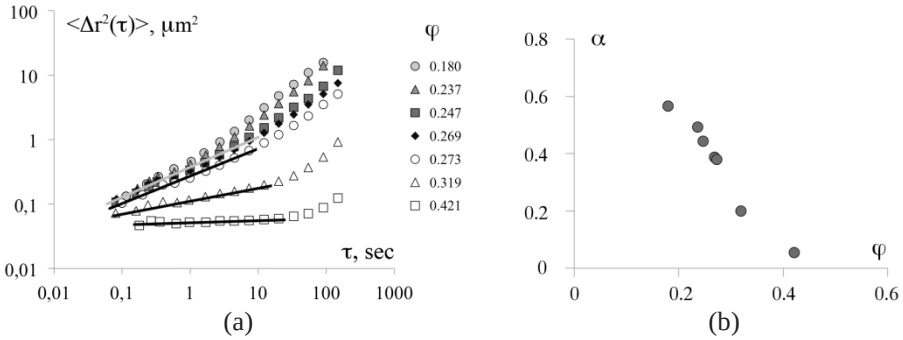

Figure 4.5. (**a):** Double logarithmic plot of the mean square displacements of the tracers from different layers; solid lines indicate the part, from which subdiffusive exponent α was calculated. **(b):** Subdiffusive exponent of the MSD in the subdiffusive regime, α is from $MSD \sim \tau^{\alpha}$.

The crossover time between the subdiffusive and diffusive regimes can be interpreted as the typical time for a tracer particle to escape from its local cage. This 'relaxation time' τ^* must be related to the dynamics of local rearrangements in the monolayer.

We obtain the crossover time from our experimental curves as shown in Fig. 4.6a and plot it as a function of the density of the monolayer in Fig. 4.6b. As expected, the crossover time increases with increasing layer density: at higher densities it takes more time for the particles to escape from their local cage. At very high surface densities the system is expected to jam completely, so that the relaxation time is expected to diverge at some critical density φ_m. However, in our data we could not reach high enough densities to observe such divergence.

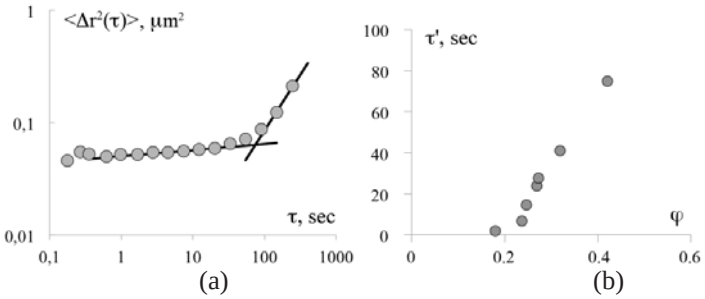

Figure 4.6 (a): Example of the crossover time finding. Two linear interpolations of $\log(\langle \Delta r^2(\tau) \rangle)$ versus $\log(\tau)$ are found first, and then their crossing point is calculated. **(b):** Crossover time τ^* versus the area fraction φ.

4.4.4 Analysis of displacement distributions

As shown by Weeks et al., the dynamics of particles become very heterogeneous as the colloidal glass transition is approached. This heterogeneity can be probed by analyzing the probability distribution $P(\Delta x)$ of displacements Δx along the x axis. We do this for our data in Fig. 4.7, for a number of different lag times, for a monolayer at a density of φ = 0.269. For time lags that are much shorter than the cage escape time, the distribution is well approximated by a Gaussian, as for Brownian motion in a homogeneous medium. However, for longer times the distribution deviates significantly from a Gaussian: shoulders appear, which indicate an increased probability of 'long jumps'. These long jumps correspond to that fraction of the particles that have escaped from their local cage.

Weeks et al. showed that this dynamic heterogeneity could be linked to the typical relaxation times related to cage escape, by characterizing the deviation from the Gaussian distribution in terms of a non-Gaussianity parameter [35, 37]. Unfortunately, our data were too noisy to obtain meaningful results from such an analysis. Nevertheless, the distributions in figure 4.7 indicate that dynamic heterogeneities are important also in the monolayers that we study here.

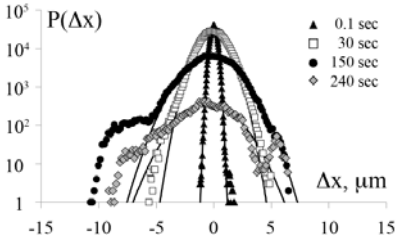

Figure 4.7. The probability distribution of tracer displacements in a monolayer at a density of φ = 0.269 for various time lags. Solid lines: Gaussian fits to the central bell-shaped curve.

4.5 Two-point microrheology

4.5.1 Cross-correlated particle mobility D_{rr}

For 3D systems, it is well known that 2-point microrheology gives a better agreement with macroscopic measurements than 1-point microrheology. Its application to interfaces was pioneered by Prasad et al [21]. Following their approach, we calculate D_{rr} using Equation 4.8 for different lag times τ and different particle-separations R; the result for three surface densities is shown in Fig. 4.8. For higher surface densities the cross-correlated diffusion becomes conserved over larger distances, but the magnitude decreases because of the restricted motion.

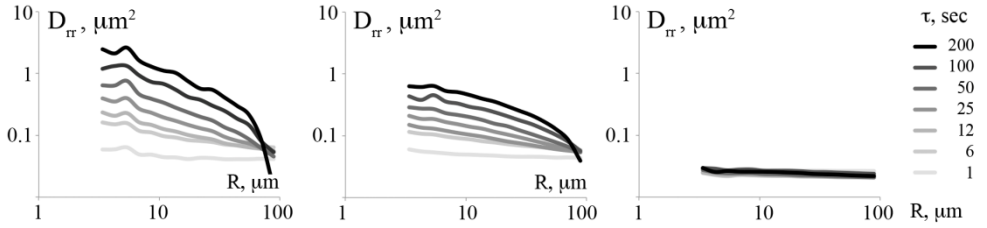

Figure 4.8. Correlated particle mobilities D_{rr} for different lag times τ and different separations R, for three different monolayers. Densities from left to right: φ = 0.18, φ = 0.27, φ = 0.42.

For purely viscous interfaces, where all particle motions are diffusive, the correlation function $D_{rr}(R,\tau)$ is proportional to the lag time τ [21]. As shown in Fig. 4.9, we observe that D_{rr}/τ becomes independent of τ only for long lag-times. For shorter times, D_{rr}/τ is larger, which means that the diffusivity at short times is larger than that at longer times. This is of course directly related to the caging effect observed in the single-particle MSDs. At short times, visco-elastic effects dominate, while at longer times, only viscous effects matter and the motions become diffusive. At higher particle densities, the crossover to diffusion occurs at longer times, just as for the 1-point data.

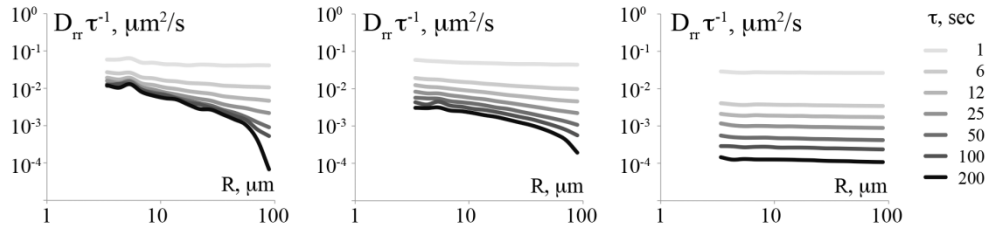

Figure 4.9. Correlated particle mobilities D_{rr}/τ for different lag times τ and different separations R, for three different monolayers. Densities from left to right: φ = 0.18, φ = 0.27, φ = 0.42.

For correlated motions in a 3D continuous medium, the longitudinal cross-correlation D_{rr} decays as $1/R$ (or, equivalently RD_{rr} is independent of R). However, for particles embedded in a visco-elastic liquid interface the R-dependence is different [21]. Our data show that for short lag times or for high particle densities, the measured $D_{rr}(R)$ dependence is weaker than $1/R$, Fig. 4.10.

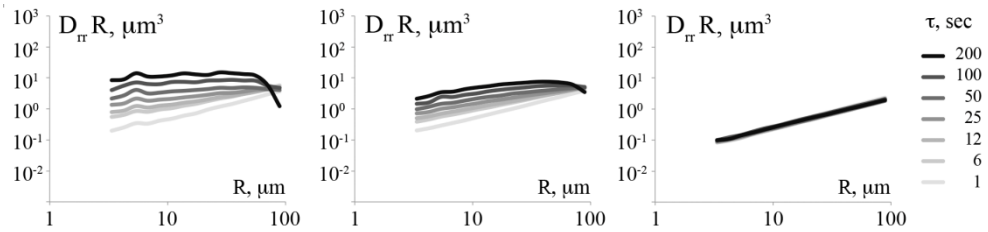

Figure 4.10. Correlated particle mobilities $D_{rr}R$ for different lag times τ and different separations R, for three different monolayers. Densities from left to right: φ = 0.18, φ = 0.27, φ = 0.42.

Such a weak dependence indicates that the correlations between the particles are very long-ranged. This is a direct consequence of the 2D nature of the interfacial flows, and is related to the famous Stokes paradox for 2D flows. Only for the lowest particle density and for long lag times do we find $D_{rr}{\sim}1/R$. For these interfaces, the interfacial viscosity is small and the drag on the interface is dominated by the viscosity of the bulk phase. A similar transition from a very weak R-dependence in the interfacial viscosity-dominated regime to the $1/R$ dependence in the bulk-viscosity-dominated regime was observed by Prasad et al. [21] for purely viscous protein-covered interfaces. Our results indicate that for visco-elastic interfaces, this transition depends on the time scale. Unfortunately, a procedure to extract the dynamic modulus of the interface from this distance dependence does not yet exist for visco-elastic interfaces.

4.5.2 Master curve for particle mobilities D_{rr}

The data shown in Fig. 4.8 show qualitatively different behavior of $D_{rr}(R)$ for different layers. It has been shown, however, that for purely viscous and homogeneous interfaces all these curves can be scaled onto a single master curve [21], by plotting a dimensionless correlation function $\overline{D}_{rr} = \langle D_{rr}/\tau \rangle / 2D_s$ versus a reduced separation $\beta = R/L$. Here, $D_s = kT/4\pi\eta_S$ and $L = \eta_S/\eta$ both depend on the surface-viscosity η_S. Theoretical predictions [32] show that such a master curve can be described by the following equation:

$$\overline{D}_{rr} = \left\{ \frac{\pi}{\beta} H_1(\beta) - \frac{2}{\beta^2} - \frac{\pi}{2} [Y_0(\beta) + Y_2(\beta)] \right\} \qquad 4.16$$

where $H_n(x)$ and $Y_n(x)$ are Struve functions and Bessel functions of the second kind, respectively.

Here, we test whether a similar rescaling applies to our data. For this, we consider only the time scales on which the motion is diffusive, so that D_{rr}/τ becomes constant. For the surface viscosities, we use the values obtained from the single-particle MSDs. The result of this rescaling is shown in Fig. 4.11. We see that all data except those for the highest particle density falls more or less on a master curve. However, the values for $\overline{D}_{rr}$ obtained from our

data are approximately one order of magnitude lower than the theoretical prediction (Equation 4.16). This indicates that for the particle-laden interfaces studied here, the interfacial viscosities obtained by the 1-point method underestimate the real interfacial viscosity. This is probably a result of the heterogeneity of the interface and the relatively small size of the tracer particles compared to the typical length scales at the interface.

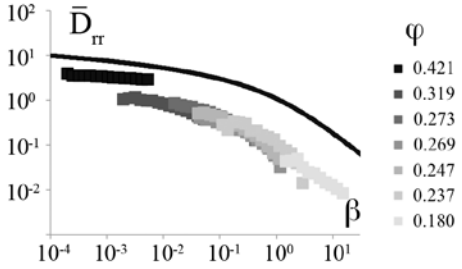

Figure 4.11. Master curve of rescaled cross-correlated mobilities $\bar{D}_{rr}$. Different symbols correspond to layers of different densities. Solid curve corresponds to the theoretical prediction, Equation 4.16.

4.6 Comparison of one- and two-point interfacial microrheology

4.6.1 Surface viscosity

As discussed in [13], the distinct mean-square displacement can be calculated from two-particle measurements by extrapolating the correlation functions $D_{rr}(R,\tau)$ to the bead size, $R = a$ (Equation 4.10). For homogeneous media, the distinct MSD thus obtained coincides with the measured 1-particle MSD. For heterogeneous media, however, the two differ. As shown by Prasad and Weeks [38], a similar extrapolation can be used for particles at an interface. It was shown that in this case the distinct MSD is obtained as $D_{rr}(R = a,\tau) = \langle \Delta r_r^2 \rangle_{2P}$. It follows that we can compare the results of 1P and 2P interfacial rheology by comparing $2\langle \Delta r_r^2 \rangle_{2P}$ to the measured 1P mean square displacement $\langle \Delta r^2 \rangle_{1P}$. Here, the factor 2 accounts for the fact that the 1P MSDs are measured in two dimensions, while the correlated motions are only measured along the axis through the two particles. Figure 4.12 shows the resulting comparison. It is clear from this figure that the 1P MSDs are much higher than the distinct 2P MSDs, in particular for the lower particle densities. Again, this indicates that 1P microrheology underestimates the viscosity of the interface, as compared to the 2P method. Only for the highest surface density at not too long time scales is there a reasonable comparison.

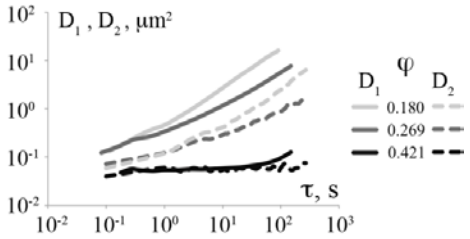

Figure 4.12. Comparison of one-point ($D_1 = \langle \Delta r^2 \rangle_{1P}$) and two-point ($D_2 = 2\langle \Delta r_r^2 \rangle_{2P}$) microrheology measurements for three different monolayers.

To compare 1-point and 2-point measurements of the surface viscosity we use the approach developed by Prasad et.al [21]. In this approach the scale factor $D_s = kT/4\pi\eta''_S$ is varied independently of $L = \eta_S/\eta$ (the latter is kept constant; η_S is from 1-point measurements) until each rescaled data set overlaps well with the theoretical prediction (Equation 4.16); the result is shown in Fig. 4.13. A comparison of η''_S found in this manner (2-point measurement) with η_S (1-point measurements) is shown in Fig. 4.14. This figure confirms our conclusion that 1-point microrheology underestimates the surface viscosity, in particular at low particle densities.

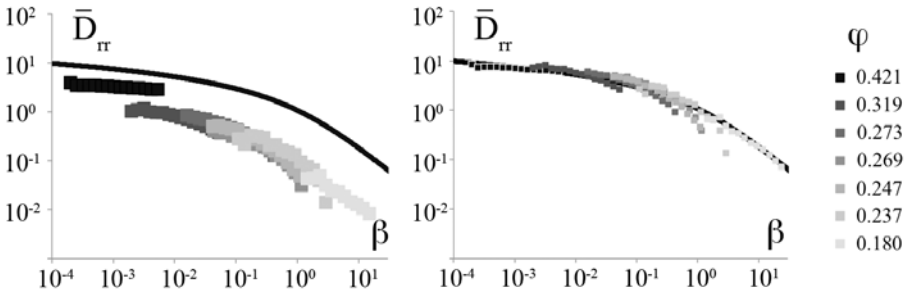

Figure 4.13. Master curve obtained with independent rescaling of $\bar{D}_{rr}$ and β. Different symbols correspond to layers of different densities. Solid curve corresponds to the theoretical prediction, Equation 4.16.

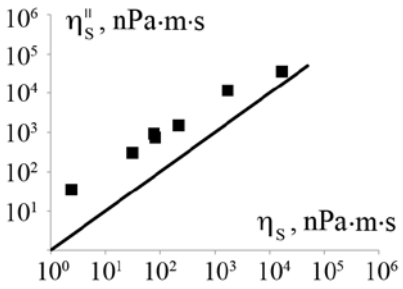

Figure 4.14. Comparison of 2P surface viscosity η''_S and 1P surface viscosity η_S.

4.6.2 Shear modulus

As discussed above, the time-dependent MSDs can be converted into a dynamic complex shear modulus $G^*(\omega) = G'(\omega) + iG''(\omega)$, by assuming that the generalized Stokes-Einstein relation (Equation 4.7) holds. For interfacial microrheology, however, this approach is not so straightforward, because the contribution of the adjacent bulk phases introduces logarithmic terms, as in Equation 4.11. We assume here that for interfaces with a high interfacial modulus, these corrections can be neglected, and adopt the following modified generalized Stokes-Einstein equation for the interface:

$$\tilde{G}(s) \approx \frac{k_B T}{\pi s \langle \Delta \tilde{r}^2(s) \rangle} \qquad 4.15$$

where $\tilde{G}(s)$ is the Laplace-transformed interfacial shear modulus (in N/m); Helfer et al. adopted a similar approach in [39]. Note that, contrary to the 3D case, this equation does not depend on the particle size. As in the Saffman-Delbruck model (Equation 4.11), the particle size appears only in the logarithmic corrections. From $\tilde{G}(s)$, the complex modulus $G^*(\omega)$ can be obtained by analytical continuation (replacing s by $i\omega$). Here, we use the method of Evans [40] to numerically perform the Laplace transform in Equation 4.14 needed to convert the MSDs into moduli.

We utilize this method to calculate the complex shear modulus for monolayers with different particle surface densities from both 1-point MSDs ($G^*_{1P}(\omega)$) and 2-point distinct MSDs ($G^*_{2P}(\omega)$); the result for 1-point measurements of storage and loss moduli G'_{1P} and G''_{1P} is shown in Fig. 4.15ab.

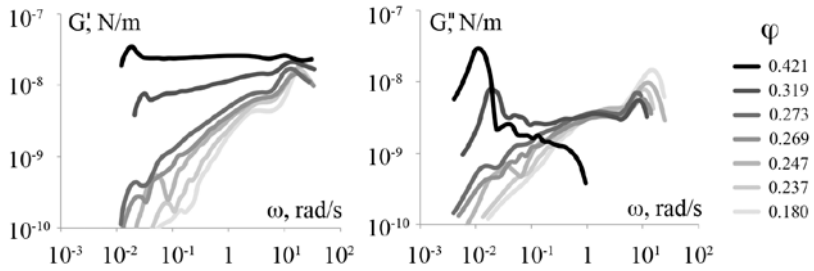

Figure 4.15. Effect of the particle area fraction φ on the storage and loss moduli G'_{1P} and G''_{1P}.

The values of the storage moduli $G'(\omega)$ taken at a fixed frequency ω = 1 rad/s are plotted versus φ for direct comparison of 1-point and 2-point measurements in Fig. 4.16.

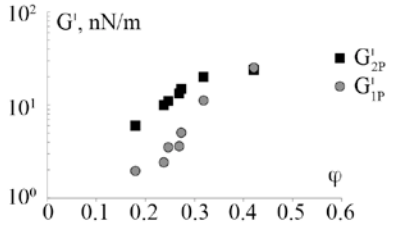

Figure 4.16. Comparison of the storage moduli G'_{1P} and G'_{2P} at the frequency ω = 1 rad/s versus area fraction φ. The scale is semi-logarithmic.

This result also confirms the discrepancy between 1-point and 2-point microrheology for low particle surface density, which is probably due to heterogeneity of the particle monolayers.

It should be noted, however, that the analysis based on Equation 4.14 is at best an approximation. In particular for low particle densities, bulk contributions cannot be neglected.

4.7 Concluding remarks

Particle-tracking based microrheology is a promising tool for characterization of the visco-elastic properties of liquid interfaces. One of the biggest advantages of this method is that it can be applied for samples that cannot be studied with traditional macrorheology methods.

Mechanical properties of the interfaces such as viscosity, elasticity, relaxation times can be obtained from the MSDs of tracers. However, care must be taken to interpret 1-point MSDs in terms of viscosity and elasticity, since they may be an underestimation because of heterogeneities in the medium or local structure changes induced by the tracers themselves [13].

These issues can be overcome by 2-point microrheology, which has been shown to give results consistent with macrorheology for bulk (3D) samples. However, in the case of interfacial microrheology further development is needed, for example, to decouple the effect of the visco-elastic layer and the bulk flows on the correlated motion of tracers [32]. It could be very interesting to check whether the model developed by Levine and Mackintosh in [32] captures the experimental reality well not only for viscous layers [21], but also for visco-elastic interfaces.

One way to do so is to measure the complex diltational and shear moduli by the means of macrorheology and check whether their combination according to [32] is consistent with 2-point interfacial microrheology measurements. For that, a specific experimental system that would be suitable for measurements with three different techniques needs to be

developed. As a related question, the effect of the tracer size as compared to typical length scales in visco-elastic interface on mirorheological measurements should be studied.

Developing experimental setups allowing for continuous increase of the particle surface density (such as Langmuir trough) combined with simultaneous microscopy observations could give additional insight into the transitions happening in the particle monolayer. It could be interesting to see whether there is a hexatic phase preceding the glass transition and study the accompanying transitions in visco-elastic properties of the monolayer.

References

1. Dickinson, E., *Milk protein interfacial layers and the relationship to emulsion stability and rheology.* Colloids and Surfaces B-Biointerfaces, 2001. **20**(3): p. 197-210.
2. Durand, M. and D. Langevin, *Physicochemical approach to the theory of foam drainage.* European Physical Journal E, 2002. **7**(1): p. 35-44.
3. Dickinson, E., *Interfacial structure and stability of food emulsions as affected by protein-polysaccharide interactions.* Soft Matter, 2008. **4**(5): p. 932-942.
4. Dickinson, E., *Proteins at interfaces and in emulsions - Stability, rheology and interactions.* Journal of the Chemical Society-Faraday Transactions, 1998. **94**(12): p. 1657-1669.
5. Kralchevsky, P.A., N.D. Denkov, and K.D. Danov, *Particles with an undulated contact line at a fluid interface: Interaction between capillary quadrupoles and rheology of particulate monolayers.* Langmuir, 2001. **17**(24): p. 7694-7705.
6. Reynaert, S., P. Moldenaers, and J. Vermant, *Interfacial rheology of stable and weakly aggregated two-dimensional suspensions.* Physical Chemistry Chemical Physics, 2007. **9**(48): p. 6463-6475.
7. Kasper Masschaele, S.V., Jan Vermant, Basavaraj Madivala, *Interfacial Rheology*, in *Rheology*
8. Stokes, G.G. and G.G. Stokes, *On the Effect of the Internal Friction of Fluids on the Motion of Pendulums, Mathematical and Physical Papers*. 2009: Cambridge University Press.
9. Einstein, A. and R. Fürth, *Investigations on the Theory of the Brownian Movement.* 1956: Dover Publications.
10. Mason, T.G. and D.A. Weitz, *Optical Measurements of Frequency-Dependent Linear Viscoelastic Moduli of Complex Fluids.* Physical Review Letters, 1995. **74**(7): p. 1250-1253.
11. Squires, T.M. and T.G. Mason, *Fluid Mechanics of Microrheology.* Annual Review of Fluid Mechanics, 2009. **42**(1): p. 413-438.
12. Ortega, F., H. Ritacco, and R.G. Rubio, *Interfacial microrheology: Particle tracking and related techniques.* Current Opinion in Colloid & Interface Science, 2010. **15**(4): p. 237-245.

13. Crocker, J.C., et al., *Two-point microrheology of inhomogeneous soft materials.* Physical Review Letters, 2000. **85**(4): p. 888-891.
14. Oppong, F.K., et al., *Microrheology and structure of a yield-stress polymer gel.* Physical Review E, 2006. **73**(4).
15. Palmer, A., et al., *Diffusing wave spectroscopy microrheology of actin filament networks.* Biophys J, 1999. **76**(2): p. 1063-71.
16. Wirtz, D., *Particle-Tracking Microrheology of Living Cells: Principles and Applications.* Annual Review of Biophysics, 2009. **38**: p. 301-326.
17. Buchanan, M., et al., *Comparing macrorheology and one- and two-point microrheology in wormlike micelle solutions.* Macromolecules, 2005. **38**(21): p. 8840-8844.
18. Starrs, L. and P. Bartlett, *One- and two-point micro-rheology of viscoelastic media.* Journal of Physics: Condensed Matter, 2003. **15**(1): p. S251.
19. Gardel, M.L., et al., *Microrheology of entangled F-actin solutions.* Physical Review Letters, 2003. **91**(15).
20. McGrath, J.L., J.H. Hartwig, and S.C. Kuo, *The mechanics of F-actin microenvironments depend on the chemistry of probing surfaces.* Biophys J, 2000. **79**(6): p. 3258-66.
21. Prasad, V., S.A. Koehler, and E.R. Weeks, *Two-particle microrheology of quasi-2D viscous systems.* Physical Review Letters, 2006. **97**(17).
22. Liu, J., et al., *Microrheology probes length scale dependent rheology.* Physical Review Letters, 2006. **96**(11).
23. Crocker, J.C. and B.D. Hoffman, *Multiple-particle tracking and two-point microrheology in cells.* Cell Mechanics, 2007. **83**: p. 141-178.
24. Cicuta, P. and A.M. Donald, *Microrheology: a review of the method and applications.* Soft Matter, 2007. **3**(12): p. 1449-1455.
25. Saffman, P.G. and M. Delbruck, *Brownian motion in biological membranes.* Proc Natl Acad Sci U S A, 1975. **72**(8): p. 3111-3.
26. Smoluchowski, M., *On the practical applicability of Stokes' law of resistance and its modifications required in certain cases.* Pisma Mariana Smoluchowskiego, 1927. **2(1)**: p. 195-208.
27. Klingler, J.F. and H.M. McConnell, *Brownian motion and fluid mechanics of lipid monolayer domains.* The Journal of Physical Chemistry, 1993. **97**(22): p. 6096-6100.
28. Naji, A., A.J. Levine, and P.A. Pincus, *Corrections to the Saffman-Delbruck mobility for membrane bound proteins.* Biophysical Journal, 2007. **93**(11): p. L49-L51.
29. B. D. Hughes, B.A.P.a.L.R.W., *The translational and rotational drag on a cylinder moving in a membrane.* Journal of Fluid Mechanics, 1981. **110**: p. 349-372
30. Petrov, E.P. and P. Schwille, *Translational diffusion in lipid membranes beyond the Saffman-Delbruck approximation (vol 94, L41, 2008).* Biophysical Journal, 2012. **103**(2): p. 375-375.

31. Gambin, Y., et al., *Lateral mobility of proteins in liquid membranes revisited.* Proc Natl Acad Sci U S A, 2006. **103**(7): p. 2098-102.
32. Levine, A.J. and F.C. MacKintosh, *Dynamics of viscoelastic membranes.* Physical Review E, 2002. **66**(6).
33. Ho, C.C., et al., *Fabrication of Monolayer of Polymer/Nanospheres Hybrid at a Water-Air Interface.* Acs Applied Materials & Interfaces, 2011. **3**(2): p. 204-208.
34. Kilfoil, M., *Biological Physics Lab Webpage: http://people.umass.edu/kilfoil/downloads.html*.
35. Weeks, E.R., et al., *Three-dimensional direct imaging of structural relaxation near the colloidal glass transition.* Science, 2000. **287**(5453): p. 627-31.
36. Phillies, G.D.J. *Viscosity of Suspensions of Hard and Soft Spheres*. 2004.
37. Zheng, Z.Y., F. Wang, and Y.L. Han, *Glass Transitions in Quasi-Two-Dimensional Suspensions of Colloidal Ellipsoids.* Physical Review Letters, 2011. **107**(6).
38. V. Prasad, E.R.W., *2D to 3D transition in soap films demonstrated by microrheology.* Phys. Rev. Lett., 2009. **102**: p. 178302
39. Helfer, E., et al., *Viscoelastic properties of actin-coated membranes.* Physical Review E, 2001. **63**(2): p. art. no.-021904.
40. R M L Evans, M.T., Dietmar Auhl, Thomas A Waigh, *Direct conversion of rheological compliance measurements into storage and loss moduli.* Phys. Rev. E, 2009. **80**: p. 012501.

CHAPTER 5

MICRORHEOLOGY OF THIN ACTIN LAYERS RECONSTITUTED AT OIL WATER INTERFACES

In this chapter we study the visco-elastic properties of a thin, quasi-2D model of the cell actin cortex, which we reconstitute from cross-linked actin filaments anchored at the surface of oil droplets. Such actin containing systems are known to contract and stiffen in the presence of myosin and ATP; this kind of contraction naturally occurs in muscles and cell cortex.

We utilize interfacial microrheology to investigate the effect of cross-linker density and the length of the actin filaments on the mechanical properties of the 2D network; we also observe and characterize strong and rapid stiffening of the 2D-networks in the presence of myosin and ATP.

This chapter is based on: Dmitry Ershov, Martien Cohen Stuart, Jasper vander Gucht, “Mechanical properties of reconstituted actin networks at an oil–water interface determined by microrheology”, Soft Matter, 2012.

5.1 Introduction

The mechanical properties of living cells are determined mainly by the cytoskeleton, a complex network composed of a variety of protein filaments that are cross-linked with other proteins. One of the main constituents of the cytoskeleton is actin, a protein, which assembles into long, semiflexible filaments that are organized into bundles and networks by different types of cross-linking proteins. In many cells, actin filaments form a dense, thin network that is attached to the plasma membrane. This thin, quasi-2D actin network is called the cell cortex. Motor proteins called myosin bind to this network and in the presence of ATP generate contractile forces that actively stiffen the cortex. These active contractions are thought to play an important role in various cellular processes, such as cell migration [1], establishing cell polarity [2, 3], and cytokinesis [4]. Understanding the visco-elastic properties of the cortical actin network is therefore a crucial step towards a detailed understanding of the mechanics of these cellular processes.

There have been a number of approaches to study the physical properties of the cytoskeleton and the actin cortex in living cells. These include micropipette aspiration [5, 7], atomic force microscopy [8, 9], and particle tracking-based microrheology [10, 13]. However, the highly complex architecture of cells makes it very difficult to relate the mechanical response measured with these techniques to the properties of the underlying cytoskeletal network. Therefore, many authors have studied simplified model systems, consisting of purified actin filaments, mixed with cross-linking or motor proteins [14-20]. Thanks to these in-vitro studies, we now have a very good understanding of how the visco-elastic properties of isotropic 3D actin networks depend on the concentrations of filaments and cross-linkers.

Much less is known about the mechanical properties of membranes coated with a thin actin layer. Several groups have attempted to reconstitute an artificial model system that mimics the structure of the cortex. Most of these studies involve actin networks attached to lipid vesicles [21] or confined to the interior of a vesicle [22-24]. The mechanical properties of actin-coated membranes were studied by manipulating attached beads with optical tweezers [25, 26] or by observing thermally induced bilayer expansions [27]. Others have confined actin filaments inside emulsion droplets [28], fixed them to arrays of pillars [29] or adsorbed the filaments to an air/water interface covered with a phospholipid monolayer [30-33].

In this chapter we present a model system for the cell cortex that captures its principal features and at the same time allows for a quantitative and systematic study of the structural and mechanical properties of the network. To achieve this, we attach actin filaments to the oil/water interface of an emulsion droplet, which is stabilized with a phospholipid monolayer. We visualize the actin layer around the droplet by means of confocal microscopy and we study its visco-elastic properties utilizing interfacial microrheology. We study how the visco-elastic properties of the reconstituted actin cortex depend on the cross-linker concentration and on the length of the filaments and show that addition of myosin

and ATP causes a very strong stiffening of the cortex due to contraction of the actin-myosin network.

5.2 Experimental details

5.2.1 Actin and Myosin filaments

Actin, biotinylated actin (b-actin, after purification actin has been modified to contain covalently linked biotin at random surface lysine residues), myosin II (from rabbit muscle), and gelsolin were obtained from Cytoskeleton Inc. Actin solutions were prepared by dissolving lyophilized actin in G-buffer (5 mM Tris-Cl pH 8.0, 0.2 mM $CaCl_2$, 0.5 mM DTT, 0.2 mM ATP) to a concentration of 12 μM. The fraction of biotinylated actin was 10%, and for visualization of the network we added 10% of actin labeled with Alexa Fluor-597 (Molecular Probes). Actin polymerization was initiated by adding a small volume of 3 M KCl to the sample, resulting in a final KCl concentration of 100 mM. Actin filaments were left to grow at room temperature for 40 minutes. These biotinylated filaments can be cross-linked with streptavidin, which has four biotin-binding sites (Fig.1a).

To study the effect of filament length, actin was polymerized in the presence of varying amounts of gelsolin, which caps the barbed end of a filament preventing its further growth (Fig.1b). Actin filaments were visualized with atomic force microscopy (AFM); the samples prepared as follows. Polylysine-modified silica substrates were dipped into a solution of the actin filaments and then rinsed to remove unabsorbed material. After drying, the samples were imaged using a Veeco Nanoscope V AFM in Scan-Assist mode with Veeco tips (model NP-10, tip C). The contour lengths of 500-1000 filaments were measured for each gelsolin concentration to obtain the length distribution. The averages for the length distributions are shown in the Results section.

Myosin II protein was stored in a high-salt buffer (100 mM Imidizole pH 7.5, 2.4 M KCl, 0.2 mM DTT, 5% sucrose and 1% dextran) in which it cannot assemble into filaments. Filamentous myosin solutions were prepared by dialysis [34, 35] against 100 mM KCl, pH 7.5 and stored at -20°C. Before incorporating myosin filament into the networks of interest (Fig. 5.1c), they were checked for activity. Myosin and actin filaments were mixed at molar ratio 0.042; microparticles were added to the mixture for visualization of contraction after addition of ATP [36].

5.2.2 Streptavidin-coated droplets

A mixture of lipids in chloroform (1, 2-didocosahexaenoyl-sn-glycero-3-phosphocholine (22:6 Cis PC) and 1,2-dioleoyl-sn-glycero-3-phosphoethanolamine-N-(cap biotinyl) (18:1 Biotinyl Cap PE) (both from Avanti lipids) was dried under nitrogen and dissolved in mineral oil (Sigma Aldrich, heavy mineral oil, density 0.862 g/mL) to

concentrations of 1 mg/mL and 0.25 mg/mL respectively, and then dispersed by sonication for 30 minutes.

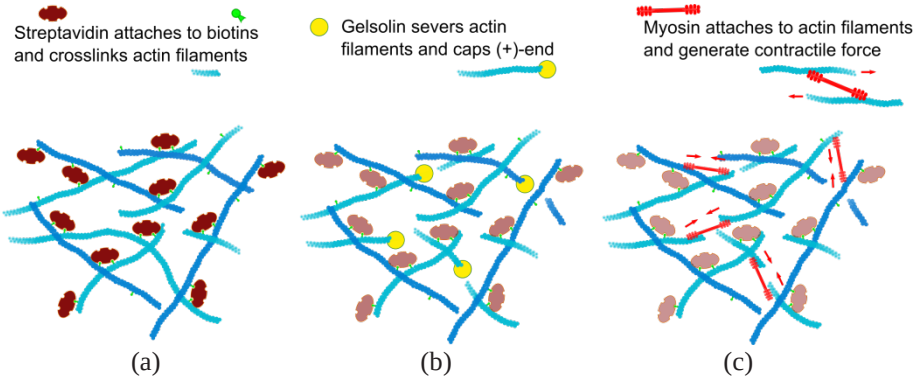

Figure 5.1. Diagram showing the function of each protein used in this study. Long filaments: actin, ovals: streptavidin, circles: gelsolin, short filaments: myosin.

Oil in water emulsion (oil to water volume ratio 0.04) was obtained by dispersing freshly prepared oil/lipid mixture in G-buffer containing different amounts of streptavidin (Pierce Biotechnology), leading to droplets covered with various amounts of streptavidin (which gives various density of cross linker). For visualization, we used streptavidin labeled with Alexa Fluor-633 (Pierce Biotechnology). We estimate the density of streptavidin molecules on the surface of the droplets from the fluorescence intensity of the surface, using a calibration plot measured for samples with known adsorbed amounts of streptavidin.

5.2.3 Actin-coated droplets with embedded particles

For the microrheology experiments, 0.3 μL of 1w/w% fluorescently labeled particles with streptavidin-modified surface (Sigma, latex beads 250 nm diameter, carboxilate-modified, streptavidin-labeled, yellow-green) was added to 500 μL of the emulsion together with the free streptavidin protein. The particles and the free streptavidin both bind to the biotin groups on the oil/water interface. Emulsion samples were checked first with the confocal microscope to see if the particles are evenly dispersed on the surface of the droplets without aggregation, and if the surface contains homogeneously distributed streptavidin (see supporting information).

Then 20 μL of freshly prepared emulsion was mixed with 20 μL of the actin solution, giving a final actin concentration of 6 μM. The negative charge on the biotinylated lipids minimizes non-specific adsorption of streptavidin and actin (both negatively charged at the working conditions pH ~8), so that it is reasonable to assume that nearly all streptavidin on

the surface is bound to the biotinylated lipids and that the actin filaments are linked to the surface through biotin-streptavidin bonds.

We found that the structure of the actin network on the droplet's surface is highly sensitive to the lipid composition on the surface. Without unsaturated lipids, clustering of biotinylated lipids and streptavidin-modified particles occurred, giving very inhomogeneous and stiff layers, probably due to crystallization of the lipids. This clustering could be prevented by adding 1 g/L of unsaturated lipids in the oil mixture. In all our experiments, we used unsaturated lipids for which crystallization did not occur, as seen with confocal microscopy.

5.2.4 Observation with confocal microscope

After mixing the emulsion with the actin-containing solution, the mixture was placed in a sample chamber made from a standard microscopy glass slide (Menzel-Glaser, 76x26) and a cover slide (Menzel-Glaser, No 1), separated from each other by two strips of parafilm, giving a chamber of 100 μm height and a total volume of ~12 μL. The chamber was sealed with a mixture of lanolin, vaseline and paraffin (1:1:1). After 10-20 minutes incubation, the samples were studied with the confocal microscope (Zeiss 200M Axiovert, LSM5 Exciter) using an oil immersion objective (100x, NA 1.4). The scan area was reduced to 13 μm x 13 μm and the scanning in "both directions" was switched on to increase the scan speed to 13 slides per second with still sufficiently good contrast of the images, even with relatively low laser transmission values (3-7%). The thickness of the optical slice, set by the pinhole, was 0.7 μm.

5.2.5 Particle tracking and microrheology

To examine the visco-elastic properties of the layers, we monitor the motion of the embedded tracer particles. Movies of about 190 seconds were taken, with a frame rate of 13 fps. Only droplets that were stuck to the cover slip were studied in order to avoid drift in the obtained data. All movies were taken in less than 6 hours after sample preparation (for the experiments with gelsolin less than 1 hour). During this time, the layers appeared homogeneous and their properties were stable and reproducible.

For analysis of the movies MATLAB (The Mathworks, Natick, MA) was used. To track the particles we used a script developed by the Kilfoil group [18, 37], which is based on the tracking algorithm developed by Crocker and Grier [38]. We use the 2D tracking algorithm, which tracks particles in the XY plane. We only consider particles that are situated near the top of the droplet, as shown in Fig. 5.2. For these particles, the distance travelled in the z-direction during a time series could be neglected. Particles situated farther from the top (or the bottom) of a droplet do move in the z-direction. These particles, which are out of focus, were therefore ignored. To check the position resolution of our experimental setup, we

immobilized particles on a glass slide and tracked their position. We found that the spatial resolution for our experimental setup is about ±30 nm, which means that the lower limit of mean square displacements that we can detect is approximately 10^{-3} μm^2.

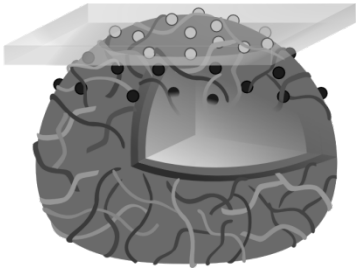

Figure 5.2. A droplet and its top, from which the movies of the tracer particles were recorded. The black particles were not observable in the movie due to the thin slice that the confocal microscopy is able to scan.

5.3 Results

5.3.1 Constructing an artificial actin cortex

Our strategy to develop a simplified model system that mimics the composite actin/membrane cortex in cells is illustrated in Fig. 5.3. Helfer et al. [25, 26] have shown that actin-filaments can be attached effectively to a lipid vesicle using biotin-streptavdin links. Here, we modify their approach to attach actin filaments to a layer of phospholipids adsorbed at the oil/water interface. First an oil in water emulsion is prepared that is stabilized by a layer of phospholipids adsorbed at the oil/water interface of the droplets. About 20% of the lipids have a biotin group. Varying amounts of streptavidin were then added to the emulsion and allowed to bind to the biotinylated lipids. After this, preformed biotinylated actin filaments were added. Actin filaments are attached to the streptavidin on the droplets via the biotin groups distributed over the filament. Biotin labels occur every ~10 unlabeled actin monomers and are thus separated by ~30 nm. Using confocal microscopy with fluorescently labeled actin and streptavidin, it was checked that streptavidin and actin were indeed attached to the droplets (Fig. 3c, d). It was noticed, that the amount of actin on the surface increases slightly with increasing streptavidin amount by ~50% between the lowest and highest streptavidin concentration.

The molar concentration of biotinylated lipids is ~2500 times larger than that of streptavidin at the highest concentration. Assuming that each phospholipid molecule occupies an area of around 0.5 nm^2 and that the lipids are homogeneously mixed, this gives approximately 0.4 biotin groups per nm^2. Because of the high strength of the biotin-streptavidin bond it is reasonable to assume that all streptavidin is attached to biotin heads

exposed at the surface of oil droplets, and that no streptavidin is left in the bulk of the solution.

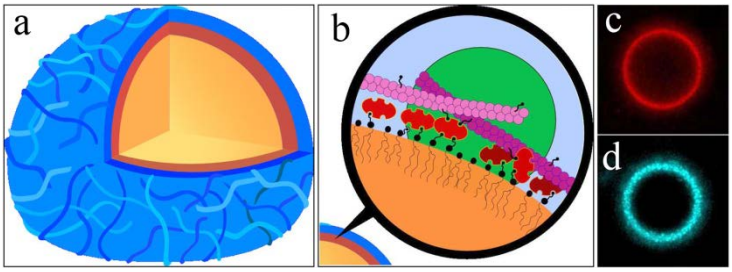

Figure 5.3. (a) Schematic picture of the artificial cortex; from outer layers: actin filaments, streptavidin layer, and the bulk is the oil; **(b)** zoom-in on the interface: biotinylated filaments are cross-linked and attached to biotinylated lipids via streptavidin; streptavidin-modified particle (large circle) is attached to the biotinylated lipids; confocal microscope images showing **(c)** streptavidin layer and **(d)** actin layer around the same droplet.

This is confirmed by our observation that the amount of streptavidin on the surface (proportional to the total fluorescence intensity in that area, I^*) does not increase when biotinylated actin binds to the surface, creating additional binding sites for streptavidin, Fig. 5.4. An increase at the lowest concentration of streptavidin is due to the bleed-through of actin label, which becomes negligible at higher concentrations of streptavidin.

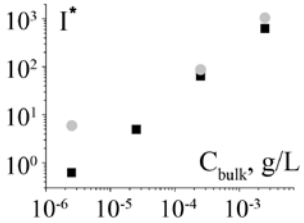

Figure 5.4. Streptavidin binding to droplets containing biotinylated lipids, in the absence (■) and in the presence (●) of actin.

Moreover, actin filaments found in the bulk of the solution do not show any binding of streptavidin (by contrast, if no biotinylated lipids were used, large actin-streptavidin bundles were observed in the bulk solution).

Because a streptavidin molecule has 4 biotin binding sites, each streptavidin attached to a lipid can still bind 3 biotins. This means that the streptavidin molecules on the interface can bind multiple actin filaments simultaneously. In all our experiments, the number of biotinylated actin monomers is at least 10 times higher than the number of streptavidin molecules, so that it is very likely that most of the streptavidin molecules are attached to at least two filaments. We therefore expect that most streptavidin molecules act both as surface anchors and as filament cross-linkers.

The obtained emulsion is polydisperse, which makes it difficult to calculate the total area of the oil-water interface. Therefore, we use the fluorescence intensity of labeled streptavidin (Fig. 5.3c) as a measure for the amount of streptavidin on the surface. We first measure the fluorescence intensity of labeled streptavidin adsorbed onto solid polystyrene particles (with known surface area) to calibrate the fluorescence signal (see Appendix).

We find that the density of streptavidin on the oil/water interface in our experiments varies between 0.00025 and 0.27 molecules per nm^2. The maximum coverage found in this way is about 5 times higher than that on the solid polystyrene surface, indicating that the molecules occupy less space on the oil/water interface. This difference might be due to unfolding of the streptavidin at solid surfaces or to the flexible spacer that links the biotin head to the tail of the lipid, giving more freedom for a streptavidin molecule. The thickness of the obtained actin layer is comparable to the size of the particles (250 nm). Because this is close to the optical resolution limit (260 nm for 597 nm wavelength, NA = 1.4), a more precise measurement of the thickness cannot be done. The thickness is small compared to the persistence length of the filaments, so that the layer can be regarded as a quasi-2D layer.

5.3.2 Effect of streptavidin

To characterize the visco-elasticity of the actin network attached to the oil/water interface, we embedded streptavidin-coated particles (diameter 250 nm) in the layer. The particles were added to the emulsion after the attachment of the actin filaments to the interface. The particles bind to the interface through biotin-streptavidin links with remaining free biotin groups on the lipids or actin filaments. Their movement was tracked using time-lapse confocal microscopy at a rate of 13 frames per second.

The particles embedded into the network showed different behavior depending on the concentration of streptavidin. Typical particles' trajectories for an interface without attached actin and for actin-coated interfaces at different surface densities of streptavidin are shown in Fig. 5.5a. On an interface without actin, or on actin-coated interfaces with low streptavidin concentration, particles explore the interface freely as can be seen from the relatively large particle displacements. Upon increasing the streptavidin concentration, the trajectories become more localized, meaning that the increased cross-linking of the network restricts the particle motion.

To analyze the trajectories of the beads in a more quantitative way, we calculate the mean square displacements (MSDs) for each STA concentration; the MSDs are shown in Fig. 5.5b. In the absence of actin filaments, the mean square displacement of the particles increases linearly with time, irrespective of the amount of streptavidin on the interface, indicating free diffusion on a purely viscous interface.

The diffusion coefficient of the particle can be obtained from the slope of the MSD and is 0.041 $\mu m^2/s$.

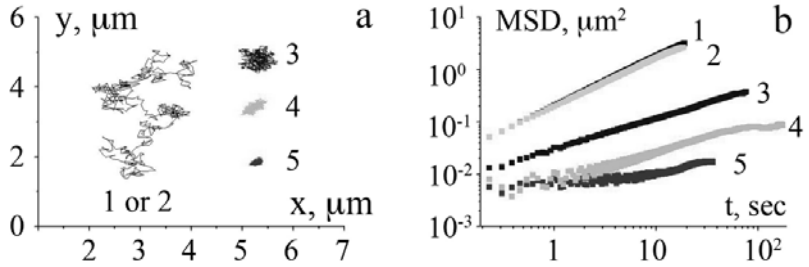

Figure 5.5. Typical trajectories **(a)** and MSDs **(b)** of particles attached to interfaces with no actin (1); actin at different streptavidin densities: 0.00025 nm^{-2} (2), 0.002 nm^{-2} (3), 0.027 nm^{-2} (4), 0.27 nm^{-2} (5).

As derived by Saffman and Delbruck [39], the diffusion coefficient of a particle on an interface D_{2D} depends both on the interfacial viscosity η_s and on the bulk viscosity of water η:

$$D_{2D} = \frac{k_B T}{4\pi\eta_S}\left[\ln\left(\frac{\eta_s}{\eta a}\right) - \gamma_E\right] \qquad 5.1$$

where a is the particle radius (125 nm) and γ_E = 0.5572 is Euler's constant. Equation 5.1 is valid if $\eta_S \gg \eta a$. Using the measured diffusion coefficient, we find η_S = 0.23 nNs/m. Since this is only two times larger than ηa = 0.125 nNs/m, the applicability of Equation 1 is questionable. Using Petrov-Schwille extension of the Saffman-Delbruck equation [40] for $\eta_S \sim \eta a$, we find η_S = 0.41 nNs/m.

For the actin-coated surface at the lowest streptavidin concentration, the mean square displacement of the particles is almost the same as that on an actin-free surface. However, an increase in the amount of streptavidin results in a decrease of the MSD, showing that the streptavidin cross-links restrict the particle motion. The slope of the MSD becomes smaller, indicating subdiffusive behavior, and at longer times the MSD levels off towards a plateau. This means that the particles become trapped in a cage and indicates elastic behavior of the surface. Hence, the surfaces become visco-elastic upon streptavidin addition.

Mason and Weitz in [41] related the MSD for particles embedded in a 3D material to the complex shear modulus $G^*(\omega)$ of the material, by generalizing the Stokes-Einstein relation to all frequencies. In the Fourier-domain it reads:

$$Fu[\langle\Delta r^2(t)\rangle] = \frac{kT}{\pi a i\omega G^*(\omega)} \qquad 5.2$$

where $Fu[\langle\Delta r^2(t)\rangle]$ denotes the unilateral Fourier transform of the mean square displacement. The extension of the GSER to diffusion on an interface is not straightforward, because there are also contributions from the bulk viscosity, leading to logarithmic corrections [42] as in Equation 5.1. Because the MSDs that we measure at high streptavidin concentrations indicate that the effect of the visco-elastic surface on the particle motion is large compared to the effect of the bulk viscosity, we assume that we can neglect the logarithmic contributions and adapt Equation 5.2 to our 2D system:

$$G^*_{2D}(\omega) = \frac{kT}{\pi i \omega F u[\langle \Delta r^2(t) \rangle]} \qquad 5.3$$

A similar approximation was used by Helfer et al. to study the diffusion of particles embedded in visco-elastic membranes [26]. In order to obtain the complex shear modulus of the surface using Equation 5.3, we need to perform a unilateral Fourier transform of the MSD. We use the approximate method of Mason et. al. [43] to do this. The results are shown in Fig. 5.6.

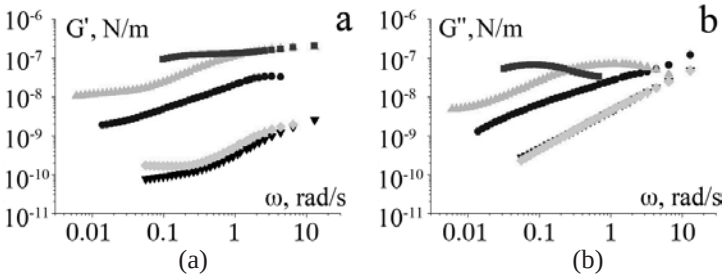

Figure 5.6. Effect of streptavidin density on the storage **(a)** and loss **(b)** moduli of the cortex. Surface concentrations of streptavidin are: 0.27 nm^{-2} (■), 0.027 nm^{-2} (▲), 0.002 nm^{-2} (●), 0.00025 nm^{-2} (♦), 0.27 nm^{-2} with no actin (▼).

It must be noted here that 1-point microrheology is known to underestimate the visco-elastic moduli of bulk actin gels, and that these problems can be overcome by using 2-point cross-correlation microrheology [44]. However, as the current 2-point algorithms are not fully adapted for interfacial microrheology of visco-elastic interfaces [42, 45], we only use 1-point microrheology here.

For low streptavidin concentrations or for surfaces without actin, the loss modulus dominates and increases linearly with frequency, indicating that the surface is purely viscous. At higher streptavidin amounts, the storage modulus becomes more important and its frequency dependence becomes weaker, indicating more elastic behavior. Helfer et al. observed a power-law frequency dependence of the complex shear modulus for actin-coated vesicles at high frequencies (ω > 100 rad/s), [26] with an exponent of 0.85. This can be ascribed to bending modes of single filaments. In our experiments we may be seeing such a regime at intermediate cross-linking densities (Fig. 5.6: 0.002 nm^{-2} with the slope 0.63). At even higher frequencies, one would expect the bulk viscosity to become more important, but our observable frequency range is too small to see this.

For the most densely cross-linked networks, the storage moduli have a plateau region at low frequencies, which corresponds to the plateaus in the MSD at longer times.

The effect of streptavidin on the low-frequency modulus G_0 is shown in Fig. 5.7. It is found to increase approximately linearly with increasing streptavidin density. A similar linear increase was found for 3D networks cross-linked by filamin [15] and for actin

networks attached to the air/water interface [33]. A proportional increase of the modulus with increasing crosslink density is expected for affinely deforming networks [46].

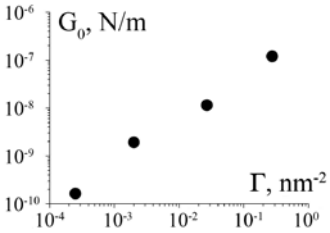

Figure 5.7. Effect of streptavidin on the low-frequency modulus G_0 of the cortex.

We note that the slight increase of the actin density at the surface with increasing streptavidin density may also contribute to the increase of the modulus. However, because this increase is modest, we assume that this contribution is small compared to that of the increased cross-link density.

5.3.3 Effect of gelsolin

Gelsolin is an actin binding protein that can sever actin filaments with a very high (~100%) efficiency [47] and then caps the barbed end of the filament. This leads to a decrease in the average length of the actin filaments [48]. Here, we use gelsolin to study the effect of filament length on the visco-elastic properties of the actin network.

Actin is polymerized in the presence of different concentrations of gelsolin. The length distribution of the samples was measured using tapping mode AFM (see Appendix). The number and weight-averaged filament length are plotted as a function of the molar gelsolin/actin ratio *R* in Fig. 5.8.

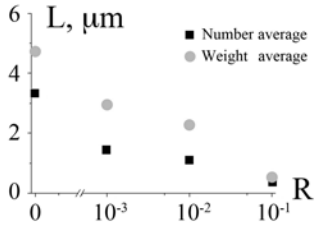

Figure 5.8. Effect of gelsolin concentration on the length of actin filaments *L*. *R* is the ratio of gelsolin to actin molar concentrations.

The actin samples with different filament length were then added to the streptavidin-coated droplets. A fixed surface concentration of streptavidin of 0.027 nm^{-2} was taken for these experiments.

We observed that with increasing amount of gelsolin, the MSD of the particles increases, as shown in Fig. 5.9. This indicates that reducing the filament length leads to a decrease in the shear modulus of the interface. At very high gelsolin concentrations (close to 1 g/L, molar gelsolin/actin ratio 0.1) the surface loses its visco-elastic properties completely and the MSD of the particles resembles that of a particle on an actin-free interface.

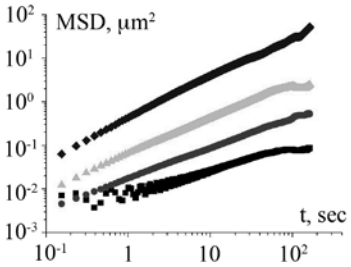

Figure 5.9. Effect of gelsolin on the MSD at different gelsolin/actin molar ratios R; R = 0 (■), R = 0.001 (●), R = 0.01 (▲), R = 0.1 (♦).

The interfacial viscosity that we find for a surface with a gelsolin/actin ratio of 0.1 is ~ 0.40 nNs/m, close to that of the surface without actin. Again we use Equation 5.3 to estimate the complex shear modulus of the surface. The results are shown in Fig. 5.10 and show the gradual transition from a visco-elastic to a viscous surface upon adding gelsolin.

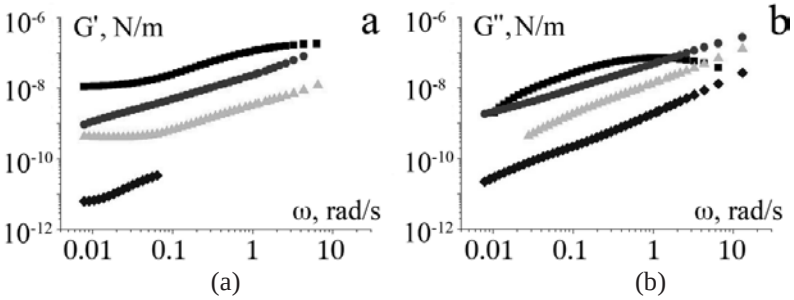

Figure 5.10. Effect of gelsolin/actin molar ratio R on the storage **(a)** and loss **(b)** moduli of the cortex; R = 0 (■), R = 0.001 (●), R = 0.01 (▲), R = 0.1 (♦); inset: the length of the filaments versus R.

The effect of gelsolin on the low-frequency storage modulus G_0 is shown in Fig. 5.11. The elasticity of the cortex decreases as the average length of the filament decreases. The reason for this is that shorter filaments have less opportunity to be cross-linked with each other. We may expect that the elastic properties are lost when the average number of biotin groups per filament is of order unity, because in that case filaments have only one anchor to the interface so that forming a cross-linked network is no longer possible.

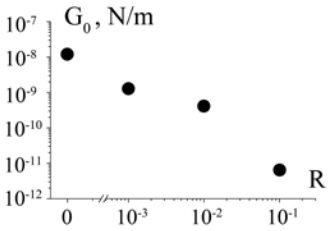

Figure 5.11. Effect of gelsolin/actin molar ratio R on the low-frequency modulus G_0 of the cortex.

As can be seen in Fig. 5.10, this happens around a gelsolin/actin ratio on the order of 0.1. According to the AFM measurements, the average filament length under these conditions is still around 400 nm, which is roughly ten times larger than the average distance between biotin groups on the filament. The reason why these layers nevertheless are almost completely viscous may be that the average length of filaments attached to the droplet is shorter than that in the bulk, because shorter filaments diffuse more rapidly.

5.3.4 Network stiffening induced by actin-myosin contraction

In animal cells, the actin cortex is stiffened actively by myosin motor proteins that generate contractile stresses in the network.

This myosin-induced contraction is utilized by cells to divide their contents into two parts during cell division process [49]. To study how myosin affects our artificial cortex layers, we mix myosin and actin in a ratio of 0.042 and then add this mixture to an emulsion of oil droplets coated with streptavidin at a density of 0.027 nm^{-2}. The resulting particle trajectories and mean square displacements are shown in Fig. 5.12a,b.

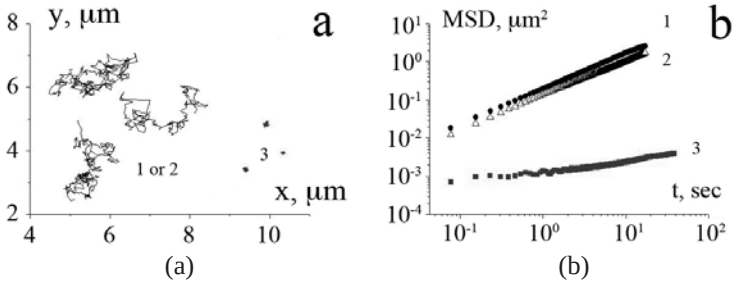

Figure 5.12. (a): Trajectories of particles in myosin-containing cortex before and after addition of ATP: no myosin (1), myosin-containing cortex with no ATP (2); myosin-containing cortex with ATP (3). **(b)**: their corresponding MSDs.

We find that the addition of myosin has no large effect on the visco-elastic properties of the networks. The MSD is slightly reduced compared to the case with the same amount of actin but no myosin. This could be due to additional cross-links formed by the myosin

filaments. Interestingly, upon adding of ATP (to a final concentration of 1.7 mM), a dramatic change was observed in the movement of the particles (Fig. 5.12a, trajectory 3) and thus, in the mechanical properties of the layer.

The particles slowed down drastically, and their motion became strongly localized, indicating that the network became more elastic. This strongly suggests an active ATP-induced contraction of the actin-myosin network around the droplets.

The values of G_0 before and after addition of ATP differ by about 400 times (1.8 nN/m and 0.75 μN/m respectively), as shown in Fig. 5.13.

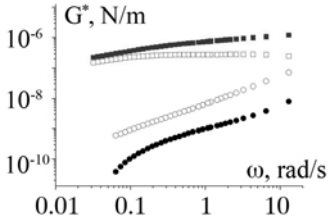

Figure 5.13. Effect of ATP addition on the complex modulus of myosin-containing cortex: storage (●) and loss (○) moduli in the absence of ATP; storage (■) and loss (□) moduli in the presence of ATP.

The actively stiffened network is even ~ 7 times stiffer than the network prepared with the highest streptavidin density (0.75 μN/m and 0.1 μN/m respectively). Similar contraction-induced stiffening was observed for actin-myosin networks in 3 dimensions, and it was ascribed to tension in the network generated by the myosin motors [15, 34].

We observed that in some cases the network became inhomogeneous. Although the MSD was roughly the same for all particles on the droplet, correlations between the movements of different particles became somewhat inhomogeneous.

5.4 Concluding remarks

In this research we have designed an artificial in-vitro model of the actin cell cortex, by linking actin filaments to the surface of an oil droplet. By adding different amounts of streptavidin and gelsolin, we varied the crosslink density of the network and the average length of the filaments. The stiffest networks, obtained for high crosslink density and relatively long filaments, had a low-frequency shear modulus of approximately 0.1 μN/m. This is slightly lower than the value of 0.5 μN/m found by Helfer et al. for actin-coated vesicles [26]. A similar value for the shear modulus of actin-coated-membranes (0.4 μN/m) was found in the study of Limozin et al [50].

When myosin and ATP are added to the actin network, very strong stiffening is observed: the shear modulus increases approximately by 2.5 orders of magnitude: from

1.8 nN/m to 0.75 μN/m. We attribute this stiffening to active tension in the network generated by actin-myosin contraction [15, 34].

The model system introduced in this paper opens up a range of opportunities to study the effect of various actin-binding proteins on the mechanics of cortical actin layers. Moreover, the use of the oil/water surface as a substrate makes it possible to use surface shear and dilatational rheometry, thus giving access also to the non-linear visco-elastic properties of the layers.

Appendix

Measurement of streptavidin density on the surface of droplets

To estimate the density of streptavidin on the surface, we proceed as follows. First, we use the adsorption of fluorescently labeled streptavidin onto solid polystyrene particles with known surface area to make a calibration plot that relates fluorescence intensity measured at the surface of a particle to the amount of adsorbed streptavidin molecules per m^2. We then use this calibration plot to estimate the density of streptavidin on the oil/water interface from the fluorescence intensity.

Samples of 20 μL with different concentrations of Alexa Fluor 633-labelled streptavidin (0.2nM, 1nM, 1.6nM, 5nM, 10nM and 100nM) were prepared. To each streptavidin solution 1 μL of washed 6 μm polystyrene particles was added (total area 13 mm^2 in each). After incubation for 2 hours at room temperature, fluorescence intensity on particles' surface was measured in the confocal microscope (at identical detector settings). For the lowest streptavidin concentrations, it was necessary to increase the laser transmission and the detector integration time. It was checked that the measured intensity increases linearly with laser transmission and integration time, so that we could normalize the intensity to correct for this.

Figure A1 shows the normalized fluorescence intensity as a function of the number of streptavidin molecules available per nm^2 of bead area. Initially, the intensity increases approximately linearly with the available streptavidin. At higher streptavidin dosages, the intensity levels off towards a plateau. We assume that the plateau corresponds to a dense monolayer of streptavidin. It is reasonable to assume that in the initial part of the curve nearly all streptavidin is bound to the particle surface. This means that the initial slope of the curve can be used to relate the fluorescence intensity to the number of streptavidin molecules on the surface per nm^2. This calibration is then used to estimate the streptavidin density on the oil droplets from the measured fluorescence intensities.

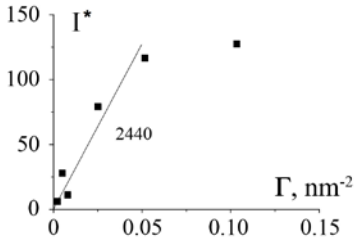

Figure A1. Normalized fluorescence intensity as a function of the amount of streptavidin per unit area.

Figure A2 shows the resulting streptavidin surface density as a function of the total concentration in the sample. The density increases linearly with increasing amount of streptavidin in the sample, which suggests that all streptavidin is bound to the interface.

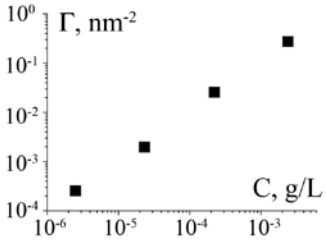

Figure A2. Streptavidin density on the oil/water interface (obtained from fluorescence intensity) as a function of the total streptavidin concentration in the sample.

The effect of gelsolin on the length of actin filaments.

Actin was polymerized as described in the Materials and methods section, with varying amounts of gelsolin. The length distribution was measured with AFM as described. Figure A3 shows a typical AFM image showing actin filaments. From these images, contour lengths were measured to obtain a length distribution. Figure A4 shows the length distribution obtained in this way for different gelsolin/actin ratios R.

Table A1 shows the weight and number-averaged length, L_W and L_N respectively for different R (also plotted in Fig. A5).

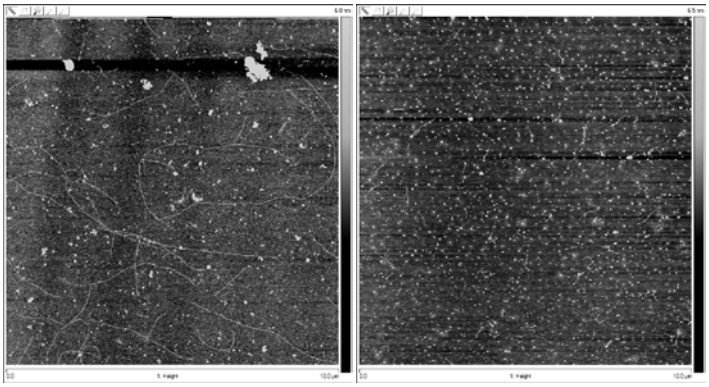

(a) (b)

Figure A3. AFM pictures of **(a)** untreated actin filaments, R = 0; **(b)** treated with gelsolin, R = 0.1 (the highest ratio studied).

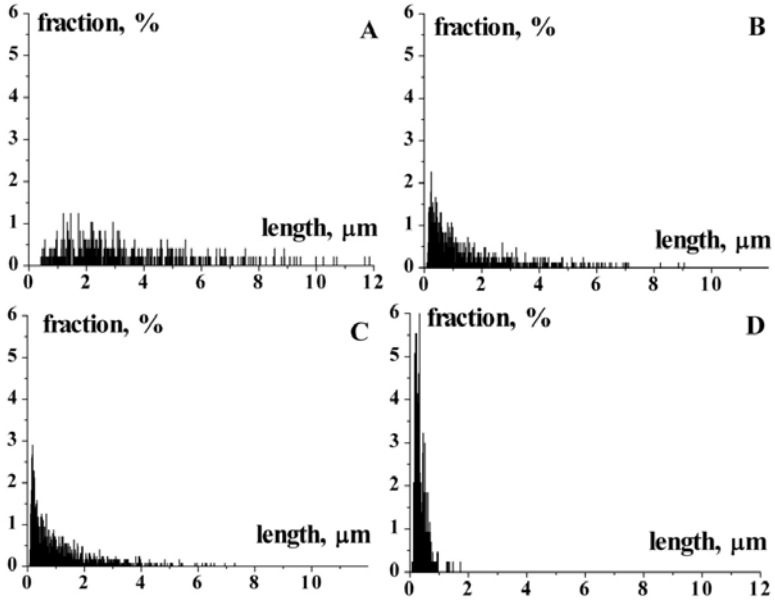

Figure A4: Effect of gelsolin on the filament length distribution, **(a)**: R=0, **(b)**: R=0.001, **(c)**: R=0.01, **(d)**: R=0.1; Horizontal axis: length; vertical axis: fraction of filaments with corresponding lengths.

R	L_W	L_N	Number of measurements
0	4.73	3.33	480
0.001	2.95	1.46	840
0.01	2.29	1.12	1270
0.1	0.50	0.37	430

Table A1. Effect of gelsolin concentration on the length of actin filaments. *R* is the ratio of gelsolin to actin molar concentrations. L_W and L_N are weight and number averaged lengths.

References

1. Diz-Munoz, A., et al., *Control of Directed Cell Migration In Vivo by Membrane-to-Cortex Attachment.* Plos Biology, 2010. **8**(11).
2. Bray, D. and J.G. White, *Cortical Flow in Animal-Cells.* Science, 1988. **239**(4842): p. 883-888.
3. Paluch, E., J. van der Gucht, and C. Sykes, *Cracking up: symmetry breaking in cellular systems.* Journal of Cell Biology, 2006. **175**(5): p. 687-692.
4. Sedzinski, J., et al., *Polar actomyosin contractility destabilizes the position of the cytokinetic furrow.* Nature, 2011. **476**(7361): p. 462-U119.
5. Heinrich, V., et al., *Elastic thickness compressibilty of the red cell membrane.* Biophysical Journal, 2001. **81**(3): p. 1452-1463.
6. Hochmuth, R.M., *Micropipette aspiration of living cells.* Journal of Biomechanics, 2000. **33**(1): p. 15-22.
7. Brugues, J., et al., *Dynamical organization of the cytoskeletal cortex probed by micropipette aspiration.* Proceedings of the National Academy of Sciences of the United States of America, 2010. **107**(35): p. 15415-15420.
8. Alcaraz, J., et al., *Microrheology of human lung epithelial cells measured by atomic force microscopy.* Biophysical Journal, 2003. **84**(3): p. 2071-2079.
9. Radmacher, M., et al., *Measuring the viscoelastic properties of human platelets with the atomic force microscope.* Biophysical Journal, 1996. **70**(1): p. 556-567.
10. Thompson, M.S. and D. Wirtz, *Sensing Cytoskeletal Mechanics by Ballistic Intracellular Nanorheology (BIN) Coupled with Cell Transfection*, in *Methods in Cell Biology*, J.C. Dr. John and D.H.W. Detrich, Editors. 2008, Academic Press. p. 467-486.
11. Tseng, Y., T.P. Kole, and D. Wirtz, *Micromechanical mapping of live cells by multiple-particle-tracking microrheology.* Biophysical Journal, 2002. **83**(6): p. 3162-3176.
12. Rogers, S.S., T.A. Waigh, and J.R. Lu, *Intracellular microrheology of motile Amoeba proteus.* Biophysical Journal, 2008. **94**(8): p. 3313-3322.
13. Yamada, S., D. Wirtz, and S.C. Kuo, *Mechanics of living cells measured by laser tracking microrheology.* Biophysical Journal, 2000. **78**(4): p. 1736-1747.
14. Gardel, M.L., et al., *Elastic Behavior of cross-linked and bundled actin networks.* Science, 2004. **304**(5675): p. 1301-1305.
15. Koenderink, G.H., et al., *An active biopolymer network controlled by molecular motors.* Proceedings of the National Academy of Sciences of the United States of America, 2009. **106**(36): p. 15192-15197.
16. Lieleg, O., et al., *Slow dynamics and internal stress relaxation in bundled cytoskeletal networks.* Nature Materials, 2011. **10**(3): p. 236-242.
17. Xu, J.Y., V. Viasnoff, and D. Wirtz, *Compliance of actin filament networks measured by particle-tracking microrheology and diffusing wave spectroscopy.* Rheologica Acta, 1998. **37**(4): p. 387-398.

18. Pelletier, V., et al., *Microrheology of Microtubule Solutions and Actin-Microtubule Composite Networks.* Physical Review Letters, 2009. **102**(18): p. 188303.
19. Humphrey, D., et al., *Active fluidization of polymer networks through molecular motors.* Nature, 2002. **416**(6879): p. 413-416.
20. Janmey, P.A., et al., *Resemblance of actin-binding protein/actin gels to covalently crosslinked networks.* Nature, 1990. **345**(6270): p. 89-92.
21. Laliberte, A. and C. Gicquaud, *Polymerization of Actin by Positively Charged Liposomes.* Journal of Cell Biology, 1988. **106**(4): p. 1221-1227.
22. Limozin, L. and E. Sackmann, *Polymorphism of cross-linked actin networks in giant vesicles.* Physical Review Letters, 2002. **89**(16).
23. Pontani, L.L., et al., *Reconstitution of an Actin Cortex Inside a Liposome.* Biophysical Journal, 2009. **96**(1): p. 192-198.
24. Tsai, F.C., B. Stuhrmann, and G.H. Koenderink, *Encapsulation of Active Cytoskeletal Protein Networks in Cell-Sized Liposomes.* Langmuir, 2011. **27**(16): p. 10061-10071.
25. Helfer, E., et al., *Microrheology of Biopolymer-Membrane Complexes.* Physical Review Letters, 2000. **85**(2): p. 457-460.
26. Helfer, E., et al., *Viscoelastic properties of actin-coated membranes.* Physical Review E, 2001. **63**(2): p. art. no.-021904.
27. Häckl, W., M. Bärmann, and E. Sackmann, *Shape Changes of Self-Assembled Actin Bilayer Composite Membranes.* Physical Review Letters, 1998. **80**(8): p. 1786-1789.
28. Claessens, M.M.A.E., et al., *Microstructure and viscoelasticity of confined semiflexible polymer networks.* Nat Phys, 2006. **2**(3): p. 186-189.
29. Haraszti, T., A.E.M. Clemen, and J.P. Spatz, *Biomimetic F-Actin Cortex Models.* Chemphyschem, 2009. **10**(16): p. 2777-2786.
30. Boatwright, T., A.J. Levine, and M. Dennin, *Mechanical reorganization of cross-linked F-actin networks at the air-buffer interface.* Soft Matter, 2011. **7**(17): p. 7851-7859.
31. Isanta, S., et al., *Active membranes with bound F-actin: sliding vs. sticking conditions.* Soft Matter, 2011. **7**(7): p. 3100-3107.
32. Renault, A., et al., *Surface-induced polymerization of actin.* Biophysical Journal, 1999. **76**(3): p. 1580-1590.
33. Walder, R., A.J. Levine, and M. Dennin, *Rheology of two-dimensional F-actin networks associated with a lipid interface.* Physical Review E, 2008. **77**(1).
34. Mizuno, D., et al., *Nonequilibrium mechanics of active cytoskeletal networks.* Science, 2007. **315**(5810): p. 370-373.
35. Brown, A.E.X., et al., *Cross-Correlated TIRF/AFM Reveals Asymmetric Distribution of Force-Generating Heads along Self-Assembled, "Synthetic" Myosin Filaments.* Biophysical Journal, 2009. **96**(5): p. 1952-1960.
36. Scholz, T. and B. Brenner, *Actin sliding on reconstituted myosin filaments containing only one myosin heavy chain isoform.* Journal of Muscle Research and Cell Motility, 2003. **24**(1): p. 77-86.

37. Kilfoil, M., *Biological Physics Lab Webpage: http://people.umass.edu/kilfoil/downloads.html.*
38. Crocker, J.C. and D.G. Grier, *Methods of digital video microscopy for colloidal studies.* Journal of Colloid and Interface Science, 1996. **179**(1): p. 298-310.
39. Saffman, P.G. and M. Delbruck, *Brownian motion in biological membranes.* Proc Natl Acad Sci U S A, 1975. **72**(8): p. 3111-3.
40. Petrov, E.P. and P. Schwille, *Translational diffusion in lipid membranes beyond the Saffman-Delbruck approximation.* Biophys J, 2008. **94**(5): p. L41-3.
41. Mason, T.G. and D.A. Weitz, *Optical Measurements of Frequency-Dependent Linear Viscoelastic Moduli of Complex Fluids.* Physical Review Letters, 1995. **74**(7): p. 1250-1253.
42. Levine, A.J. and F.C. MacKintosh, *Dynamics of viscoelastic membranes.* Physical Review E, 2002. **66**(6).
43. Mason, T.G., et al., *Particle tracking microrheology of complex fluids.* Physical Review Letters, 1997. **79**(17): p. 3282-3285.
44. Crocker, J.C., et al., *Two-point microrheology of inhomogeneous soft materials.* Physical Review Letters, 2000. **85**(4): p. 888-891.
45. Prasad, V., S.A. Koehler, and E.R. Weeks, *Two-particle microrheology of quasi-2D viscous systems.* Physical Review Letters, 2006. **97**(17).
46. Head, D.A., A.J. Levine, and F.C. MacKintosh, *Distinct regimes of elastic response and deformation modes of cross-linked cytoskeletal and semiflexible polymer networks.* Physical Review E, 2003. **68**(6).
47. Selden, L.A., et al., *Severing of F-Actin by the amino-terminal half of gelsolin suggests internal cooperativity in gelsolin.* Biophysical Journal, 1998. **75**(6): p. 3092-3100.
48. Janmey, P.A., et al., *Structure and mobility of actin filaments as measured by quasielastic light scattering, viscometry, and electron microscopy.* Journal of Biological Chemistry, 1986. **261**(18): p. 8357-62.
49. Dean, S.O. and J.A. Spudich, *Rho Kinase's Role in Myosin Recruitment to the Equatorial Cortex of Mitotic Drosophila S2 Cells Is for Myosin Regulatory Light Chain Phosphorylation.* Plos One, 2006. **1**(2).
50. Limozin, L., A. Roth, and E. Sackmann, *Microviscoelastic moduli of biomimetic cell envelopes.* Physical Review Letters, 2005. **95**(17).

CHAPTER 6

SUMMARY AND GENERAL DISCUSSION

6.1 Summary

This thesis deals with spherical microparticles trapped at liquid interfaces. It focuses on two aspects of their behavior: firstly, the effect of the curvature of a liquid interface on interparticle interactions and their organization; secondly, the mobility of particles at visco-elastic interfaces.

In **Chapter 2** of this thesis we showed that it is possible to induce capillary interactions between spherical microparticles with homogeneous surface chemistry by tailoring the curvature of the liquid interface. If the interfacial curvature is anisotropic, the constraint of constant contact angle along the contact line can only be satisfied if the interface is deformed locally. These deformations create excess surface area, which changes when two particles approach each other. This leads to a change in the surface free energy, which manifests itself as a capillary interaction between the particles.

To study the effect of curvature on the interactions between particles, we created oil-water interfaces of different shape (ellipsoid, dumbbell, torus and squares) and added spherical negatively charged particles that adsorbed at these interfaces. On all these interfaces, we observed quadrupolar capillary interactions that organized the particles into square lattices. The order of this organization increased with increasing curvature anisotropy, indicating that capillary interactions are stronger as well. By contrast, on flat interfaces or on spherical droplets with homogeneous curvature, no attractive interaction was observed and only at very high surface coverage did the particles order in a hexagonal lattice, as a result of repulsive interactions.

In **Chapter 3** we studied the interface deformations around particles at curved interfaces and the resulting capillary interactions theoretically. We used the finite element method to solve the Young-Laplace equation for the shape of the interface around a particle and calculated the interaction potential between the particles numerically.

The main finding of these calculations is that for an anisotropically curved interface, with two different local principal curvatures, the particle deforms the interface in two ways simultaneously: concave deformation along one principal direction and convex – along the other, thus creating a deformation field with quadrupolar symmetry. Two particles with such deformations interact favorably only if the overlapping deformations are similar (concave-concave, convex-convex), which occurs when they approach each other along one of the two principal directions. Since the two local principal directions are always perpendicular, particles interacting along them will tend to arrange into a square pattern.

As a consequence of the quadrupolar deformation field, two particles approaching each other along a line forming 45 degrees with the principal axes will repel each other (which is confirmed by our observations), because in this case the deformation fields overlap with four different “petals” (2 pairs of concave-convex), and the excessive surface area doesn’t reduce upon approaching, but increases. A system of two particles oriented at an angle with respect to the principal axis is therefore subjected to a torque rotating the axis of the system so that it gets aligned with one of the two principal directions. The torque magnitude reaches its maximum when the system’s axis is at an angle of 45 degrees with respect to the

principal direction and decreases to 0 when the axis is aligned with one of the principal directions.

The family of interaction potentials we obtained allows for calculating the minimum deviatoric curvature needed to initialize capillary interactions strong enough to compete with thermal energy, so that a stable organization can be expected. The calculated value was very close to the deviatoric curvature where ordering was observed experimentally in Chapter 2.

In **Chapter 4** we studied the mobility of 3 μm polystyrene particles in a monolayer of 1.5 μm core-shell microparticles deposited at flat air-water interfaces; all the particles present in the system were stabilized by negative charges.

In this exploratory chapter we made an attempt to characterize the mechanical properties of such monolayers by analyzing the mobility of the larger tracer particles in the monolayer. With increasing particle density of the monolayer, we observed that the mean-square displacement of the tracer particles was reduced, which can be interpreted as an increase of the viscosity of the monolayer. At very high densities the motion of the particles became subdiffusive and confined, pointing at elasticity of the monolayer. We also studied correlated movements between neighboring particles in an attempt to do two-point interfacial microrheology. A comparison between the one-point and two-point methods shows clear indications of heterogeneous dynamics of the tracer particles. Our results therefore call for a further development of two-point microrheology at interfaces.

In **Chapter 5** we used tracer particles to study the properties of thin cross-linked actin networks deposited at the surface of oil droplets. These networks are a model system for the intracellular actin cortex. We used the generalized Stokes-Einstein relation to extract the complex frequency-dependent shear modulus of such networks from the movement of the added tracer particles. We studied the effects of the length of actin filaments and the cross-linker concentration on the mechanical properties of these layers.

The advantage of this system is that actin networks are freely accessible from the water phase, and therefore can be subjected to in-situ addition of cross-linkers, enzymes or other chemicals of interest. Using this, we managed to show strong stiffening after addition of myosin motor proteins and ATP, which we ascribed to contraction of the actin-myosin network.

6.2 General discussion

6.2.1 Colloidal self-assembly

Colloidal self-assembly is used in many applications such as drug delivery [1, 2], cosmetics [3], food industry [4, 5], in photonics [6] and microelectronics.

In particular the latter two applications rely on our ability to manufacture well-defined structures in the micro and nanometer range with good precision. For 2-dimensional structures this can be achieved by using an interface to direct the self-assembly process [7].

The possibility of using a layer of colloidal particles deposited in either random or ordered arrays at the surface of a substrate as an etching or deposition mask was first described in [8]. In this work, the authors manufactured identical submicron columnar structures, by utilizing the ability of colloids to self-organize under suitable conditions at a liquid interface into arrays of hexagonally ordered particles. After drying on a solid substrate, the particles and the openings between them form a mask, under which the substrate can be modified selectively by erosion or by adding thin-film deposition.

Strategies for the fabrication of new structural motifs have been investigated actively since then [9, 10]; after years of development this technique is now capable of producing nanocircuits by utilizing double layer masks composed of ordered nanoparticles [11], Fig. 6.1.

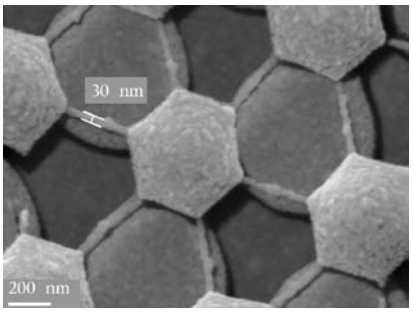

Figure 6.1. SEM image of a plasma treated NSL double layer mask made of 1000 nm diameter PS spheres. Adopted from [11].

The quality of the fabricated structures depends on the quality of the particle masks. Therefore, understanding and controlling each step of their preparation is essential. To achieve control over the final lattice geometry of particle layers, it is crucial that the direction and strength of particle interactions can be controlled precisely. This requires a good understanding of all the different kinds of interactions that can arise between colloids at an interface

In the case when hard repulsive interactions dominate [12], the resulting structures are determined mainly by packing constraints. Typically, for monodisperse particles this leads to hexagonal particle arrays, since this correspond to the most efficient packing in two dimensions. More complex patterns can be obtained for bidisperse suspensions of particles. By carefully choosing the size ratio between the two kinds of particles, regular lattices can be obtained in which the small particles occupy the gaps between the closely packed larger particles [7].

To obtain other lattice symmetries, *directional* interactions between the colloidal particles are needed. While previously, this has been achieved by using particles with an anisometric shape [13], or with asymmetric surface properties [14, 15], or by employing external fields [16-18], in Chapter 2 we have shown that anisotropic interactions can also be induced between homogeneous spherical particles.

By using anisotropically curved interfaces, we have shown that quadrupolar capillary interactions can be induced between the particles, which drive organization of the particles into square lattices. This could potentially find use in the fabrication of circuits in microelectronics as a new structural element that has not been introduced so far. To achieve this, however, it is crucial to have a better control over the self-organization of particles at curved interfaces. This requires both optimization of the experimental conditions and a better understanding of the particle interactions and dynamics.

6.2.2 Producing flat interfaces

Before interface curvature can be used as a means to induce interactions between particles, it is of crucial importance that interfaces with well-defined curvature can be produced. The reverse is also true, however: if capillary interactions between particles at a liquid interface must be avoided, it is of crucial importance to be able to produce perfectly flat interfaces. This is not as straightforward as it may seem at first sight, because the interactions with the container walls or with other solid surfaces produce curved liquid menisci. These menisci perturb the liquid interface over a distance of approximately $l_c \approx \sqrt{\gamma/\rho g}$ (the capillary length), which is ~2.7 millimeters for the air-water interface. For a cylindrical container with a diameter of 3 cm this capillary length gives $D = 3 \cdot 10^{-4}$ μm^{-1}. As we have seen in Chapter 2, a deviatoric curvature of this magnitude is insufficient to produce significant capillary interactions between micron-sized colloids, but for larger particles it might cause interactions.

In Chapter 2, we have used flat interfaces as a negative control, to make sure that the interactions that we observed are indeed due to a curvature effect. Using large areas (much larger than the capillary length) turned out to be difficult, because convective flows or interface vibrations made it impossible to track the particles. We therefore decided to work with smaller areas. To avoid curvature effects due to the meniscus at these interfaces, it is important that the interface edge is pinned at 90 degrees to the walls of the vessel. This can in principle be achieved using micro-wells, provided that exactly the right amount of liquid is placed in the wells, in order not to create concave or convex interfaces. One very crucial issue should be recognized: the edges of the well have to be smooth and straight, otherwise they induce unwanted “rays” of curvatures, as shown in Fig. 6.2. Random directions of these “rays” effectively induce interactions that may be recognized as isotropic attractive. This information might be of use in shedding some light on the mystery of attraction between like-charged particles at seemingly flat interfaces [19-21].

Improving the quality of the wells’ edges is important for future work in this direction. It is possible to achieve this by tuning the parameters of the soft lithography process, during which the wells are formed. The quality of the edges (their sharpness) responds rather sensitively to the temperature and time of the soft baking step and to the thickness of the photoresist layer.

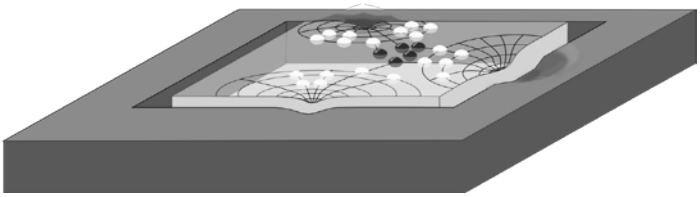

Figure 6.2. Random curvature "rays" emanating from dents on the edge of the substrate. In the place where they interact, the particles may form irregular clusters.

In an alternative approach, we have attempted to trap a smaller volume of water in a small torus-shaped O-ring, as shown in Fig. 6.3. First we placed a rubber O-ring on the air-water surface. For a heavy O-ring, the interface is deformed as shown in Fig. 6.3a, creating a 'capillary monopole'. If the O-ring is light, however, so that its Bond number is small, no monopole is created. The axial symmetry of the O-ring, whose cross section is a circle, implies that the contact angle can be satisfied everywhere without deformation of the interface (provided that the ring has a smooth surface). Hence, for light and smooth O-rings floating at the interface, no deformation of the interface occurs (Fig. 6.3b).

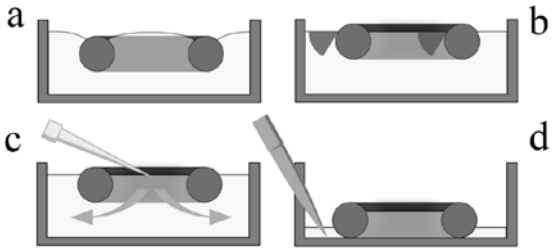

Figure 6.3. **(a)**: A heavy floating O-ring deforming a liquid interface. **(b)**: A light O-ring with smooth surface doesn't deform the interface. **(c)**: Deposition of compound of interest onto the "secured" part of the interface; **(d)**: removal of the bulk water. The steps **c-d** can be repeated many times.

The rubber band that we used was 0.125 g, its outer radius was 12 mm, and its inner radius was 8 mm; for the O-ring immersed in water to ¾ of its height the Bond number was estimated to be about 0.1; it seems possible to reduce the Bond number even more by reducing the mass and volume of the torus. Although the surface of the O-ring was not entirely smooth, with some effort it was possible to make the contact line pinned rather uniformly, which gave an interface with unnoticeable curvature defects.

After this, one can deposit any compound of interest at the interface secured by the O-ring, Fig. 6.3c. For depositing microparticles they are typically suspended in ethanol and spread over the interface; ethanol then evaporates and seeps into water, leaving particles attached to the interface. In small volumes of water this causes flows that persist for a long time (as observed with microscopy), but in a larger volume of water ethanol dissipates much quicker, as schematically indicated with arrows in Fig. 6.3c. After the flows have disappeared, one can remove the bulk of water to settle the torus on the bottom of the

vessel; this traps a small volume of water that still has a flat interface. Reduction of the bulk of water leads to significantly reduced flows and remarkably improves the stability of the interface.

The advantage of this approach is that it is very easy to add compounds suspended in volatile solvent in a controlled manner: the compound doesn't dilute over the entire interface and is secured within the region confined by the O-ring. Another useful feature is that one can change the composition of the bulk phase by adding, e.g., salt or acid or other chemicals of interest to the water bulk outside the O-ring without disturbing the area secured within the ring. One way to produce light and smooth O-rings is by using a 3D printer; 3D printers with a precision ranging from 16 to 200 microns are available at relatively low cost.

6.2.3 Producing interfaces with adjustable curvature

During our experiments with microparticles at curved oil-water interfaces we observed an interesting phenomenon: at high particle surface density, the organization could be switched from a hexagonal to a square lattice by increasing the curvature of the oil-water interface. To study the dynamics of such transitions, it is necessary to be able to produce interfaces, whose shape can be adjusted in situ.

In a first attempt to make such an adjustable interface, we developed micro-wells that were connected to a larger reservoir. This allows for pumping more liquid inside the micro-wells by pushing on the large reservoir; doing so we deliver additional volume into the wells and thus change the curvature of the interface (since the contact line remains pinned to the edge of the wells). Preliminary experiments indicated that this could indeed be used to induce transitions from a hexagonal to a square lattice organization.

This experiment can be improved further, if the volume of liquid pumped into micro-wells could be controlled. This can be done utilizing multilayer soft lithography, as shown in Fig. 6.4. The bottom layer contains a channel for pumping the liquid in/out (red arrow), while the upper layer contains a shape to which the liquid interface contact line will be pinned. In this way one can control curvatures of the interface by adding or removing well-defined volumes of the liquid. Additionally, this setup can be used to have more control over the process of making flat interfaces, as discussed above in the Section 6.2.2.

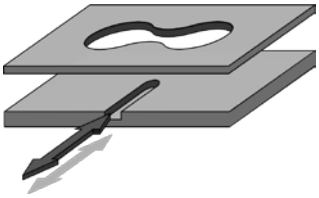

Figure 6.4. Multilayered soft lithography. The lower layer contains a channel-inlet for liquid; the upper layer contains a shape to which the liquid is going to be pinned.

6.2.4 Other symmetries?

The interfaces that were studied in this thesis (cylinder, catenoid as the neck of a dumbbell, ellipsoid, and others) all had quadrupolar symmetry, leading to square lattice organizations (Fig. 6.5a). The question then rises whether it is possible to create interfaces with different symmetry, for instance, a “hexapolar” surface, which would induce hexapolar deformations around particles? One would imagine, that the surface, curved as in Fig. 6.5b would do this, but this is only true for particles situated in the center of the hexapole. In any other region, the local symmetry is quadrupolar (being described by two principal curvature directions), so square patterns are to be expected based on our findings of Chapter 3. It should be noted, however, that the calculations in this chapter were performed for cases when the curvature can be assumed to be constant on the scale of the particle size. Different organizations may be expected when the length scale at which the curvature varies is of the same order as the particle size.

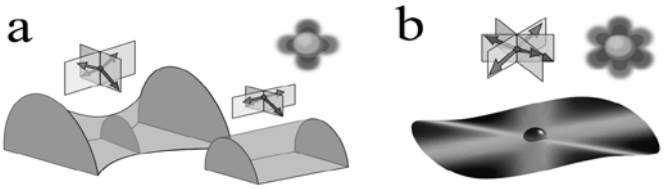

Figure 6.5 Quadrupolar deformation induced by particles deposited at “quadrupolar” interfaces (a). Hexapolar deformation induced by a particle deposited at the center of “hexapolar” interface.

6.2.5 Control over particle properties

Next to the curvature of the liquid interface, also the properties of the particles play an important role in determining the nature of the capillary interactions. Particles with a rough surface can curve the interface around them due to contact line pinning at irregularities on the particle surface. This results in a poorly controlled deformation field. As reported in [22], the quadrupolar deformation mode is expected to dominate at large distances from the particle surface (for 0.5 μm particles the interaction energy decays to 1 kT at a separation of 15 μm). Hence, even irregular deformations of the contact line can effectively give rise to quadrupolar interactions in the far field. However, because the meniscus is different for each particle, there is a broad heterogeneity in the interparticle forces. Therefore the tendency towards the formation of linear aggregates [22] instead of square patterns can be reasoned with the frustration of multiparticle interactions caused by inadequate relative orientations. Also, at smaller separations, other modes (of higher orders) become important. As a result, a regular square pattern is not observed experimentally for particles with irregular contact line.

If a particle has an asymmetric (or patchy) charge distribution, then it can effectively behave as a dipole, either “vertical” (perpendicular to the plane of the interface), or in plane, as shown in Fig. 6.6. The vertical dipoles pointing in the same direction repel each other, thus inducing a long-ranged interparticle repulsive interaction analogous to [12]. By contrast, in-plane dipoles can rotate and rearrange end-to-end, thus inducing an attractive interaction [23]. These interactions due to charge “patchiness” are often unwanted, and for precise measurements this should be taken into account; this problem is also inherent to commercially available particles, as reported in [23].

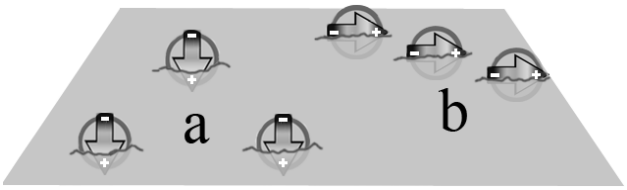

Figure 6.6. Dipoles that may occur if a particle is unevenly charged. **(a)**: “Vertical” dipoles would lead to repulsive dipole-dipole interaction. **(b)**: “Horizontal” dipoles lead to attractive dipole-dipole interaction.

Clearly, the properties of the particles, in particular the surface roughness and charge distribution must be taken into account when studying their interactions at interfaces.

6.2.6 Responsive particles

In Section 6.2.3 we described that curving a liquid interface *in-situ* can induce a transition from one kind of organization to another. An alternative possible way to achieve this is by using particles that change their surface properties upon a change in the environmental conditions. We know now that the effect of curved interfaces is a result of the condition of constant contact angle along the contact line; so can we create a particle, the contact line of which would depend on environmental conditions?

In Chapter 1 we have discussed a dumbbell-shaped particle and the peculiarities of its contact line at a liquid interface. When the contact angle of such a dumbbell-shaped particle is exactly 90 degrees, there will be no deformations of the interface (Fig. 6.7a), and therefore no capillary interaction between the particles. If one now changes a relevant parameter in one of the phases (such as pH, ionic strength, or surfactant concentration), a change in contact angle may result as, for instance, in [24].

Suppose that the particle gets more hydrophilic and submerges deeper into the water, Fig. 6.7b. The contact angle will not be constant along the whole contact line anymore (Fig. 6.7b: yellow and red angles are not equal) and in order to make it so, the particle has to deform the interface (Fig. 6.7c: two angles are now equal). This kind of deformation will induce a surface tension force with a vertical component pulling the particle downwards,

and this will create a weak depression around the spherical parts of the dumbbell, as shown in Fig. 6.7d. Thus in equilibrium the particle will have a quadrupolar deformation around itself, which will cause attractive capillary interactions, Fig. 6.7d.

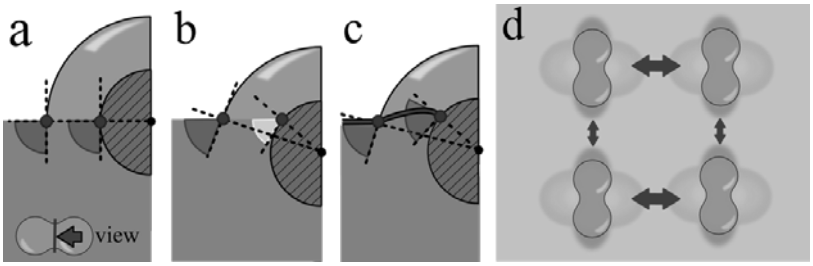

Figure 6.7. (a): A dumbbell-shaped particle at a flat liquid interface with a contact angle of 90 degrees. **(b)**: The particle has submerged deeper into water; the contact angle is not constant. **(c)**: The interface deforms to equalize the contact angle. **(d)**: Capillary interactions between particles with such deformations.

In Fig. 6.8 one can see dumbbells deposited at a flat air-water interface. Many of the particles are aligned with their major axes parallel to each other (either side-by-side or end-to-end, data not shown), which confirms our reasoning above. This experiment can be improved further by tuning the contact angle of the particles so that the deformations become stronger and therefore the organization similar to that in Fig. 6.7d is more pronounced.

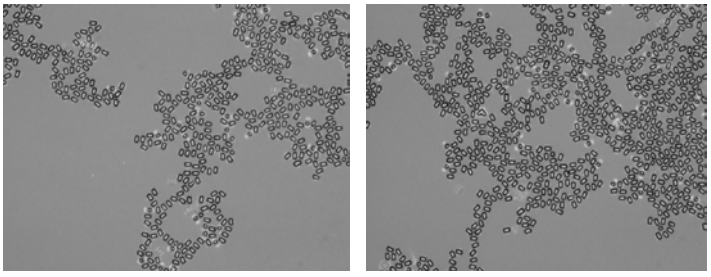

Figure 6.8. Interactions between dumbbell-shaped particles (1 micrometer) at a flat air-water interface. The major axes of the particles are mainly parallel (end-to-end or side-by-side). (Pictures: courtesy of Christian Buchcic).

6.2.7 Measurement of capillary interactions and manipulating the lattices

In Chapter 3 we have made theoretical predictions for the interaction potential between two particles at a curved liquid interface. It would be interesting to compare these

predictions directly to experimental data. This would require a direct measurement of the interaction forces acting between two particles trapped at a curved liquid interface

An elegant method of characterizing interparticle forces was developed by Loudet et. al. for ellipsoids at an oil-water interface [25]. Their approach is based on following the trajectories of moving particles approaching each other and then calculating the interaction energy by equating the work done by capillarity and viscous dissipation in the fluid.

An alternative method to measure interaction forces is to use optical tweezers. Microparticles are trapped in a harmonic potential well created by a focused laser beam; by steering the beam, particles can be manipulated. The force on the particle can be measured at the same time by monitoring the displacement away from the center of the trap. This technique has been successfully implemented in similar systems [26-28].

It is also interesting to use the optical tweezers to introduce defects in square lattices. This can be done, for example, by adding an extra particle, by removing one particle from the lattice, or by moving particles around in the lattice. Alternatively, one could study particle mixtures, in which some of the particles are replaced with another type, for instance with a higher surface charge density or with a different size.

Although this method has the advantage of being able to directly manipulate the beads, it is probably more difficult to apply than the trajectory-based method. For example, in order to be able to trap and manipulate the particles, they have to possess suitable optical properties; artifacts can be introduced around the focal spot of the trapping beam, which might introduce local curving of the interface [29-31].

6.2.8 Application

When full control over the directional (anisotropic) interactions and therefore of the assembly process has been gained, the square lattices can find their use as a new structural element in a number of applied fields: photonics, microelectronics, soft lithography.

However, for many of these applications, it is necessary to transfer the particle arrays onto a solid substrate. Some of the most used techniques for deposition of microparticles onto a solid substrate are sessile drop evaporation, patterned deposition at moving contact lines, Langmuir-Blodget and methods. They all involve deformation of the liquid interface during the process of deposition (evaporation or additional contacts with the interface), which can disturb particle organization.

This suggests that the particles should be frozen into the interface prior to direct contact with the substrate, so that their organization is not disturbed. This can be done by trapping the particles at an interface formed with temperature-responsive material such as paraffin instead of oil.

6.2.9 Interfacial microrheology

In the second part of this thesis, we have studied the mobility of particles trapped at a liquid interface. The particle mobility was used to extract information about the visco-elastic properties of the interface, by assuming a generalized Stokes-Einstein relation [32]. The applicability of Stokes-Einstein relation to particles at liquid interfaces was shown to hold true in [33]. Although valuable information about the interface can indeed be obtained using this approach, care should be taken both in the choice of the experimental system and in the interpretation of the data.

First of all, one should be very careful with choosing the tracer particles. For example, the presence of charge on the particles can initiate long-ranged dipole-dipole repulsion (for out-of-plane dipoles, [12]) or attraction (for in-plane dipoles, [23]) between the particles. Likewise, as discussed above, surface roughness [22] or curvature of the liquid interface (for example due to menisci) can lead to long-ranged capillary interactions between particles (Chapter 2). Obviously, the presence of such long-ranged interactions has a significant effect on the mobility of the tracer particles, which can be erroneously interpreted in terms of visco-elastic properties of the studied medium.

For 1-point microrheology, heterogeneities in a medium and interactions between tracers and the medium lead to erroneous results too; the values of the complex shear moduli are significantly lower as compared to macrorheology measurements. For bulk measurements this issue has been successfully solved with 2-point microrheology. However, usage of this method for interfacial measurements should be conducted with care.

The flow fields around the tracers are different in the presence of an interface, and may add additional coupling between particle movements and affect their cross-correlated motion [34]. For homogeneous, viscous surfaces, these effects have been addressed successfully by Prasad et al. [35]. However, a method that can be applied to both viscous and elastic interfaces has not yet been fully developed.

The work of Levine & Mackintosh [34] provides a framework within which new experiments can be done to improve understanding of interfacial phenomena in the context of 2-point microrheology. In their study they derived the connection between the complex shear modulus and dilatational modulus to the 2-point microrheology measurements. Their approach can be tested by combining three respective measurement techniques (interfacial shear and dilatational rheology and microrheology) and applying them to the same sample interface.

6.2.10 Studying of thin actin networks

In Chapter 5, we developed a model system for the actin cortex of biological cells, in which actin filaments were attached to an oil/water interface. The advantage of this model is that it gives easy access to the actin filaments from the water phase. The effect of regulating factors, such as cross-linkers or motor proteins can be studied conveniently by

changing their concentration in the water phase. To use the full advantage of this, it would be interesting to deposit such actin-covered oil droplets inside micro chambers, which have several micro channel inlets and outlets. This would allow delivery of chemicals of interest directly to the actin network so that their effect can be studied more precisely.

In our experiments on actin-myosin networks at the oil/water interface, we observed very strong stiffening upon adding ATP, which we ascribed to active contractions. It would be interesting to measure the stress that such an active network exerts on the substrate. One possible way to do this is to attach an actin/myosin network to the surface of a microgel particle (for example by using electrostatic interactions). Contraction of the network after ATP addition would squeeze the microgel particle. If the elastic modulus of the microgel particle is known (this can be measured separately and varied by changing the crosslink density), the stress exerted by the network can be obtained from the deformation of the particles.

6.2.11 Artificial muscles?

In a side project, we have studied another way of attaching actin filaments to a surface. Solid silica substrates were chemically modified for further attachment of proteins to it. Actin was used to test whether the modification was successful. After it was proven that the actin monomers were covalently linked to the substrate, we tried to initiate growth of actin filaments from them by adding more actin monomers and F-buffer.

An interesting phenomenon was observed when the sample was left for one night to polymerize. If the surface density of the covalently attached monomers was high, we could see that growing filaments organized into bundles (Fig. 6.9). The mechanism of such organization is most probably based on spatial confinement of the actin filaments and their aligning along each other, as observed for microtubules.

In principle, the quality of such bundles can be controlled on molecular and global levels. Microfluidics can be utilized to govern the alignment of bundles in a desired direction globally [36, 37] and using nucleation promoting factors (as, for example, protein pWA in [37]) along with various cross-linkers, the density of the bundles can be controlled.

A further step would be growing well-organized bundles in the presence of myosin filaments and studying contractile forces of such systems. Apparently, they would be able to generate strong forces due to unidirectional organization of the bundles, contrast to disordered gel-like actin-myosin systems [38, 39].

Figure 6.9. Actin bundles, grown from actin monomers covalently linked to silica substrate.

References

1. Weers, J.G., *Colloidal particles in drug delivery.* Current Opinion in Colloid & Interface Science, 1998. **3**(5): p. 540-544.
2. Dinsmore, A.D., et al., *Colloidosomes: Selectively permeable capsules composed of colloidal particles.* Science, 2002. **298**(5595): p. 1006-1009.
3. Tadros, T.F., *Colloids in Cosmetics and Personal Care*. 2008: Wiley.
4. Patel, A., *Novel colloidal structures from food-grade materials for applications in functional foods*, in *InsideFood symposium : book of proceedings*. 2013, KU Leuven.
5. Luo, Y., *Development of food polymer-based colloidal delivery systems for nutraceuticals*, in *Food Science*. 2012, University of Maryland.
6. Romanov, S.G., et al., *Probing guided modes in a monolayer colloidal crystal on a flat metal film.* Physical Review B, 2012. **86**(19).
7. Vogel, N., et al., *Wafer-Scale Fabrication of Ordered Binary Colloidal Monolayers with Adjustable Stoichiometries.* Advanced Functional Materials, 2011. **21**(16): p. 3064-3073.
8. Deckman, H.W. and J.H. Dunsmuir, *Natural lithography.* Applied Physics Letters, 1982. **41**(4): p. 377-379.
9. Haynes, C.L. and R.P. Van Duyne, *Nanosphere lithography: A versatile nanofabrication tool for studies of size-dependent nanoparticle optics.* Journal of Physical Chemistry B, 2001. **105**(24): p. 5599-5611.
10. Zhang, X.Y., et al., *Advances in contemporary nanosphere lithographic techniques.* Journal of Nanoscience and Nanotechnology, 2006. **6**(7): p. 1920-1934.
11. Gogel, D., et al., *Plasma modification of nanosphere lithography masks made of polystyrene beads.* Journal of Optoelectronics and Advanced Materials, 2010. **12**(3): p. 740-744.
12. Pieranski, P., *Two-Dimensional Interfacial Colloidal Crystals.* Physical Review Letters, 1980. **45**(7): p. 569-572.

13. Botto, L., et al., *Capillary interactions between anisotropic particles.* Soft Matter, 2012. **8**(39): p. 9957-9971.
14. Park, B.J., T. Brugarolas, and D. Lee, *Janus particles at an oil-water interface.* Soft Matter, 2011. **7**(14): p. 6413-6417.
15. Rezvantalab, H. and S. Shojaei-Zadeh, *Capillary interactions between spherical Janus particles at liquid-fluid interfaces.* Soft Matter, 2013. **9**(13): p. 3640-3650.
16. Velev, O.D. and K.H. Bhatt, *On-chip micromanipulation and assembly of colloidal particles by electric fields.* Soft Matter, 2006. **2**(9): p. 738-750.
17. Dommersnes, P., et al., *Active structuring of colloidal armour on liquid drops.* Nature Communications, 2013. **4**.
18. Dillmann, P., G. Maret, and P. Keim, *Polycrystalline solidification in a quenched 2D colloidal system.* Journal of Physics-Condensed Matter, 2008. **20**(40).
19. Nikolaides, M.G., et al., *Electric-field-induced capillary attraction between like-charged particles at liquid interfaces.* Nature, 2002. **420**(6913): p. 299-301.
20. Megens, M. and J. Aizenberg, *Like-charged particles at liquid interfaces.* Nature, 2003. **424**(6952): p. 1014-1014.
21. Nikolaides, M.G., et al., *Like-charged particles at liquid interfaces - Reply.* Nature, 2003. **424**(6952): p. 1014-1014.
22. Stamou, D., C. Duschl, and D. Johannsmann, *Long-range attraction between colloidal spheres at the air-water interface: The consequence of an irregular meniscus.* Physical Review E, 2000. **62**(4): p. 5263-5272.
23. Chen, W., et al., *Long-ranged attraction between charged polystyrene spheres at aqueous interfaces.* Physical Review Letters, 2005. **95**(21).
24. Yan, N. and J.H. Masliyah, *Effect of pH on Adsorption and Desorption of Clay Particles at Oil–Water Interface.* Journal of Colloid and Interface Science, 1996. **181**(1): p. 20-27.
25. Loudet, J.C., et al., *Capillary Interactions Between Anisotropic Colloidal Particles.* Physical Review Letters, 2005. **94**(1): p. 018301.
26. Di Leonardo, R., F. Saglimbeni, and G. Ruocco, *Very-long-range nature of capillary interactions in liquid films.* Physical Review Letters, 2008. **100**(10).
27. Wang, G.M., R. Prabhakar, and E.M. Sevick, *Hydrodynamic Mobility of an Optically Trapped Colloidal Particle near Fluid-Fluid Interfaces.* Physical Review Letters, 2009. **103**(24): p. 248303.
28. Jesacher, A., et al., *Holographic optical tweezers for object manipulations at an air-liquid surface.* Optics Express, 2006. **14**(13): p. 6342-6352.
29. Emile, O. and J. Emile, *Low-Power Laser Deformation of an Air-Liquid Interface.* Physical Review Letters, 2011. **106**(18): p. 183904.
30. Delville, J.P., *Optical Deformability of Fluid Interfaces*. 2009: Nova Science Publishers, Incorporated.
31. Verma, G., et al. *Can low power laser induce dimple on air-water interface?* in *CLEO: 2013*. 2013. San Jose, California: Optical Society of America.

32. Mason, T.G. and D.A. Weitz, *Optical Measurements of Frequency-Dependent Linear Viscoelastic Moduli of Complex Fluids.* Physical Review Letters, 1995. **74**(7): p. 1250-1253.
33. Song, Y., M. Luo, and L.L. Dai, *Understanding Nanoparticle Diffusion and Exploring Interfacial Nanorheology using Molecular Dynamics Simulations.* Langmuir, 2009. **26**(1): p. 5-9.
34. Levine, A.J. and F.C. MacKintosh, *Dynamics of viscoelastic membranes.* Physical Review E, 2002. 66(6).
35. Prasad, V., S.A. Koehler, and E.R. Weeks, Two-particle microrheology of quasi-2D viscous systems. Physical Review Letters, 2006. 97(17)
36. Bouxsein, N.F., et al., *Alignment of filamentous proteins and associated molecules through confinement in microchannels.* Applied Physics Letters, 2004. **85**(23): p. 5775-5777.
37. Reymann, A.C., et al., *Nucleation geometry governs ordered actin networks structures.* Nature Materials, 2010. **9**(10): p. 827-832.
38. Koenderink, G.H., et al., *An active biopolymer network controlled by molecular motors.* Proceedings of the National Academy of Sciences of the United States of America, 2009. **106**(36): p. 15192-15197.
39. Bendix, P.M., et al., *A quantitative analysis of contractility in active cytoskeletal protein networks.* Biophysical Journal, 2008. **94**(8): p. 3126-3136.

SAMENVATTING

In dit proefschrift is het gedrag bestudeerd van bolvormige microdeeltjes gevangen op vloeistof- vloeistof grensvlakken. De focus van dit gedrag ligt allereerst, op het effect van de kromming op vloeistof-vloeistof grensvlakken, en, ten tweede, op de mobiliteit van deeltjes op visco-elastische grensvlakken.

In **hoofdstuk 2** van deze thesis demonstreren wij de mogelijkheid tot het induceren van capillaire interacties tussen bolvormige microdeeltjes met homogene oppervlaktechemie. Dit wordt bereikt door het instellen van een geschikte kromming van het vloeistof-vloeistof grensvlak. In het geval dat de kromming van het grensvlak anisotroop is, kan de randhoek alleen constant zijn langs de contactlijn als het grensvlak lokaal wordt gedeformeerd. Deze deformaties zullen resulteren in extra oppervlakte. Wanneer de deeltjes elkaar naderen verandert dit extra oppervlak. De wijziging van de vrije energie op het oppervlak, komt aldus direct tot uiting in de capillaire interactie tussen microdeeltjes.

Met het doel het effect van kromming op de interacties tussen deeltjes te bestuderen, creëerden wij een olie-water grensvlakken van verschillende vormen (o.a. ellipsoïde, halter, torus en vierkanten). Hieraan voegde wij vervolgens bolvormige negatief geladen deeltjes toe die adsorbeerden aan deze ontworpen grensvlakken. Op al deze grensvlakken namen we quadrupolaire capillaire interacties waar die tot gevolg hadden dat de microdeeltjes zich organiseerden in een vierkante rooster structuur. De mate van organisatie bleek vervolgens toe te nemen met de stijging van de anisotrope kromming, wat sterkere capillaire interacties impliceert. Dit in tegenstelling tot platte grensvlakken of bolvormige druppels met homogene kromming, waar geen aantrekkende interacties werden waargenomen. Bovendien werd alleen bij zeer hoge bezetting van deze deeltjes aan het oppervlak, ten gevolge van repulsieve interacties, een ordening van deze deeltjes in een hexagonale ruitstructuur gevonden.

In **hoofdstuk 3** onderzoeken we grensvlak deformaties, rondom deeltjes op gekromde grensvlakken, en bestuderen we de capillaire interacties vanuit theoretisch oogpunt. Met behulp van de methode der eindige elementen hebben we de Young-Laplace vergelijking voor de vorm van het grensvlak rondom een deeltje op kunnen lossen. Daarnaast gebruikten we deze methode om de interactie potentiaal tussen deeltjes numeriek te berekenen.

De belangrijkste ontdekking die we met behulp van deze berekeningen hebben gedaan is dat, voor een anisotroop gekromd grensvlak met twee verschillende lokale hoofdkrommingen, de microdeeltjes simultaan op twee manieren het grensvlak deformeren. Er is een concave deformatie langs een hoofdrichting en een convexe – langs de andere as, een deformatie veld met quadrupolaire symmetrie is het gevolg. Twee deeltjes met zulke deformaties hebben alleen gunstige interacties als de overlappende deformaties vergelijkbaar zijn (concaaf-concaaf, convex-convex), oftewel als de deeltjes elkaar benaderen langs een van de twee hoofdrichtingen. Daarnaast is het zo dat deeltjes die interactie met elkaar hebben langs de hoofdrichtingen de neiging hebben zich te ordenen in

een vierkant patroon. Dit komt doordat twee lokale hoofdrichtingen altijd loodrecht op elkaar staan.

Ten gevolge van een quadrupolair deformatie veld, zullen twee deeltjes die elkaar naderen langs een lijn die 45 graden met de hoofdas maakt, elkaar afstoten. Dit wordt bevestigd door onze waarnemingen en is in dit geval het resultaat van deformatie oppervlakten met verschillende richting die overlappen (2 concaaf-convex paren) en excess oppervlakten die niet kleiner worden bij toenadering, maar juist toenemen. Een systeem van twee deeltjes georiënteerd onder een hoek met de hoofdas is dus onderhevig aan een krachtenkoppel, dat de as van het systeem zo roteert zodat het uitlijnt met een van de twee hoofdrichtingen. Wanneer het systeem een hoek bereikt van 45 graden met de hoofdrichting, zal het maximale koppel worden bereikt. Het koppel wordt 0 wanneer de as uitlijnt met een van de hoofdrichtingen.

De in **hoofdstuk 3** verkregen lijst van interactiepotentialen geeft ons de mogelijkheid om de z.g. minimale deviatorische kromming uit te rekenen. Deze waarden zijn nodig om capillaire interacties op gang te brengen, die sterk genoeg zijn om de thermische energie te overwinnen, hierdoor kunnen stabiele organisaties worden gerealiseerd. De berekende waarde kwam goed overeen met de deviatorische kromming uit hoofdstuk 2 waar de ordening experimenteel werd waargenomen.

In **hoofdstuk 4** bespreken we ook de mobiliteit van 3 μm polystyreen deeltjes in een monolaag van 1.5 μm kern-omhulsel microdeeltjes gepositioneerd op platte lucht-water grensvlakken; alle aanwezige deeltjes in het systeem zijn gestabiliseerd door negatieve ladingen.

In dit verkennende hoofdstuk hebben we vervolgens een poging gewaagd om de mechanische eigenschappen van dergelijke monolagen te karakteriseren door de mobiliteit van grote traceerbare deeltjes te analyseren. Met toenemende deeltjesdichtheid op de monolaag, hebben we gevonden dat de gemiddelde afstand van de traceerbare deeltjes kleiner wordt. Dit kan worden geïnterpreteerd als een toename van de viscositeit van de monolaag. Bij zeer hoge dichtheden wordt de beweging van de deeltjes subdiffusief en begrensd, wat duidt op elasticiteit van de monolaag. Ook hebben we de gecorreleerde beweging tussen aangrenzende deeltjes onderzocht in een poging om twee-punts grensvlak microrheologie toe te passen. Een vergelijking tussen de een-punt en twee-punts methode wijst duidelijk op de heterogene dynamiek van de grote traceerbare deeltjes. Ons resultaat tot nu toe vraagt om verdere ontwikkeling van de twee-punts microrheologie op grensvlakken.

In **hoofdstuk 5** zijn traceerbare deeltjes gebruikt om de eigenschappen van dunne gecrosslinkte actine netwerken gepositioneerd op het oppervlak van oliedruppels te bestuderen. Deze netwerken staan model voor de intercellulaire actine cortex. Met behulp van de algemene Stokes-Einstein vergelijking hebben we vervolgens de complexe frequentie-afhankelijke afschuifmodulus van zulke netwerken weten te bepalen. Het effect van de lengte van de actine filamenten en de cross-linker concentraties op de mechanische eigenschappen van deze lagen hebben we zodoende onderzocht.

Het voordeel van dit systeem is dat actine netwerken vrij toegankelijk zijn vanaf de water fase, en daardoor onderhevig zijn aan in-situ toevoegingen van cross-linkers, enzymen en andere interessante chemicaliën. Gebaseerd op dit gegeven, was het voor ons mogelijk, aan te tonen, dat sterke verstijving optreedt na toevoeging van myosine motor eiwitten en ATP; dit gedrag schrijven we toe aan de contractie van het actine-myosine netwerk.

Acknowledgement

At last my thesis is written. With great relief I now recollect what a huge effort it was to deliver such a small book, and it would never have come to life without the immense help and support from the people that were around during the course of my PhD.

I wish to thank all of you from my heart.

Jasper, I thank you for your kindness and patient support, with which you guided me through my research, for all the freedom that you gave me, for all your ideas and inspiring mathematical expertise. Thank you for helping me in writing the publications and this thesis, without you I would never have been able to finish them all. I wish you a happy life!

Martien, I want to thank you for your countenance, with which you supported me in the most decadent moments of my PhD; somehow you always knew when it was necessary to come up and give me a few reassuring words. Perhaps one day we will again have scientific and philosophical discussion.

Hans Lyklema, thank you for connecting eastern and western science! Whenever I talked to you, I had a feeling that I had a glimpse of a part of the incredible history of science flashing in front of my eyes, and in this flash scientists with great names, who had been almost mythical for a young researcher, become alive and real. Thanks to you I felt that we, young PhDs, are a small part of this bright history too.

Frans Leermakers, thank you for your intrinsic readiness towards scientific discussions and your inexhaustible “I have an idea!”. I remember my first day in Wageningen, which I spent in your apartment as if it was yesterday. The night of a random walk with a senior Dutch scientist in Basel is an unforgettable experience too; we need to repeat it someday. Next time we do it in Saint Petersburg in the white nights.

Josie, thank you for being always positive and for sharing your shiny smile giving a warm support to everyone. Mara, you have trained enough, it is time to go and take golden medals on next Olympic Games!

The room 0020 in PCC lab… After four years the sound of it is as good as “home”. Always with a warm, friendly and inviting atmosphere, it was often used as a meeting place, gathering many PhDs for funny and sometimes serious talks. Kathelijne, Yunus, Maria, thank you for being such great office mates! Yunus, it was great to be your neighbor at Haarweg and playing music with you. Mustafa, I remember you and wish you success! Liyakat, we spent a lot of time together in the gym and we always had interesting discussions; all the best, man! Armando, Liyakat and Yunus, thank you for the “philosophical week” that we spent in Italy. I will always remember those times with warmth in my heart and sincerely wish to repeat this experience once more. Yuan, you took something special from the lab when you left. I wish you good luck with your scientific career!

Katarzyna and Kuba, Gosia prime, Gosia double prime and Marcin, Soumi and Surrender, thank you for bringing sports, social activities and a little bit of east in my otherwise boring evenings. Thank you for all the interesting discussions and fun that we had together. Katarzyna and Gosia, you have my very special gratitude for everything!

Huanhuan, thank you for your always positive attitude, openness and willingness to help. Your questions motivated me to learn more and more about Matlab; I should thank you for this. It was a great pleasure to work with you, and I hope we can do more collaboration in future.

Huanhuan, Lennart, Christian and Frank, thank you for helping out with your cars! Lennart, your openness is something to admire in some moments, and something to run away from for the rest (by far the major fraction) of the times. I sincerely wish you all the best. Frank, you are great, thank you for giving insights into the life of a postdoc! And it was always funny to hear you ranting about your “rheologically-motivated” dislike of soups. I wish you a great scientific career! Mark and Evan, thank you for your support and sharing experiences with me.

Jacob, it was always hilarious to hear how you go Bane at random moments. Stay positive, as you always have been. Junyou, Thao, Harke, Helen, Christian, Hande, Jeroen, Sabine, Maarten, thank you for all help that you gave me and good luck with your research. Kris, it was a great pleasure to do crazy dances and play good tunes with you, success with your research too!

To my new friends at AMOLF, Sergey, Rutger, Sebastian, Fatemeh and Noreen, good luck to you guys! Katja, I think you’ll make a truly great scientist; it was inspiring to hear your questions and explanations. Arif, I thank you for your openness and I sincerely wish you all the best!

I started with the big guys and I conclude with them. Joris, I think your example is a great motivation for any student, and I’m happy that I saw at least a part of your history. During my PhD not once but many times, I recalled your “no guts, no glory”, and it always supported me. Thanks and success to you!

Хочу сказать спасибо Татьяне Максимовне Бирштейн за ее лекции и за ее совершенно неожиданную помощь, через которую я и попал в этот замечательный коллектив. Мария Иннокентьевна, Нина Анатольевна, Софья Владимировна, Ирина Михайловна, спасибо и вам, за то, что дали мне так много!

Мама и папа, спасибо вам за все, за вашу любовь. Мы тоже вас любим и заботимся о вас, очень хотим вас видеть счастливыми! Мои родные, мои любимые сестры Маша и Саша, Саня, желаю вам всяческих успехов и радостей!

Друзья мои, Андрей, Димыч, Ренат, Игорь, спасибо вам за прекрасные студенческие годы. Я надеюсь, что жизнь нас не сильно разбросает по этой маленькой планете, и мы будем видеться хотя бы раз в год, чтобы радоваться и играть на гитарах, забывая о времени, как и раньше.

Катя, мой дорогой друг, мой жизненный спутник. Я благодарю тебя за поддержку, которую ты оказывала мне в течение всех этих лет. Спасибо тебе за твое титаническое терпение и за чудо, которое произошло в середине моего обучения во многом благодаря тебе. Я желаю тебе успеха с твоим тезисом, я верю в тебя – у тебя все получится. Я мечтаю, чтобы ты была свободна и беззаботна, как ребеночек. И я очень хочу дарить тебе эту свободу, и очень прошу тебя быть моей невестой. И прошу тебя о самом главном: радуйся, Бог с тобой!

Спасибо всем. Слава Богу за всех, за все, за эту книгу.

Dmitry, Bussum, 2014.

List of publications

This thesis

- Dmitry Ershov, Joris Sprakel, Jeroen Appel, Martien A. Cohen Stuart, Jasper Van Der Gucht, "Capillarity-induced ordering of spherical colloids on an interface with anisotropic curvature", *PNAS, 2013 June*.
- Dmitry Ershov, Martien Cohen Stuart, Jasper Van Der Gucht, "Mechanical properties of reconstituted actin networks at an oil–water interface determined by microrheology", *Soft-Matter*, 2012, 8, 5896.
- Dmitry Ershov, Martien A. Cohen Stuart, Jasper Van Der Gucht, "Near-field capillary interactions between spherical particles on curved interfaces"; *to be submitted*.

Other work

- Sourav Bhattacharjee, Dmitry Ershov, Kleanthis Fytianos, Jasper van der Gucht, Gerrit M Alink, Ivonne M C M Rietjens, Antonius T M Marcelis and Han Zuilhof**,** "Cytotoxicity and cellular uptake of tri-block copolymer nanoparticles with different size and surface characteristics", *Particle and Fibre Toxicology*, 2012.
- T. Krebs, D. Ershov, C.G.P.H. Schroen and R.M. Boom, "Coalescence and Compression in Centrifuged Emulsions Studied With In-Situ Optical Microscopy", *Soft Matter 9, 2013*.
- Huanhuan Feng, Joris Sprakel, Dmitry Ershov, Thomas Krebs, Martien A. Cohen Stuart, Jasper van der Gucht, "Two modes of phase inversion in a drying emulsion", *SoftMatter 9, 2013*.
- Merel JC van der Ploeg, Johnnes HJ van den Berg, S. Bhattacharjee, Laura HJ de Haan, Dmitry Ershov, "In vitro nanoparticle toxicity to rat alveolar cells and coelomocytes from the earthworm Lumbricus rubellus", *Nanotoxicology*, 2012.
- Sourav Bhattacharjee, Dmitry Ershov, Mohammed A. Islam, Angela M. Kampfer, Katarzyna A. Maslowska, Jasper van der Gucht, Gerrit M. Alink, Antonius T. M. Marcelis, Han Zuilhof, Ivonne M. C. M. Rietjens "Role of membrane disturbance and oxidative stress in the mode of action underlying the toxicity of differently charged polystyrene nanoparticles", *RSC Advances*, 2014.

- Huanhuan Feng, Dmitry Ershov, Thomas Krebs, Karin Schroen, Martien A. Cohen Stuart, Jasper van der Gucht, Joris Sprakel, “Switching between two modes of coalescence in dense thermoresponsive emulsions”, *Langmuir, submitted 2013.*

Publications 2005-2008:

- L. A. Kartsova, N. A. Kasyanenko, A. V. Alekseeva, O. V. Ganzha, S. V. Paston, D. S. Ershov, “Electrophoretic determination of catechins and examination of their complexing with organic and inorganic compounds”, *Russian Journal of Applied Chemistry*, October 2008, Volume 81, Issue 10, pp 1758-1763.
- D.S. Ershov, S.V. Paston, I.M. Ziryanova, N.A. Kasyanenko. Study of the radioprotective behaviour of catechin in DNA solutions exposed to γ- and UV radiation, *Vestnik SPbGU*. Ser. 4, vol.2. St.-Petersburg, 2007. pp. 3-9.

Overview of completed training activities

1. Discipline specific activities (courses, workshops, symposia, summer schools etc.)

Trainings

- Han-Sur-Lesse Winterschool ’10 (Han-Sur-Lesse, Belgium; organized by Combined Physical Chemistry groups NL)
- European School on Rheology ’09 (KU Leuven, Belgium; organized by BGR/SoftComp)

International conferences

- European Polymer Congress ’11 (Granada, Spain; organized by EPF/GEP; 1 poster)
- FOM Physics ‘11&’13 (Veldhoven, the Netherlands; organized by FOM; 1 oral in ’13)

Local conferences

- Colloid Physics meeting between FYSKO@WUR and PCC@Utrecht ’13 (Wageningen, the Netherlands; organized by WU/UU; 1 oral)
- Dutch Polymer Days ’09-’13 (the Netherlands; organized by NOW/PTN/KNCV)
- Dutch Soft Matter Days ’10-’13 (the Netherlands)

2. General courses (e.g. PhD week, language courses, presentation courses, statistics, etc.)

- Techniques for Writing and Presenting a Scientific Paper ’11 (Wageningen the Netherlands; organized by WUR/VLAG)
- VLAG PhD week ’09 (the Netherlands; organized by VLAG)
- Electron Microscopy Workshop ’12 (Wageningen, the Netherlands; organized by WEMC/Cat-AgroFood)
- Presenting Research to a Broad Audience ’13 (Wageningen, the Netherlands; organized by FYSKO@WUR/deperskamer.eu)
- Emulsions & Foams ’10 (the Netherlands, organized by Wilten Instrumenten)
- “An introduction to statistical Thermodynamics with a focus on Molecular modelling” ’12 (Wageningen, the Netherlands; organized by FYSKO@WUR)

3. Optionals (participation in discussion groups, PhD excursions, MSc courses, etc.)

- PhD excursion Swiss & France ’09 (organized by FYSKO@WUR/VLAG)
- PhD excursion South East Asia ’11 (organized by FYSKO@WUR/VLAG; 1 oral)
- Weekly group meetings ’09-’13 (FYSKO@WUR)
- Colloquia ’09-’13 (FYSKO@WUR)
- “Advanced Soft Matter” ‘09 (FYSKO@WUR)

Cover: design and art by the author.

Printing: Wohrmann Print Service, Zutphen, the Netherlands.

This research was financially supported by VLAG